CORE
Metadata, citation and similar papers at core.ac.uk
Provided by University of Salford Institutional Repository

A novel technique for measuring and sensing rain

Arun KUNDGOL

School of Computing, Science and Engineering
University of Salford, Salford, UK

Submitted in Partial Fulfilment of the Requirements of the Degree of Doctor of Philosophy,

2015

Contents

List of figures

List of tables

List of symbols

F_d	Drag force
We	Weber number
F_g	Force on the drop due to gravity
η_a	Viscosity of air
d	Diameter of a spherical drop
u	Fluid velocity
g	Acceleration due to gravity
C_d	Drag coefficient
ρ_a	Density of air
σ	Surface tension
r	Radius of a cylindrical drop
ρ_w	Density of water
Vt	Terminal velocity of a drop
m	Mass of a rain drop
F	Force of a drop
v	Velocity of drop at time of contact
v_0	Velocity of drop at point of contact
r	Radius of spherical and cylindrical drop
h	Height of lower cylinder of a cylindrical drop
y	Changing in height of lower cylinder of a cylindrical drop
T_R	Drop intensity
$n(d)$	Number of drops as a function of the size of droplets of diameter d
R	Rain rate
N	Tot al number of drops detected
$x(t)$	Input to a time invariant system in time domain
$y(t)$	Output a time invariant system in time domain
$h(t)$	Frequency response function for a time invariant system in time domain
$X(\omega)$	Input to a time invariant system in frequency domain
$Y(\omega)$	Output a time invariant system in frequency domain

$H(\omega)$	Frequency response function for a time invariant system in frequency domain
$[M]$	Modal mass matrix
$[C]$	Damping matrix
$[K]$	Stiffness matrix
$\{q\}$	Acceleration vector
$[\phi]$	Eigenvectors matrix
C	Capacitance
ε_0 ε_r	Absolute and relative permittivity
d_p	Distance between plates
D	Charge density
Q	Charge developed
A	Conductive electrode area
d_{3n}	Appropriate piezoelectric coefficient for the axis of applied stress or strain where n is the axis of applied stress or strain
X_n	Stress applied in relevant direction
V_0	Output voltage of the sensor
g_{3n}	Appropriate piezoelectric coefficient for the axis of applied stress or strain where n is the axis of applied stress or strain
th	Film thickness

Acknowledgements

There are a number of people to whom I owe a debt of gratitude for their help and support without which this work could not have been completed. Firstly for their guidance with the overall scope and focus as well as detailed advice in all aspects of the work completed I would like to extend my sincere thanks to my supervisors, Prof. Nigel Mellors and Prof. Andy Moorhouse of the School of Computing, Science and Engineering at the University of Salford.

I am very grateful to Jon Crossley from Dyer Environmental Controls Ltd for providing me the opportunity and funding my research. Special thanks are due to Andy Elliott of Acoustics department at the University of Salford, I owe him a few beers for the help he has provided me.

Finally I would like to thank my family and all my friends for their encouragement and support throughout the project throughout the process of my PhD, for always being prepared to take my side and sticking through with me until the end.

Abstract

Rainfall passing over a given area is a highly dynamic process; it changes constantly in form and intensity. It varies constantly on short spatial and temporal scales that makes real time measurements of the amount of rainfall challenging. Measuring and sensing rain is important to be able to understand and control our urban environment. Traditionally, rainfall analysis for hydrologic modelling use spatial measurements collected at various sparsely spread observation points using rain gauges working on various principles such as weighing type, tipping bucket, capacitive type etc. An accurate representation of spatial model of rainfall is essential for hydrological operational purposes such as forecasting of river flow, flood irrigation planning and modelling of catchment areas. Measurement of drop size distribution are also exploited to investigate microphysics of precipitation and to improve rainfall remote sensing estimation techniques. However, the high initial costs of convectional rain gauges prevent collection of data with high spatial resolution. The research looks at investigating the sensor stack to be a part of an integrated sensor approach to develop a device architecture for the development of low cost integrated rain sensing and measuring the rain.

The device architecture consists of three main stacks – energy generation layer, sensing layer, processing layer. The raindrop on impact causes vibration on the device surface. This force exerted by the raindrop causes a deflection and is measured indirectly by the use of a thin film piezo sensor. As part of the work, we find there is a good correlation between the vibrations caused and the size or volume of the raindrop by indirectly measuring the impact force of the raindrop. The working range of the device is between $100hz$ and $2000hz$, which includes the first modal peak of the impact that acts as an amplification to the drop's impact. Using this information, the device is able to calculate the raindrop size distribution and the rain intensity. Calibration of the device is key as we are measuring the impact force of the rain drops and correlating it to the size of the drop. Primary, not all rain drops will fall on the device at terminal velocity (the main assumption for calibration of the device), as the fall velocity of the droplet may also be affected by the wind. Secondly, the spatial variation of the frequency response function in $Volts/Newton$ in decreasing order from the centre of the plate. This research is funded by Dyer Environmental Controls Ltd.

1 Introduction

1.1 Overview

Rainfall passing over a given area is a dynamic process; it changes in form and intensity. As water is a vital resource, numerous research studies have been conducted to understand rain. The sensing and measuring of the type and amount of rain helps us develop a physical and dynamic description of rain and thereby helps us gain a better understanding of our environment and prepare for possible environmental disasters such as drought or flooding. However, the localized nature and variability of precipitation makes it difficult to understand and model its physical parameters and behaviour. The parameters that describe the type of rainfall include total amount of rain, rainfall rate, drop size distribution, and rain reflectivity. These measurements have a broad range of application in meteorology and hydrology, (Tokay, Kruger, & Krajewski, 2001; Van Dijk, Bruijnzeel, & Rosewell, 2002). The study of these parameters help obtain a physical and dynamic description of rain, and provide a better understanding of its impact, intensity, and energy (Fernandez-Raga et al., 2011).

Since the 17th century, measurement of rainfall in a scientific sense has been conducted. The methods of measurement has changed with innovative thinking over the different centuries from manual gauges to drop counting techniques to satellite based data. Some examples of measurement techniques include mechanical recording gauges (float- operated recorders, weight- operated recorders), electrical rain gauges (tipping bucket, capacitance gauges), and drop- counting gauges (vibration based disdrometers, optical based disdrometers) (Strangeways, 2010). Modern day measurement techniques include the use of weather radars supplemented by ground based measurements that can be used from a single location to produce a real time detailed precipitation information for large areas. However, irrespective of the method used, radar based rainfall measurements are quantitatively less accurate than rain gauge measurements, also the weather radars are required to be carefully calibrated. The error in measurements by weather radars are typically a factor of two or more out. The sources of these errors in measurement may include radar reflectivity factor, evaporation and advection of precipitation, variability of raindrop size distribution and vertical air motions. The agreement between radar and surface rain gauges decreases with increase in radar ranges. For high accuracy rainfall measurement where the average error is less than 10- 20%, there is no real advantage in the use of a radar as the number of rain gauges required to provide the desired accuracy is sufficient to provide the accuracy (Wilson & Brandes, 1979).

The rapid development of wireless sensing technologies over recent times, makes it possible to build inexpensive sensor networks enabling the science of big data with improvements in monitoring for applications such as buildings, transport systems, and many others. These interconnected devices are constantly collecting/ processing data, and bringing about an improved accuracy and an increase in the density of measurements being made. This large density of data helps provide a better understanding of our physical world by analysing different events/ occurrences (Barnaghi, Wang, Henson, & Taylor, 2012). The chosen method for computing the drop size distribution and rain intensity is to measure the vibrations caused on a clamped plate using a thin film piezo film, details of which will be discussed as part of this research.

1.2 Product gap

As mentioned earlier, ground based measurements of rainfall are fundamental to developing an accurate representation of its spatial model. A high spatial density of accurate measurements has advantages for hydrological operational purposes such as forecasting of river flow, flood, irrigation planning, erosivity of rainfall, and modelling of catchment areas. And data regarding drop size distribution is also largely exploited to investigate microphysics of precipitation and to improve rainfall remote-sensing estimation techniques. It is for this purpose larger numbers of devices are required. However, due to the high cost of maintaining gauges; there has been a decrease in ground based measurements of these parameters (Amos, 2014). What is required is a cheap, convenient, low maintenance method to conduct similar measurements of drop size distribution and rain intensity.

The aim of the research is to investigate the sensor stack to be a part of an integrated sensor approach to develop a device architecture for the development of low cost integrated rain sensing and measuring device which can then be deployed in large numbers for the aforementioned applications or alongside home automation devices such as solar integrated window control devices (Crossley, Kundgol, Mellors, & Waterworth, 2011). The integrated rain measuring device's architecture consists of three main stacks – energy generation layer, sensing layer, processing layer as shown in Figure 1.

The device's chosen working principle is based on an acoustic disdrometer. An acoustic disdrometer is a device wherein the vibration caused by a rain drop falling on the device is

converted to an electric pulse that is then correlated to the size of the droplet. These individual drops are counted and the data is used to develop the drop size distribution which is then used to calculate the rain rate.

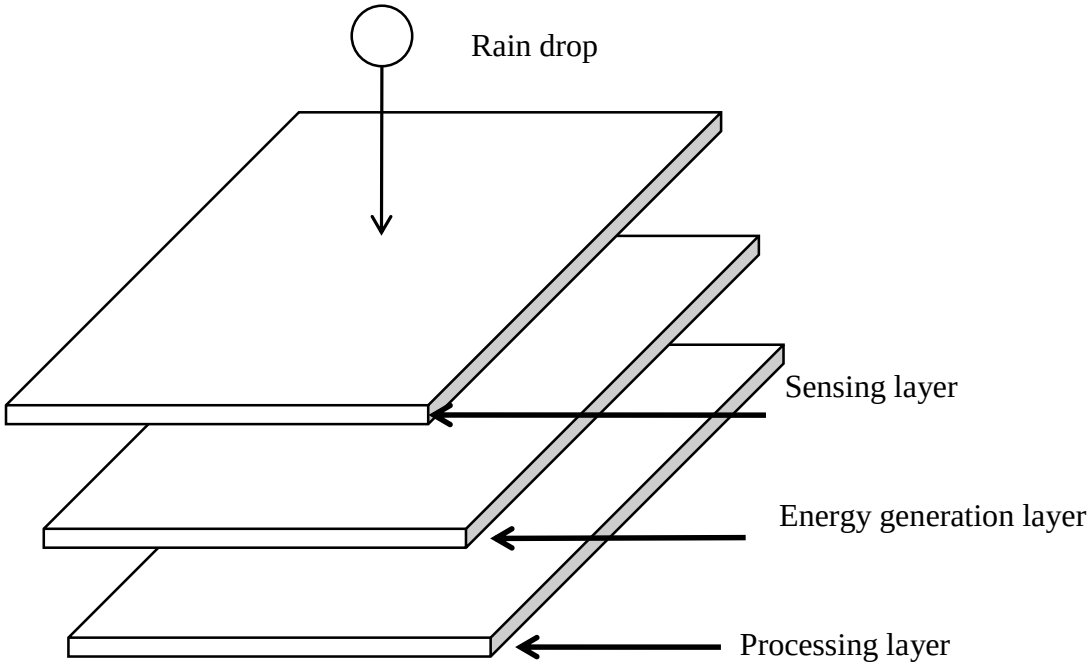

Figure 1: Proposed design architecture of the device for sensing and measuring rain

The drop size distribution (DSD) is defined as the probability distribution of the number of drops per unit size (can be expressed in diameter/ volume of the drop) and per unit volume of space as measured on the surface of earth providing a complete description of rain (Campos, 1999). The drop size distribution can be used to calculate the rainfall rate from existing parametric fits of distribution parameters (Jameson & Kostinski, 2001). One such example of an acoustic disdrometer is the Joss- Waldvogel disdrometer (JWD) was invented in 1967 manufactured by Distromet of Basel, Switzerland (Sheppard & Joe, 1994). Other types of disdrometers available in the market are optical based. However, both these types of devices are very expensive to dispatch in large number in a particular area.

1.3 Thesis objectives

This research is fully funded by Dyer Environmental Controls Ltd. The aim of this research is to investigate the sensor stack to be a part of an integrated sensor approach to develop a device architecture for the development of low cost integrated rain sensing and measuring device. The

device architecture consists of three main stacks – energy generation layer, sensing layer, processing layer. The objectives of this work can broadly be summarised into the following:

- Identification the technique for quantifying the amount of rain using an embedded sensor approach.
- Design, and implementation of experiments and analysis of results.
- Design and test of prototype device

1.4 Thesis structure

This thesis discusses the work carried out during the study. It provides a review of the literature in the subject area, design of various experiments, discusses its results and provide an outline to the design parameters of the device.

Chapter 2 is a critical review of the relevant literature. It looks into understand the process of rain formation and how that affects the characteristics of rain – amount of rain, rain intensity, and rain drop size distribution and how these affect the physics of rain – force of a drop, terminal velocity, maximum size and volume. It will also look into the different techniques for measuring rain and provide a background for choice for selecting the architecture of the device.

Chapter 3 discusses the first of experiments conducted to characterize the responses of different plates of different thickness and size to find the optimal dimensions for the sensing area of the suggested device. **Chapter 4 and Chapter 5** discusses the design and development of the rain generator and the experiments created for characterisation of different sizes of droplets of water, and ratification of the drop force model.

Chapter 6 looks to measure the device plate to different levels of noise, to verify the impact of noise on its sensitivity. **Chapter 7,** draws conclusion from the work carried out in the previous chapters for the simulation of the proposed device. It also includes methods to calibrate the device, and to calculate the drop size distribution, rain intensity. **Chapter 8** is the concluding chapter and also suggest areas of further work.

2 Literature & theory

2.1 Introduction

The chapter is divided into three main sections. In section 2.2, we will look to understand what is rain - the process of rain formation is, provide an understanding of existing techniques used for measuring various rain parameters (amount of rain, rain intensity, drop size distribution, and relationship between these parameters) and finally understand the dynamics of rain – maximum size and volume, velocity of a raindrop, force of a raindrop. Section 2.3 will look to provide basics for vibration measurements and analysis in machines and how key concepts (modal model and frequency model) can be used for identification of forces for this particular application. Finally, section 2.4 will look to provide a background on designing sensors and what type of sensors can potentially be used.

2.2 Background to Rain

2.2.1 Introduction

In this section, we look to understand the techniques used to measure various parameters of rain – rain intensity, drop size distribution and the parameters used to define the dynamics of a rain drop. Rain is a naturally occurring phenomenon and is a highly dynamic process. Over a particular area it is constantly changing in both form and intensity. According to the Met Office (U. K. national weather station), rain is defined as the liquid water in the form of droplets that have condensed from atmospheric water vapour and then precipitated. Rain is an important source of fresh water and is a major component of the water cycle, not only providing water for the sustenance of different ecosystems but also water necessary for different human activities (drinking water, crop irrigation, etc.).

Rain is typically described by the use of parameters such as rain rate and raindrop size distribution where rain rate is defined as the measure of the intensity of rainfall and is expressed in millimetres per hour (in units of speed rather than volume) and it is the most commonly used parameter. It is given by the product of the raindrop concentration and volume and terminal speed of the drop (Kostinski & Shaw, 2009). Drop size distribution is defined as the probability distribution of the number of drops per unit size (expressed either in diameter or volume of the drop) per unit volume of space as measured on the surface of the earth. The drop size distribution helps provide a complete description of rain and is typically used to investigate the microphysics of precipitation and improve remote sensing of rain (Campos, 1999).

2.2.2 Rain formation

Before exploring the descriptors for rain, it is instructive to understand the formation process of rain. There are different methods describing the formation of rain, these include convectional rain, frontal rain, and relief rain. Convectional rain is formed as a result of rise in temperature of ground and the air above it due to hot weather conditions. The warm air has an increased capacity to absorb and hold more water. As the warm air above the ground rises, there is a reduction in temperature by 1℃ for every $100m$ rise in altitude. Eventually, leading to forced condensation of water vapour to rain drops. The frontal rain process, is a result of the collision of the less dense warm air with cooler air leading to cooling of the warm air. As the air cools, this leads to the formation of clouds and precipitation of water vapour. And finally, the relief rain process is a result of a physical obstruction (mountains, hills, cliffs) forcing warm moist air to rise and cool over the obstruction, leading to the formation of rain clouds or fog depending on how large the droplets grow.

The growth process for the droplets is the same for all these different types of rain. Mason (1978) describes the growth of a single raindrop using first mechanics (the branch of science wherein physical bodies are either at rest or in motion). He suggests that not all cloud droplets have the same diameter and only one in a thousandth cloud droplet grows on a large hygroscopic nucleus by condensation to two or three times its average size. This grows further by capturing other small droplets around it. Sea based salt particles typically form the largest hygroscopic nuclei. These hygroscopic nuclei are formed by the evaporation of large drops formed due to the bursting of air bubbles (found in the foam of breaking waves) and consequent rushing of water into thus formed craters.

On the course of the fall of the raindrop through a cloud, it could overtake, collide, and coalesce with smaller droplet. The course of these actions is dependent upon the size of the droplet. This interaction of the raindrops is important to the structure of the rainfall providing an inherent limitation to the size and velocity of the rain drops. This understanding helps with developing a relation between the drop size and drop velocity.

2.2.3 Techniques for measuring rain

In the previous sub section we looked into understanding the formation of rain and how this affects the values of the descriptors for rain. In this sub-section, we will look into the various techniques for measuring rain. There are primarily two main parameters that is measured by meteorologist for a particular rain even, these include rain gauging, and drop size distribution.

2.2.3.1 Rain gauging

Here we look at the different methods for rain gauging and its evolution during time. Hanna (1995) quotes Savage and McGee's explanation of rainfall measurements as "The principle is that a gauge intercepts precipitation over a known, clearly defined area bounded by the rain-gauge rim, to measure the amount of water so collected, which is expressed in depth units. It is then assumed that the depth of water intercepted is the same as the depth of rain which fell on a large area surrounding the gauge."

Rain gauge measurements represent one in a billion of a small $15km^2$ catchment area, making simple modern gauges an epitome of much painstaking research; Strangeways (2010) provides an insight into the history of rain gauges. Currently, there are three main types of rain gauges available in the market.

Manual gauges: There are over fifty different types of manual gauges in use worldwide. They are all a variation of the same construction. One such example of a manual gauge is the UK Met office Mark 2 rain gauge example in Figure 2. This is a five- inch gauge, it stores an equivalent of 75 millimetres of rain water in a bottle below ground and is read daily using a graduated measuring cylinder. A larger base allows for weekly or monthly amounts of rain to be stored.

Mechanical recording gauges: Two main types of mechanical recording gauges are present – the float- operated recorders and the weight- operated recorders. A typical chart-recording rain gauge is the tilting siphon designed by Dines in 1920 example in Figure 3. The principle of operation is rain fed into a cylinder with a float that rises as water enters thus moving a pen up a paper chart. As the float approaches to the top it starts a siphon process by causing the cylinder to tip over and when it is nearly empty the cylinder tips back to its vertical. Some other examples are the Negretti and Zambra gauge and the Hellmann siphon gauge.

Figure 2: Five-inch standard UK MET Office gauge, with graduated measuring cylinder image taken from (Strangeways, 2010)

The weight-operated recorder works by recording the weight of precipitation as it accumulates in a container suspended on a spring or the arm of a balance. The movement of which is magnified by levers moving a pen. The first example of a weight- operated recorder was designed by Osler in 1937. These types of devices must be emptied regularly; this is done either by hand, or siphoning of the water, or the tipping of the container (Strangeways, 2010).

Figure 3: Dines tilting siphon gauge: (a) complete; (b) open to show mechanism image taken from (Strangeways, 2010)

Electrical rain gauges: There are four different categories of electrical rain gauges. The most common type is the tipping bucket gauge. It works on the principle of tipping of the bucket which moves a magnet past a reed switch giving a contact- closure which is recorded by a data logger. The buckets are designed to tip at 0.1, 0.2, 0.25, 0.5 and $1mm$ of water. Another type

is the electronic weighing rain gauge which works on the principle of logging the accumulated rainfall in a water container on a load cell. This method requires some means of emptying the container. In the case of unattended operations, this is achieved by siphoning of the water. The capacitance type rain gauge, wherein the water collected is measured by storing it in a cylinder containing electrodes that act as the plates of a capacitor with the water behaving as the dielectric (the dielectric constant of water is around 80 and of air is 1). Finally, the drop-counting gauge which works on the principle of counting the drops produced by the collected water; this provides a good measuring of the rainfall-rate. However, due to drop size variations as a result of changing surface tension, the accuracy is limited (Strangeways, 2010).

There are many sources of possible errors. All of the above mentioned methods require some form of human intervention for either making measurements, or maintenance of the equipment. The tipping bucket as an example, is a simple device whose work principle is based on alternately fill and dump of two buckets. Any asymmetry in the fill-dump cycle of the two buckets (especially during high rainfall rates) can lead to errors in the measurements. Maintenance is another issue associated with this type of measurement- if these instruments are left unattended for long periods of time, it can lead to the clogging and jamming of the mechanical action by insects, or dead leaf. Another issue with most systems is the drift in clock time, most data loggers have a typical drift of the order of one minute per month and would require to be synchronized.

2.2.3.2 *Drop size distribution*

An early method of measurement of drop size distribution was originally presented by Bentley (1904) and then modified by Laws and Parsons (1943) was conducted through a straightforward laborious process of allowing raindrops to fall into a layer $(2-3cm)$ deep of fine and smooth flour in a container of $10cm$ in diameter. This box is exposed to the rain for a few seconds. The raindrops remain in the box until the dough- pellet is dried; these dried pellets are separated, measured and counted. Today this method is modified to use plaster (Ries, Seeger, Iserloh, Wistorf, & Fister, 2009). Later, Jones (1959) developed a method using two cameras placed close together that are synchronised to take two photos simultaneously of the raindrop from two perpendicular angles (east-west or north- south); making it possible to take a three-dimension al image of the shape of raindrops and from there calculate the drop size (Fernandez-Raga et al., 2011).

Until recently, a more widely used instrument is the disdrometer based on micro phonic measurement developed by Joss and Waldvogel in 1967 manufactured by Disdromet of Basel, Switzerland. Here the sensor head contains a thin aluminium surface covering a Styrofoam body. The surface is $50cm^2$ shallow cone that converts the vertical impact of the raindrop into electrical impulses. This voltage in the sensory coil is amplified and applied to the secondary coil producing an electromagnetic force that restores the body to its rest position (Sheppard & Joe, 1994). The instrument detects raindrops with diameters of between 0.3 and 5mm up to 5% accuracy and can record a maximum of 190 impacts per second in the sampling area. A schematic representation of the working of Joss- Waldvogel disdrometer is shown in Figure 4.

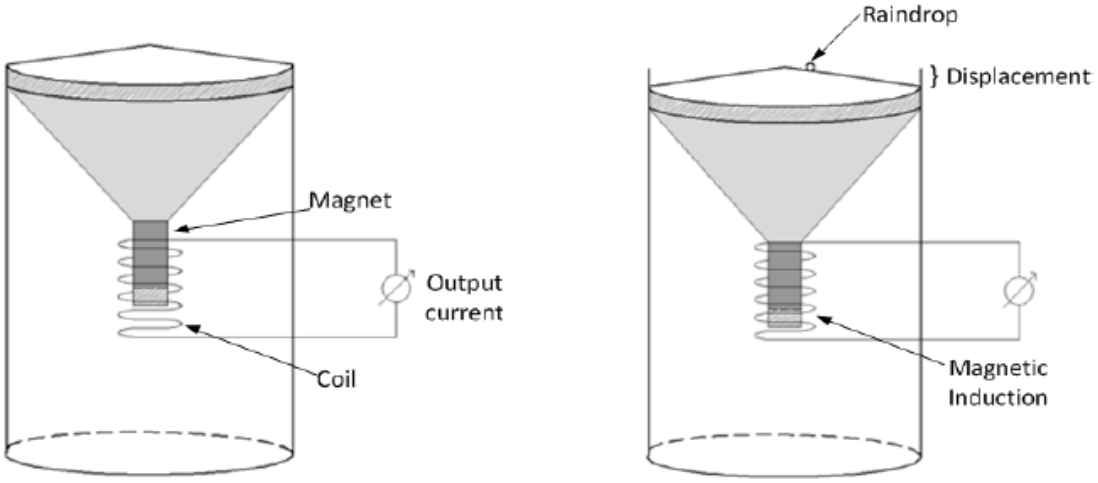

(a) Normal Condition (b) When drop impinges on the surface

Figure 4: Schematic representation of working of the Joss- Waldvogel disdrometer image taken from Bagree (2012)

The first non-electromagnetic type systems also known as optical devices were developed in the 1970, one such example is the Particle Measuring System (PMS) spectrometer is a shadowing probe manufactured by Particle Measuring Systems (PMS) Inc. of Boulder, Colorado. The instrument measures the size of particles passing through a laser beam (optically shaped into an elliptical cross section by cylindrical lenses) by the shadow created on a linear array of 64 photodiodes introduced the possibility of measuring precipitation particles far from the ground (by installing the PMS on an aircraft). Optical disdrometers are much improved since the 1980s and the 1990s, they have gotten better at distinguishing between different raindrop sizes by becoming more sensitive and precise. Other examples of optical devices such as Optical Spectro-Pluviometer (OSP) can simultaneously measure the diameter and the fall

velocity of the drops. The principle of operation for an optical based disdrometer is measurements are taken as raindrops fall through a parallel beam of ultraviolet light. These types of instruments were used to measure the individual drop size and then the drop size distribution. The Vaisala RAINCAP sensor developed by (Salmi, Ikonen, & Oyj, 2005) converted the impacts from the drops to its proportional volume to calculate the accumulated precipitation.

2.2.4 Dynamics of raindrops

In the previous sub section we looked at existing methods used to measure rain (rain gauging techniques, and drop size distribution). As this research looks to sense and measure rain by analysing the vibrations caused, an understanding of the dynamics of raindrops is important. This section looks to describe the parameters used for understanding the physics of a rain drop.

2.2.4.1 Raindrop mass and size

Firstly, let's look at the relation between the mass and the size of the raindrop. As mentioned earlier, raindrops fall from the clouds, the characteristics (size and shape) of the raindrop is affected by its interactions (coalescence by collision with other droplets, turbulence in air, deformation of drop shapes and disintegration). The size of the droplet is limited by its flow in air that can potentially overwhelm the cohesive forces of surface tension of the drop, this competition between surface tension. As a result the maximum possible size for a stable water droplet at terminal velocity in stagnant air is 6 mm diameter. However, it must be noted larger drops of size up to 10 mm in diameter have been observed in Brazil and Hawaii and this is attributed to the surfactants produced by forest fires detected in the raindrop. (Kostinski & Shaw, 2009; Villermaux & Bossa, 2009).

2.2.4.2 Velocity of a raindrop

Now, we will look at the relation between the size of the raindrop and its velocity. A raindrop falling in still or stagnant air reaches its terminal velocity when the drag force (F_d) is balanced by the weight of the drop (F_g) as shown in Figure 5. Assuming a spherical rain drop of diameter size d and density ρ_w.

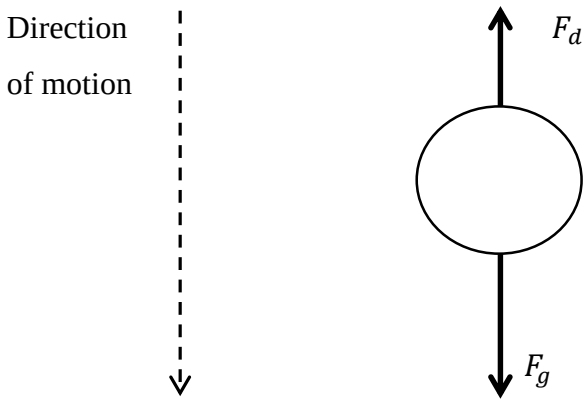

Figure 5: Assessment of the forces acting on a drop during its fall adapted from (Guigon, Chaillout, Jager, & Despesse, 2008b) where F_d is the drag force and F_g is the force due to the weight of the drop.

By equating the drag force and the force due to the weight of the drop, we can derive the formula for terminal velocity as follows,

$$F_d = F_g, \qquad 2.1$$

$$\tfrac{1}{4}\pi\, d^2 \times \tfrac{1}{2} C_D\, \rho_a\, \mathrm{V}_t^2 = \tfrac{1}{6}\pi\, d^3 \rho_w\, g,$$

$$V_t = (\tfrac{4}{3}\rho_w\, g\, d / \rho_a\, C_D)^{1/2} \qquad 2.2$$

where C_D, is the drag coefficient which is the function of the Reynolds number Re and $Re = {V_t\, d\rho_a}/{\eta_a\, \eta_a}$, is the viscosity of air. The Reynolds number is used in fluid mechanics to predict flow patterns in different fluid flow situation, it is a dimensionless quantity.

For non-spherical drops the diameter of an equal volume is normally used and C_D is adjusted accordingly. The drag force is due to the viscous stresses and internal forces set up in the fluid by the motion of the drop through it and may be calculated by numerical solution of governing Navier – Stokes equation provided the air flow around the drop remains steady. It must be noted that the speed of raindrops in windy condition tends to be more than its terminal velocity.

Now, the terminal velocity of water droplets has been extensively researched and many have experimentally developed a model as a function of the drop diameter (d in mm). Some examples of the models include ones by (Best, 1950) $V_t = 10.30 - 9.65\exp(0.6d)$ which is a good fit for diameters larger than $0.4\ mm$ but then predicts a negative terminal velocity for very small drops. Gossard, Strauch, Welsh, and Matrosov (1992) changed this to $V_t =$

$9.65(1.0 - \exp(-0.53d)$; although it doesn't provide a negative value it is less accurate as shown Figure 6. Uplinger (1981) proposed $V_t = 4.85\ d\ \exp(-0.195\ d)$ which over estimates the fall velocity for drop diameters exceeding 5 mm (Van Boxel, 1998). The equation provided by Valette et al. (2012) provided by $V_t = \exp(2.397 - 1.006/d)$ is a close fit to the measurements done by Gunn and Kinzer (1949) showing the terminal velocity of raindrops can be predicted. Gunn and Kinzer (1949) measured the terminal velocity of where more than 1500 droplets of mass ranging from 0.2 to 100,000 micrograms in stagnant air.

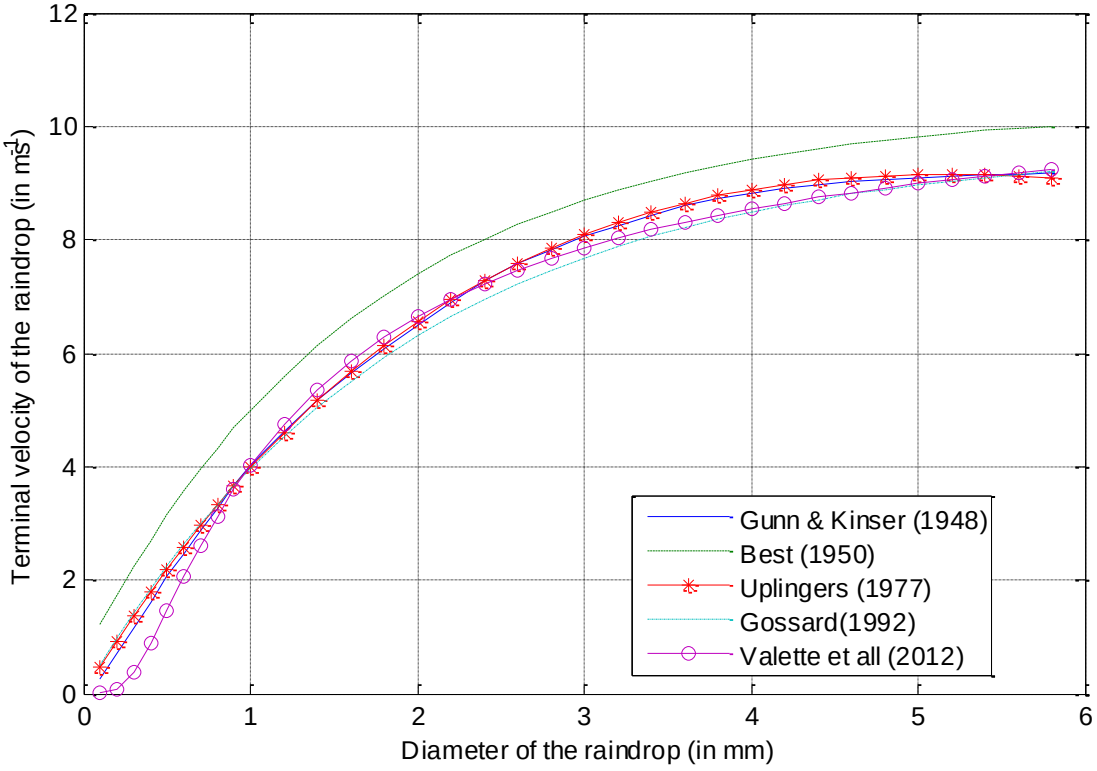

Figure 6: Comparison of the different models for terminal velocity of a raindrop vs equivalent diameter adapted from Valette et al. (2012)

2.2.4.3 Force of a raindrop

In this sub section we look to describe a function to simulate the force of a single rain drop, and the how this can be implemented for a multiple drop scenario. Petersson (1995) describes a model for the force of a single liquid drop impact. According Newton's second law, the force of a drop impacting a rigid surface can be provided by,

$$F = \frac{d}{dt}(mv) \qquad 2.3$$

where m, is the mass of the unperturbed drop and v, is the velocity at the time of impact.

This impact force of the drop can be split into two components related to - the changing mass (the breaking of surface tension and subsequent jetting of drop) and changing velocity of the drop (retardation of the drop due to impact), as shown in the following equation. Here, jetting is the process of spurting water droplets.

$$F = m\dot{v} + \dot{m}v \qquad 2.4$$

Assuming the drop has a velocity v_0 at the time of the initial contact, the velocity to be used in the flow part of the equation is provided by

$$v_0 - \Delta v$$

where $\Delta v = \int_0^{t_1} a\, dt$ and a is acceleration of the drop

However, over the complete time duration of the liquid- solid impact T, the time taken to dissipate for the drop t_1 is of minor importance as the force pulse is found governed by a peak value plus the flow part and with Δv negligible, the equation of force results as,

$$F = m_0 a + \dot{m}v_0 \qquad 2.5$$

Drop shapes are not always spherical, depending on the raindrop axis the shape distortion is observed to be a transition between spherical shape and a combination of two oblate spheroids with a decreased curvature at the lower hemisphere of the drop (Beard, Bringi, & Thurai, 2010). During the first phase of impact between the drop and the solid surface, the distortion in the shape means an extended length of time t_1(as it is dependent on the geometry of the drop). The distortion in the shape of the drop leads to a circular cylinder followed by hemisphere as shown in Figure 7.

The volume of the initial sphere of radius r (assuming that the drop volume remains constant throughout the fall), the height of the lower cylinder may be set to $h = \frac{2r}{3}$. Using the cylindrical hemispherical model as shown in the geometry in Figure 7a, the mass-time function is simply found to be

$$m(t) = \rho\pi r^2 \begin{cases} \left[\frac{2r}{3} + (h - y(t))\right], & y(t) \le h \\ \left[\frac{2r}{3} + \frac{(y-h)^3}{3r^2} - (y - h)\right], & h \le y(t) \le h + R \end{cases} \qquad 2.6$$

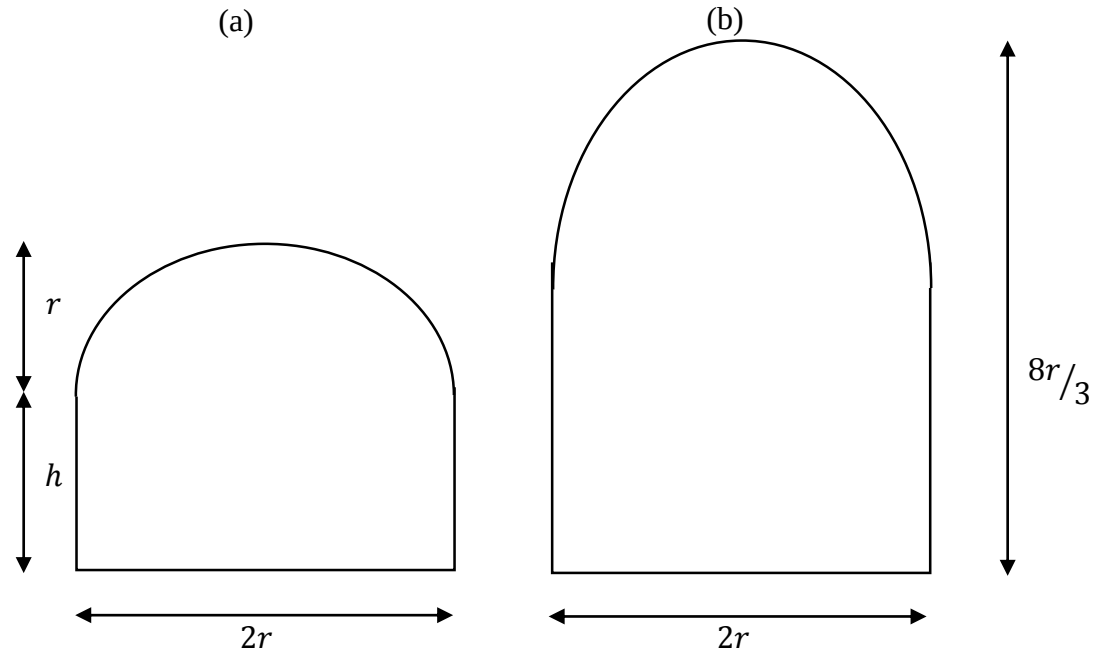

Figure 7: Simplified drop shapes (a) cylindrical- hemispherical and (b) paraboloidal adapted from (Petersson, 1995)

And the force exerted on the receiving system is obtained as

$$F(t) = -\rho\pi r^2 \begin{cases} -v_0^2, \ t \leq \frac{2r}{3v_0} \\ v_0^2 \left[\frac{5}{9} + \frac{4v_0 t}{3r} - \frac{v_0^2 t^2}{r^2}\right], \ \frac{2r}{3v_0} \leq t \leq \frac{5r}{3v_0} \end{cases} \quad 2.7$$

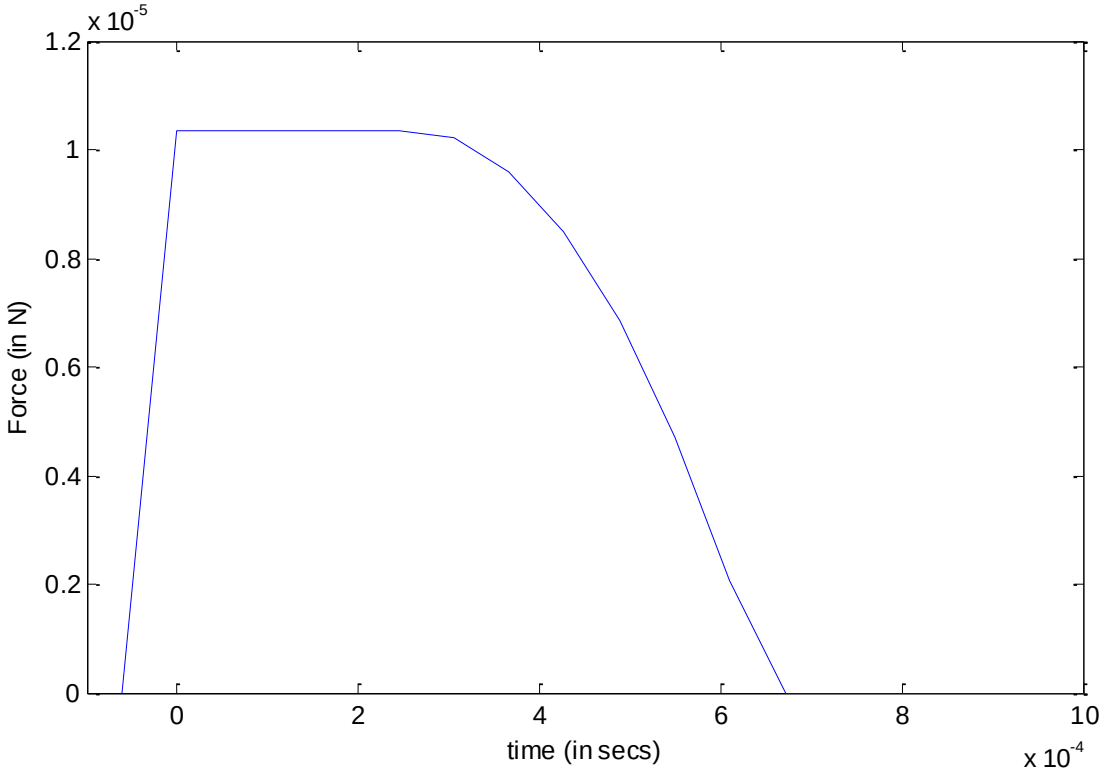

Figure 8: the simulated force of a raindrop in time domain of equivalent diameter $0.2998mm$ *and its terminal velocity of* $0.3834m/s$ *using Petersson (1995) equation*

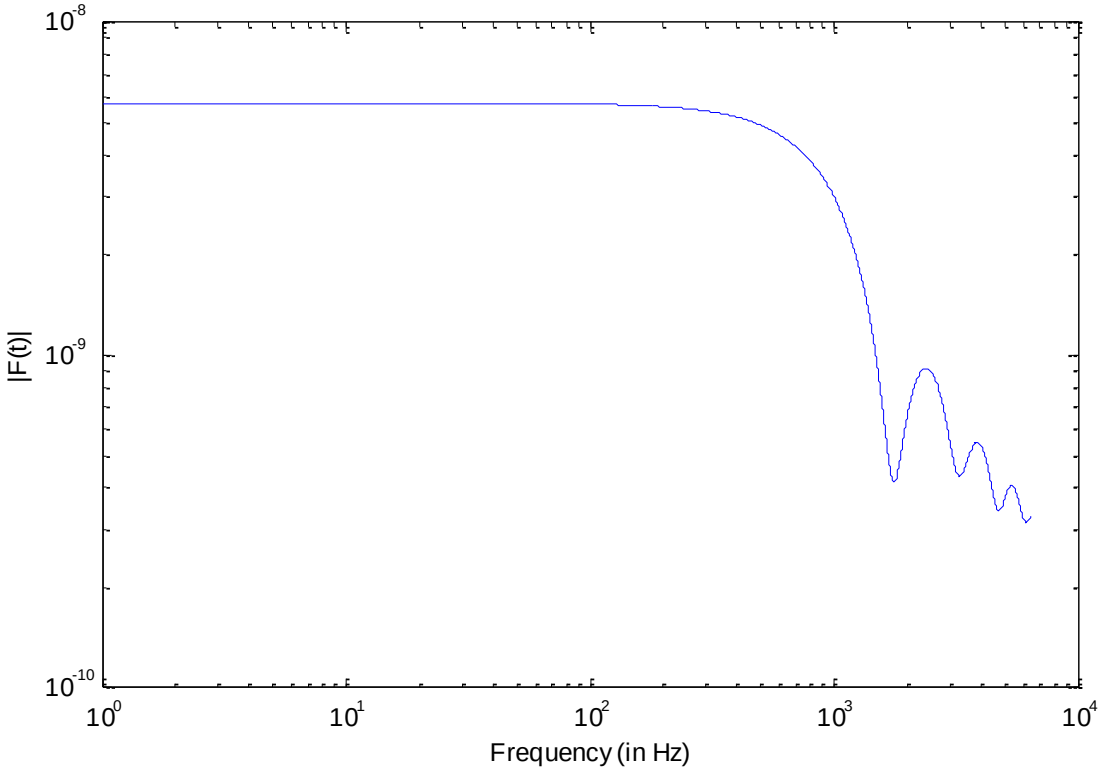

Figure 9: the simulated force of a raindrop in frequency domain of equivalent diameter 0.2998mm and its terminal velocity $0.3834m/s$ *using Petersson (1995) equation*

In this equation, $t \leq \frac{2r}{3v_0}$ is the duration of the time taken to break the surface tension maintaining the drop shape and the length of the pulse is given by $\frac{5r}{3v_0}$. Figure 8 shows the result of the above equation for a raindrop of equivalent diameter $0.2998mm$ and velocity $0.3834m/s$ in the time domain and Figure 9 show the simulated force of the drop in the frequency domain. The time domain representation is sampled at 16khz.

This force of a single drop can then be used to describe a multiple drop scenario. The multiple drop impact can be regarded as a random process making it hard to predict the spatial impact of a rain drop during an event. However, if we were to assume that all drops were of the same size and fell at a specific spatial position, the event can be described as a train of pulses. The pulse length for the different drop varies from $0.2msecs$ to $0.55msecs$ as shown in Figure 10 depending on drop sizes. The reason for the smaller drops taking longer to dissipate on a liquid-solid impact is because of the relatively slower velocity of the drops. The method used for identifying the droplets will be discussed at a later stage in this thesis.

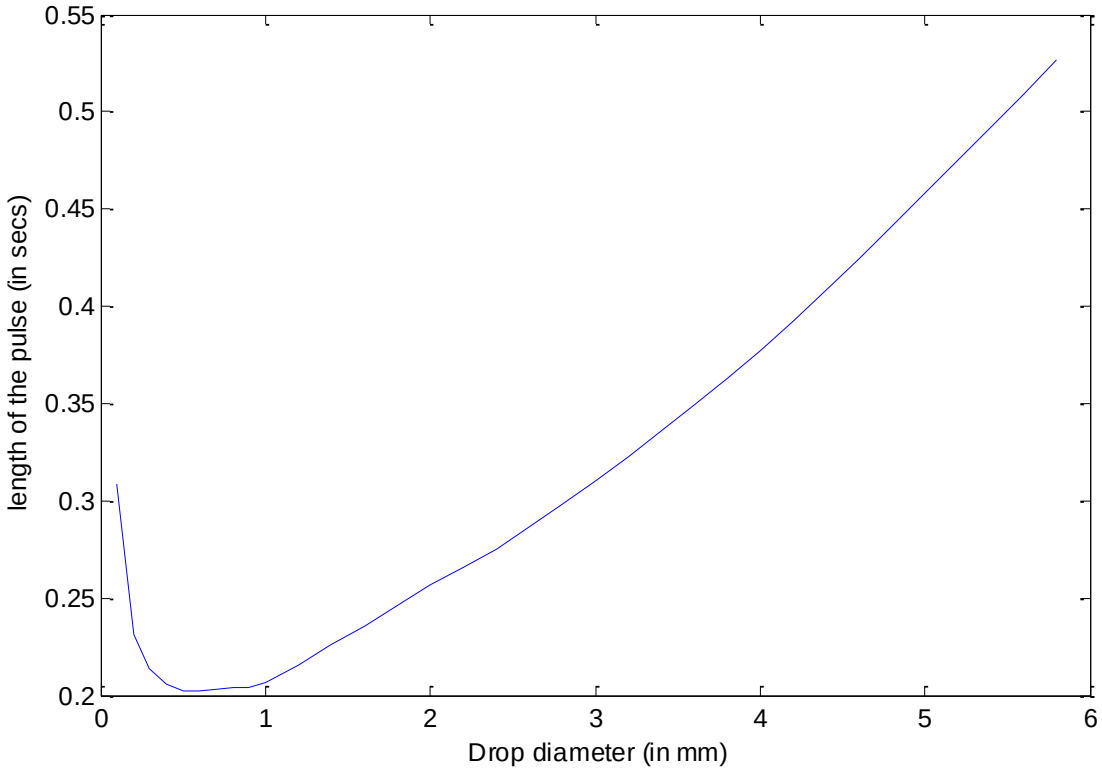

Figure 10: Comparison of pulse length for different drops to the drop diameter at terminal velocity

2.2.4.4 Drop size distribution

Rainfall is a distribution of differently sized drops that attain their corresponding terminal velocity. As mentioned earlier, the drop size distribution is defined as the probability distribution of the number of drops per unit size (expressed in diameter of the drop) and per unit volume of space as measured on the surface of earth. The key assumption on how rain is formed as part of section 2.2.2 is, by a sequence of nucleation plus condensation of ambient water vapour followed by coalescence of the colliding drops allowing for the drop size distribution to be different on the surface in comparison to in the clouds. (Campos, 1999) (Villermaux & Bossa, 2009)

The first empirical description of drop size distribution was given by Marshall and Palmer (Sheppard & Joe, 1994). It showed that raindrop size distribution is a monotonically decreasing function of the size: the number of drops $n(d)$ with size between d and $d + \delta d$ per unit volume of space is

$$n(d) = n_0 e^{-\Lambda d} \qquad 2.8$$

Where n_0 is a constant reflecting the average spatial density of the drops, which depends on temperature and is equal to $0.08\ cm^{-4}$ at ground level and Λ is the average diameter related to the rate of rainfall R in $mm\ h^{-1}$ by

$$\Lambda^{-1} = 41\ R^{-0.21} \qquad 2.9$$

The steepness of the distribution is related to the intensity of the rainfall. Drop sizes are more broadly distributed in heavy storms than in fine mists. This relationship (equation above) was later cross- checked in situ by aircrafts flying through clouds and/ or precipitation, and by more refined measurements exploiting rain's radar echo reflectivity.

2.2.5 Relationship between rain drop size distribution and rain intensity

Now, let's look at the relationship between rain drop size distribution and rain intensity. As the device designed measures the drop size distribution, this relationship will help with calculating the rain intensity during the rain event. Let us consider a circular sensing surface of radius r, its area is given by A_s as shown in the figure.

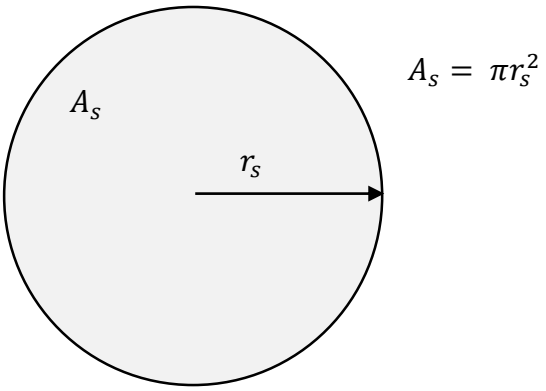

Figure 11: Top view of an impact- type rain sensor of area A_s

Assume all rain drops and droplets are falling vertically at their terminal velocities to the earth's surface. For a given drop size category K, characterized by its terminal velocity $V_{K\,term}$, and N_K is the number of drops detected corresponding to the drop size during the period of analysis t_{int}, then the drop intensity, and the rain rate can be derived as follows.

The drop intensity T_R is the sum of drop intensities T_{KR}:

$$T_R = \sum_K T_{KR} = \sum_K \frac{N_K}{t_{int} A_s} \qquad [drops\ m^{-2} s] \tag{2.10}$$

The rain rate R is given by

$$R = \sum_K R_K = \sum_K \frac{\pi}{6} \frac{D_K^3 N_K}{t_{int} A_s} \qquad [mm\ h^{-1}] \tag{2.11}$$

This method is currently used for deriving the drop intensity and rain rate for existing impact-type rain sensors (for e.g., Joss- Waldvogel disdrometer). These formulae were adapted from (Förster, Gust, & Stolte, 2004).

2.3 General background to vibration

2.3.1 Introduction

In the previous section, a review of rain and techniques used to measure various parameters of rain – rain intensity, drop size distribution and the parameters used to define the dynamics of a rain drop were described. As the chosen method to design the device is to measure the various parameters (rain intensity, drop size distribution) associated with rain by measuring the vibrations associated we are going to look into the background for measuring vibration.

A lot of the previous work done with measuring vibration and its analysis is associated with machines. As we progress through the thesis we will then look to how this can then be used to independently characterise the raindrops falling on the device surface through its active and passive properties – free velocity or blocked force, and mobility or impedance respectively.

2.3.2 Basic definition

In this sub section we are going to introduce the various terms associated with vibration analysis- free velocity, blocked force, mobility, and impedance. Free velocity is defined as "the velocity of the source when all contact zones (connection points) of the machine are ideally free to move" and blocked force as the "force exerted on an ideal rigid foundation point with all contact zones blocked in their movement". Mechanical impedance represents the ratio between the cause of motion (force), and its effect (displacement) with mobility is the reciprocal of mechanical impedance $Y = \frac{1}{Z}$ (ten Wolde & Gadefelt, 1987).

The device developed can be considered to be a linear time invariant system, with the raindrop impact as the input. This input force is converted to an output vibration that is measured by the sensor attached to the plate. A typical linear time invariant system as shown in the Figure 12 can be described in the time and frequency domain.

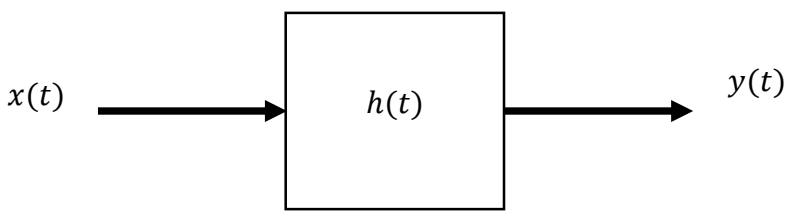

Figure 12: An example of a linear time invariant system

The relationship between the input $x(t)$ and the output $y(t)$ is given by

$$y(t) = \int_{-\infty}^{\infty} x(t - \tau)h(\tau)d\tau$$

$$y(t) = x(t) * h(t) \qquad 2.12$$

where $*$ indicates convolution operator which represents the convolution integral in equation above

On applying Fourier transform, the frequency response functions H for a system is as follows,

$$H(\omega) = \frac{Y(\omega)}{X(\omega)} = \frac{Y\, e^{j\omega t}}{X\, e^{j\omega t}} \qquad 2.13$$

$$Y(\omega) = X(\omega)\ H(\omega) \qquad 2.14$$

where ω denotes radian frequency, t is time and $j = \sqrt{-1}$.

Equation 2.14 is known as the transfer function or frequency response function or Green's function of the linear time invariant system. The direct measurement of forces and moments in comparison to linear and angular acceleration is quite challenging. This is because direct measurement requires the transducer to be inserted between source and receiver; inevitably changing the transmission path. However, consider a system as shown in Figure 13, it is possible to estimate (in principle) the forces on the structure from measured vibration signals from a transducer (for example, in this particular scenario the measured component in acceleration). The acceleration of the structure in the frequency domain due to a force can be related by,

$$A = H_{aF} = \frac{a}{F} \qquad 2.15$$

where a is acceleration, A is the accelerance (measureable by a dual channel analyser), and F is the measured force by a force transducer.

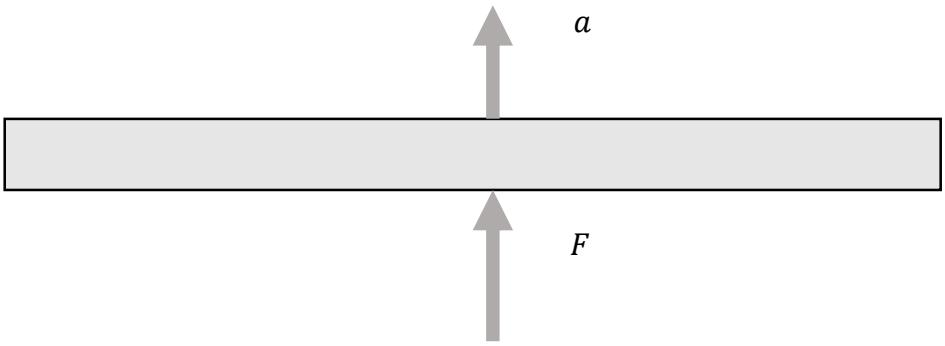

Figure 13: A typical system to measure the acceleration of a plate

The relation between accelerance A and mobility Y is given by,

$$Y = \frac{A}{j\omega} \tag{2.16}$$

The mobility Y is related to velocity $v = \frac{a}{j\omega}$ and input force F by

$$Y = H_{vF} = \frac{v}{F} \tag{2.17}$$

Finally, the mechanical impedance Z which is also referred to as the receptance R of the plate is given by

$$Z = R = H_{xf} = \frac{x}{F} \tag{2.18}$$

The mathematics of the transfer function shows a clean relationship, however this is not the case. There are several issues that can affect this method of calculation, these include noise or error in measurement, the resonant nature of the structure that affect the transfer function. The magnitude of $H(\omega)$ consists of a number of resonant peaks separated by anti- resonance regions. These anti- resonance regions also affect the measured signal $Y(\omega)$. Before getting into detail on the different types of errors, Let us discuss the three methods for calculation of excitation forces, these include modal model, spatial model, and transfer function approach. The modal and spatial model are discussed to highlight their usefulness for vibration analysis and will not be used as part of this research.

2.3.3 Modal model

Modal analysis is the more traditional approach to vibrational analysis wherein "the process involved in testing components or structures is to obtain a mathematical description of their dynamic behaviour" (Ewins, 1986). Similar to representing a complicated waveform as a combination of sine and cosine waves, the mathematical response of the structure is expressed as a sum of the natural modes of vibration of the structure. These natural modes are inherent and can be calculated from by the mass, stiffness, and damping of the structure. Each mode is described by its: natural frequency, modal damping factor, and mode shape. (He & Fu, 2001).

"A structure can be described in terms of its spatial properties of mass, damping and stiffness. This can be the basis of the finite element approach, although the derivation of damping terms is generally omitted or treated separately"(Dobson & Rider, 1990). Here we look to use modal model for force identification, to which an adequate model of the system dynamics is required. The frequency domain response of the system should a number of resonant peaks that indicate the vibration modes, the equation below describes a standard equation of dynamics for a structure in its modal coordinates

$$[M]\{\ddot{q}\} + [C]\{\dot{q}\} + [K]\{q\} = [\emptyset]^T\{F\} \quad 2.19$$

$$\{\ddot{x}\} = [\emptyset]\{\ddot{q}\} \quad 2.20$$

where, $[M]$ is the modal mass matrix,$[C]$ is the viscous damping matrix, and $[K]$ is the stiffness matrix; These are diagonal matrices; $\{q\}$ is the nodal displacement vector in modal coordinates and $[\emptyset]$ is the eigenvectors matrix (Briggs, 1991).

This method is also called as the spatial model method (Dobson & Rider, 1990). Mathematical convenience is the main reason for using modal coordinates instead of actual system coordinates making computation easier. The modal force identification technique has its advantages, having a reduced amount of computation requirements. However, in order to accomplish this a good modal model of the system is required to apply the technique. Any errors in the model will result in a systematic error of the predicted forces (Briggs, 1991).

An alternative method is to describe the dynamic behaviour of the linear structure using a model which is based upon hysteretic damping (to reduce mathematical complexity) in terms of the natural frequencies, associated mode shapes and damping. The three matrices are $[\omega^2]$ is a diagonal matrix of the natural undamped angular frequencies and is called the spectral matrix,

$[\Phi]$ is the modal matrix in which the mode shapes corresponding to each natural frequency are written column by column, with the N columns corresponding to the N natural frequencies of the system and N rows corresponding to the number of degrees of freedom in the model (here the mode shapes are presented as relative displacements at the degrees of freedom and do not represent absolute motion making them scalable against a standard), and $[\eta_r]$ is a diagonal matrix of modal damping or loss factor values in which each term represents a global loss factor for a specific natural frequency (Dobson & Rider, 1990).

Modal models can be developed from experimental frequency response functions since it can be shown that $H_{jk}(\omega)$ is a function of modal properties summed across the modes within the frequency bandwidth. For the hysteretic model, the ratio of the displacement response/ force excitation (receptance) can be expressed by

$$H_{jk}(\omega) = \frac{x_j(\omega)}{f_k(\omega)} = \sum_{r=1}^{N} \frac{\Phi_{jr}\Phi_{kr}}{\omega_r^2 - \omega^2 + \mathrm{j}\eta_r\omega_r^2} \qquad 2.21$$

Where $\Phi_{jr}\ \Phi_{kr} = {}_rA_{jk}$ is the modal constant of the rth mode between the jth and kth degrees of freedom, Φ_{jr} is 'mass normalized modal matrix element for the rth mode at the jth degree of freedom, ω_r is natural angular frequency of the rth mode, η_r is the loss factor of the rth mode, ω is the angular excitation frequency, and N is the total number of modes(Dobson & Rider, 1990).

2.3.4 Transfer function approach

An alternative method to force identification using modal analysis is transfer path analysis more specifically inverse force synthesis. In this method, we use the measured receiver mobility, determined from an uncoupled source and receiver to calculate the operational forces acting on the receiver when the source and receivers are coupled. However, you cannot independently define the velocity of the source and receiver and the forces acting at their interfaces since they are interdependent. The process used in this particular research will be discussed at a later stage as part of this thesis.

As mentioned earlier, the contact force F and contact velocity v are linked to the mobility Y as (ignoring the frequency dependence for conciseness)

$$v = Y\ F \qquad 2.22$$

In this particular scenario a point source (raindrop impact), connected to a receiver structure exerts a point force at the interface which excites the receiver is given by

$$F = Y^{-1}v \qquad 2.23$$

This leads to a three step procedure also known as the matrix inversion method for obtaining the contact force that includes

- Measurement of the mobility response of the uncoupled receiver structure, by applying forces at each of the contact positions.
- Measuring the velocities at the same response positions on impact of the rain drop.
- Calculating the force of the rain drop using equation above.

2.3.5 Relationship between the models

Figure 14 shows the interrelation between the three forms of model, and how they can be transformed between each other. The transformation between experimental model to the spatial domain is sometimes not accurate because the modal model derived doesn't have its measurement sites equal to the observed natural frequencies.

As a consequence the modal matrices are not square making it impossible to represent the mass-normalized modal matrices to be represented as follows.

$$[M] = [\Phi]^{-\mathrm{T}}[\Phi]^{-1}$$
$$[K] = [\Phi]^{-\mathrm{T}}[\omega_r^2][\Phi]^{-1}$$
$$[H] = [\Phi]^{-\mathrm{T}}[\eta_r\omega_r^2][\Phi]^{-1}$$

Where $[M]$ is a $N \times N$ mass matrix, $[K]$is a $N \times N$ stiffness matrix, and $[H]$is a $N \times N$ damping matrix. However, by specifying the number of measurement sites equal to the number of modes to define an 'equivalent' spatial model the resulting matrices in comparison to the finite element model will have little physical significance(Dobson & Rider, 1990).

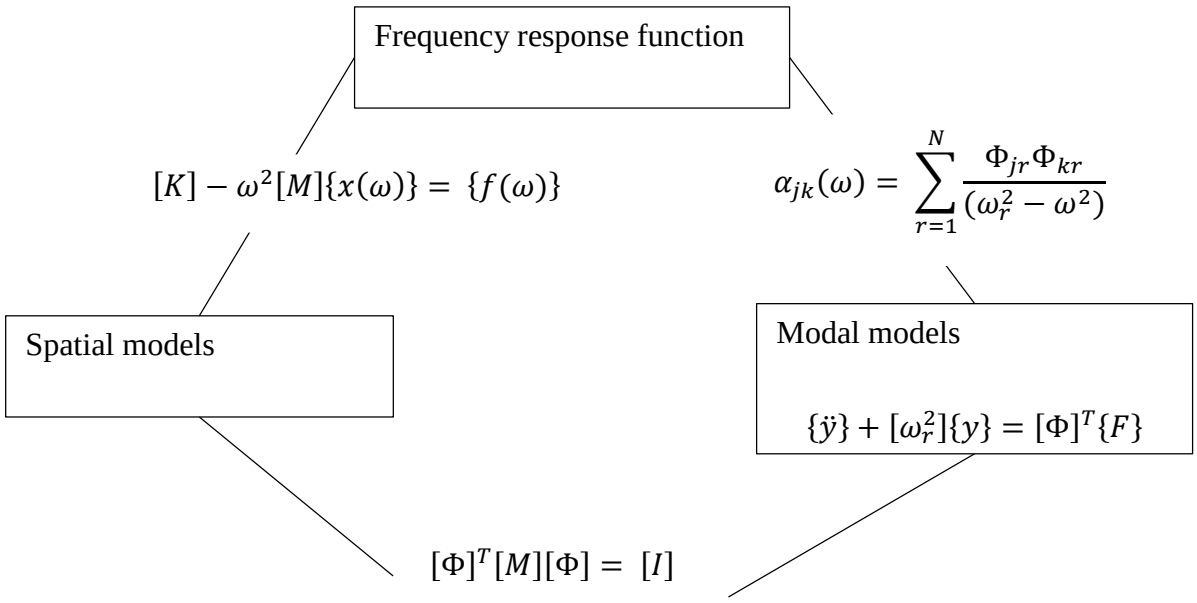

Figure 14: Relationship between the models adapted from Dobson and Rider (1990)

2.3.6 Errors associated with inverse force analysis

There are two types of error that affect the measurements using inverse force analysis, these include statistical errors (or random errors), and systematic errors (or deterministic errors). It is hard to distinguish these errors as the sources for statistical error in one experiment may cause systematic error in another (Taylor, 1997). The treatment of random errors is different from that of systematic errors. The statistical methods described in the following sections give a reliable estimate of random uncertainties, and, as we shall see, provide a well- defined procedure for reducing them.

2.3.6.1 Statistical errors

It can be defined as "the (unknown) difference between the retained value and the true value. It is immediately associated with accuracy since accuracy is used to mean the inverse of the total error, including bias and variance"("Glossary of Statistical terms," 2002).

In inverse force determination, statistical errors are inevitable and can arise from random noise in FRF estimates and operational response signal, and the propagation of these errors can lead to large mistakes in force estimates. This noisy data in combination with ill conditioned FRF estimates will lead to larger errors in the force estimates. Blau (1999) demonstrated that random

error tends to be evenly distributed over the spectrum of the force and the relative errors are larger for weaker forces.

2.3.6.2 Systematic Error

The second type of error is systematic or deterministic errors and these are harder to quantify. There is no real solution to dealing with systematic error. Most theories simply suggest systematic errors need to be identified and dealt with. Systematic errors tend to arise from calibration error of instruments used, use of incorrect value for calculations, or flaw in the design of experiment (Taylor, 1997). Höller (2013) in his research enlists the different sources of systematic errors for inverse force synthesis as follows

- Non- linear behaviour of receiver structure
- Neglected degrees of freedom in the FRF matrix
- Excitation misalignment during FRF measurements
- Sensor mass loading
- Inconsistencies between elements of the FRF matrix, due to changing conditions during multi- run measurements

2.4 Designing the sensor

2.4.1 Introduction

In the previous section, we looked into the general background to vibration and the different methods for force identification and the errors associated in this method. In this section we look to understand the principles for designing a sensor and will look to provide a review of the different technologies available.

As mentioned earlier, currently most electrical rain measuring devices contain separate components for sensing, data acquisition, data logging and a power supply. With the advances seen in Very Large Scale Integration (VLSI), Micro Electromechanical Systems (MEMS) and wireless communication has allowed for the development of low cost, scalable devices. Thus enabling a change of approach in monitoring of buildings, environment, transport systems, industrial equipment, healthcare and a host of other applications resulting in a sensor-rich world. Electronic sensors have rapidly evolved from wired power systems to intelligent, wireless sensors that can be deployed throughout the environment as “deploy and forget” with

functioning limited by the initial energy capacity of the battery available to the system (Mathuna, O'Donnell, Martinez-Catala, Rohan, & O'Flynn, 2008). The impact of "deploy and forget" functionality is the ability to develop large networks of sensor devices continuously monitoring a system, activity or environment.

These large scale sensor networks can improve the accuracy and density of scientific measurement of a physical phenomenon for example rain whilst continuously gathering data and communicating with each other. This smart environment or ambient intelligence will haver millions of sensors embedded and dramatically improving our understanding of the environment, and the quality of life. A typical smart environment is as depicted in Figure 15.

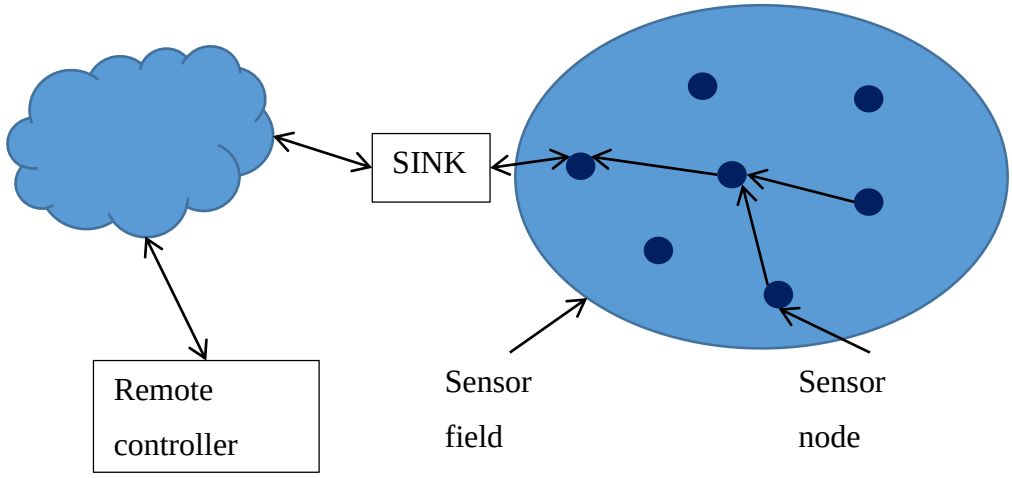

Figure 15: Sensor network architecture adapted from Anastasi, Conti, Di Francesco, and Passarella (2009)

First, let's look at understanding what a sensor is - a sensor is defined as a device that converts a non-electrical physical or chemical quantity into a measurable electrical signal and measurement is the process of evaluating changes in physical and chemical properties of the measurand (e.g. displacement, pressure, gas concentration) to a reference value that can be processed as a method of change (Gardner & Udrea, 1994) . The architecture of a typical sensor is shown in Figure 16 (Kompis & Aliwell, 2008) (Mitcheson, Yeatman, Rao, Holmes, & Green, 2008).

There are four main components to any typical sensor (1) the power source (energy generation and storage), (2) the sensing mechanism which measures the physical world, (3) processing element which consists of either the microprocessor or microcontroller that processes the measured data and stores in memory and (4) the communication component which consists of the wireless communication method either with other nodes or the outside world.

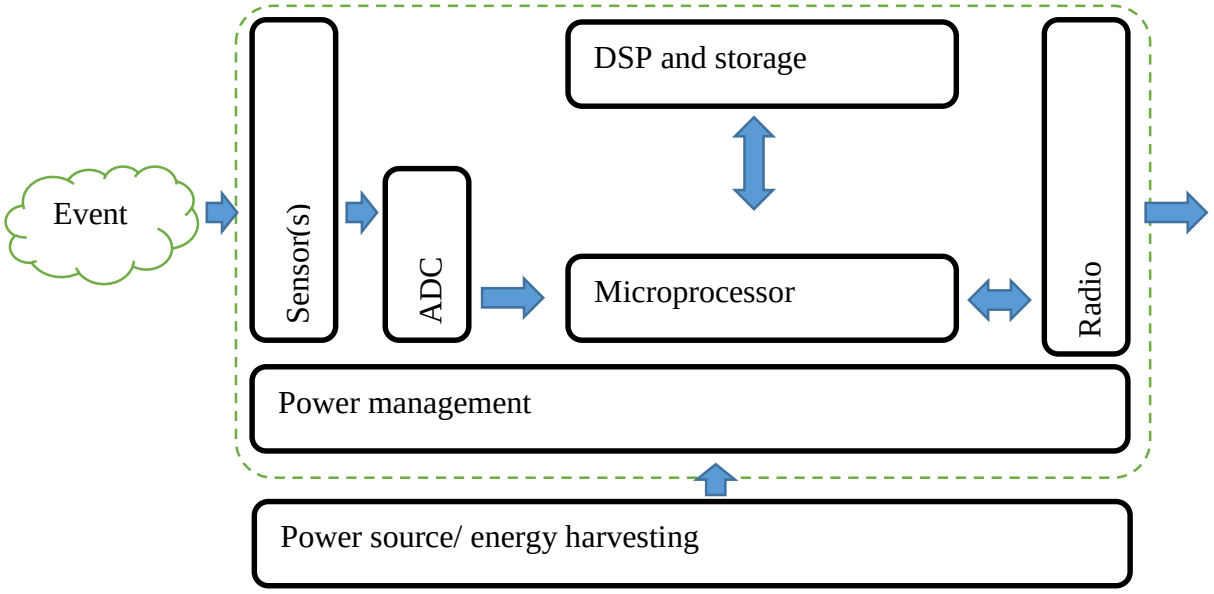

Figure 16: Architecture of a typical smart sensor node adapted from (Kompis & Aliwell, 2008)

2.4.2 Power source and energy harvesting

The power source is an important component of sensor. The source of power for a sensor can come from a battery, or from an energy harvesting solution or a mixture of both and the selection of the power source is affected by several factors that include life-time expectation, available energy sources, and type of energy store (Weddell, Harris, & White, 2008). Currently, batteries are the main source of electrical power for a compact, low- power, and portable electronic device. There are basically two main types of batteries –

- Primary (disposable): Primary batteries use up their chemicals in an irreversible reaction and can be used only once.
- Secondary (rechargeable): Secondary batteries, the chemical reactions used are reversible. They can be recharged by running a charging current through the battery (in the opposite direction). They offer a high energy density at a low cost. Discharge rate and the amount of current drawn from the battery is the most important factor that affects battery lifetime. The

degradation of battery life can be controlled by limiting the amount of current drawn from it.

The different types of commercially available batteries are compared in the Table 1. Battery wear out with time and regular replacement is part of maintenance which is time consuming, uneconomical, unmanageable and may also be impractical (Kompis & Aliwell, 2008).

	$NiCd$	Lead acid	$NiMH$	$Li-ion$	Reusable alkaline	$Li-ion$ polymer
Gravimetric Energy density (Wh/kg)	45-80	30-50	60-120	110-160	80 (initial)	100-130
Cycle life (to 80% of initial capacity)	1500	200 to 300	300 to 500	500 to 1000	50 (to 50%)	300 to 500
Typical fast charge time	1h	8-16h	2-4h	2-4h	2-3h	2-4h
Overcharge tolerance	Moderate	High	Low	Very low	Moderate	Low
Nominal cell voltage	1.25V	2V	1.25V	3.6V	1.5V	3.6V
Load current - peak -best result	 20C 1C	 5C 0.2C	 5C <0.5C	 >2C <1C	 0.5C <0.2C	 >2C <1C
Operating temperature (in ℃)	-40 to 60	-20 to 60	-20 to 60	-20 to 60	0 to 65	0 to 60

Table 1: Characteristics of commonly used battery types adapted from (Kompis & Aliwell, 2008)

An alternative to the use of batteries is the use of super capacitors, typically capacitors are used in power supply filters. They behave as a rectifier by storing the charge to moderate output voltage and current fluctuations. The operational life of standard capacitors is between $10\ to\ 100$ times the operational life of conventional secondary batteries and are more environmentally friendly (free of heavy metals such as lead and cadmium). Electrochemical double layer capacitors (EDLC) also known as super capacitors or ultra-capacitors can be used for storing energy from energy harvesting mechanisms. They have higher energy density than

standard capacitors, but retain many of their characteristics (e.g. long life, short charging time and low leakage). Contrary to characteristics of rechargeable batteries super capacitors do not require a complex method of charging (however care must be taken in order to extend the life of the electrolyte) or display memory effects. It has no limit on number of charging cycles. The energy storage works for several weeks (some super capacitors can store up to 50% of stored energy even after 3 months, depending on temperature)(Kompis & Aliwell, 2008).

However, power sources tend to be fundamentally energy reservoirs and energy harvesting or energy scavenging to power wireless sensor nodes by utilizing various low grade ambient energy sources such as environmental vibrations, thermal sources, solar, and wind energy converted to electrical energy. They are characterised by power density, depending upon how long the source is in operation. A comparison of the different energy sources is summarised in Table 2.

	Condition	Power Density	Area or volume	Energy/day
Vibration	$1\ m/s^2$	$100\ \mu W/cm^2$	$1cm^3$	$8.64J$
Solar	Outdoors	$7500\ \mu W/cm^2$	$1cm^2$	$324J$ (assuming light is available for 50% of the time)
Solar	Indoors	$100\ \mu W/cm^2$	$1cm^2$	$4.32J$ (assuming light is available for 50% of the time)
Thermal	$\Delta T = 5℃$	$60\ \mu W/cm^2$	$1cm^2$	$2.59J$ (assuming heat is available for 50% of the time)

Table 2: Typical data for various energy harvesting techniques adapted from Mathuna et al. (2008)

The main issue with energy harvesting, is that it suffers from low, variable and unpredictable levels of available power. However, trends in reducing power consumption in electronics and increase in mobile and autonomous devices increases the attractiveness of harvesting techniques. In typical operation conditions the energy generated from off- the- shelf technologies, for example in vibration energy harvesting and indoor photovoltaic, is of the order of $milliwatt$ which may appear restrictively small, but operation over several years; these technologies are comparable with long-life primary batteries, both in terms of provision and the cost per energy unit provided making energy harvesting devices attractive as replacements for batteries in low power wireless electronic devices.

2.4.3 Sensing mechanism

The sensing mechanism is compose transducers that can be defined as devices that produce a measurable response to a change in physical condition, e.g. temperature, pressure, voltage, current, etc. The transducer produces an analogue signal which is converted to a digital signal by the use of an analogue- to digital converter. The transducers can either be active sensors, where the transducer generates an electrical voltage or current proportional to the stimulus provided or passive sensors, where there is a change in passive characteristics (capacitance, resistance, or inductance). The parameters used to characterise different types of sensors are summarised in Table 3 taken from Shieh, Huber, Fleck, and Ashby (2001).

Range	Maximum minus minimum value of the measured stimulus
Resolution	Smallest measureable increment in measured stimulus
Sensing frequency	Maximum frequency of the stimulus which can be detected
Accuracy	Error of measurement in % full scale deflection
Size	Leading dimension or mass of sensor
Operating environment	Operating temperature and environmental conditions
Reliability	Service life in hours or number of cycles of operation
Drift	Long term stability (deviation of measurement over a time period)
Cost	Purchase of cost of sensor

Table 3: Summary of sensor characteristics taken from (Shieh et al., 2001)

For the application of force detection, the principles governing the choice of the sensing mechanism can be listed as follows –

- The device must be large enough to record a representative sample of raindrop during an event.
- The device must not be too large that coincident drops are numerous.
- The device must be sensitive that the same size drop will produce the same response with minor errors at all points on the defined sensing area.
- The sensing mechanism used must be fast to respond to the dynamic impact of raindrops.

There are three main types of method for measuring vibration based on the frequency of the measurements. These include displacement sensors, velocity sensors, and accelerometers. Here

displacement sensors are typically used in a low frequency of measurement and low amplitude displacement applications. The sensors typically yield a measurable output proportional to the relative motion. Velocity sensor find their applications in low to medium frequency, and accelerometers find applications in high frequency measurement applications (Morris, 2001).

These sensors can be of made of different technologies. Piezoresistive based sensors, are made from semiconductor material, wherein the resistance of the material changes greatly when the sensor is either compressed or stretched. These devices are typically used as strain gauges. Capacitive based sensors, are sensors typically are constructed using two parallel metal plates with a dielectric (air or some medium) in between them. Here compression between the plate causes a change between the relative permittivity ε_r of the dielectric and hence the capacitance C.

$$C = {\varepsilon_0 \varepsilon_r A}/{d_p} \qquad 2.24$$

ε_0 is the absolute permittivity, d_p is the distance between the plate and A is the area of the plate. Piezoresistive and capacitive sensors are typically used as displacement sensor. Finally, piezoelectric based sensors – where mechanical strain on the material causes it to be electrically polarized (The degree of polarization is proportional to the applied strain). This effect is exhibited naturally in quartz (SiO_2), other synthetic piezoelectric materials include barium titante ($BaTiO_4$), Lead zirconate titante (PZT), Piezoceramics, and PVDF film (Morris, 2001).

2.4.4 Processing

The processing unit for a sensor node is a microcontroller unit which has a small storage unit and performs tasks such as data acquisition, data processing, and controls the functionality of the radio unit for the sensor. The choice of this component affects the size and the device and the overall power consumption of the device. There are many commercial chip manufacturers offering low cost, and low power processors having their energy consumption typically in the range of $12pJ/instruction$ (Gilbert & Balouchi, 2008).

Yu, Qinghua, and Xiyuan (2010) conducted a review of the many commercially available microcontroller units. Amongst them, the MSP430 family of 16-bit ultra-low-power microcontroller (Texas Instruments) and the ATmega family of 8-bit microcontroller (Atmel

Corporation) are most commonly used. The following table provides a comparison of the different microcontrollers over the different selection parameters.

	MSP430 F2618	MSP430 F1611	MSP430 F149	ATmega 128L
Supply voltage (V)	1.8- 3.6	1.8- 3.6	1.8- 3.6	2.7- 5.5
Frequency (max)	16Mhz	8Mhz	8Mhz	8Mhz
RAM	8 KB	10KB	2 KB	4 KB
Flash	116 KB	48 KB	60 KB	128 KB
Peripherals on chip	WDT, dual 12 bit D/A, dual 12 bit A/D, dual 16 bit timer, three channel DMA, four USCIs, hardware multiplier.	WDT, dual 12 bit D/A, dual 12 bit A/D, dual 16-bit timer, three channel DMA, two USARTs, hardware multiplier	UART, WDT, 12 bit ADC, Timer/compara tor	USRT, WDT, 10 bit ADC, Timer/ comparator
Active current (mA)	0.365 @1Mhz, 2.2V	0.33@1Mhz , 2.2V	0.28@ 1Mhz, 2.2V	20.0@ 8Mhz, 5V
Standby current (μA)	0.5	1.1	1.6	20.0
Off current (μA)	0.1	0.2	0.1	5.0

Table 4: Comparison of the commercially available MCUs taken from (Yu et al. (2010))

2.4.5 Communication

The communication unit is a transceiver that enables connecting the sensor node to the network. Generally radios are used in the transceivers of industrial sensor nodes. They operate in four different modes transmit, receive, idle, and sleep. As mentioned earlier, the radio unit in a big power consumer of the sensor operation. The factors affecting the power consumption was listed by Kompis and Aliwell (2008) as

- modulation scheme
- data rate
- transmission range
- operational duty cycle

There are several commercially available wireless communication standards currently available, a summary of which is given in Table 5.

	EnOcean	Z-Wave or KNX-RF	ZigBee (802.15.4)	ZigBee (802.15.4)	Bluetooth	WLAN
Frequency ($\boldsymbol{MHz}$)	868	868	868	2400	2400	2400
Data rate $\left(\boldsymbol{kbytes}/\boldsymbol{s}\right)$	125	9.6/20	20	250	720	11,000 – 54,000
Min. telegram length ($\boldsymbol{ms}$)	extremely low	low	low	low	medium	high
Basic load level of frequency band	low	low	low	high	high	high
Risk of data collision	very low	medium	medium	low	very low	high
Optimal solution for	Battery-less wireless sensor systems	Battery powered wireless sensor systems	Battery powered wireless sensor systems	Battery powered wireless sensor systems	Computer networking with printers and PDAs	Computer networking (web, e-mail, video)

Table 5: Comparison of the different commercial wireless protocols available taken from (Kompis and Aliwell (2008))

2.4.6 Signal Processing

Signal processing is an enabler that helps with extracting and processing of the abstract signals to a more useable information. There are different denoising techniques available, traditionally noise is removed from a signal by the use of a filter (Ergen, 2012). It takes in an input signal, processes it, and returns an output signal. The filter is designed using fast Fourier transform techniques. The different types of filters include low pass filter, high pass filter, band pass filter, and band stop filter. The main assumption for the Fourier series method is that every signal can be broken down into it component blocks made of periodic sine and cosine waves added together. This may prove to be disadvantages in cases where the measured signal is not periodic and has a time- independent wave like features (Boggess & Narcowich, 2009) as in this particular case of measuring rain impact pulses.

In order to overcome this issue, we can possibly use Fourier transform for a shorter time window length instead of applying the Fourier transform to the entire signal. However, by shortening the window length we sacrifice the frequency resolution of the signal in order to capture the transient behaviour of rain. An alternative technique is the use of wavelet transforms

where the signal is decomposed into scales that represent different frequency bands, and at each scale, the position of signal's instantaneous structures can be determined approximately.

2.5 Summary

This chapter forms the literature review. Here we looked into gaining an understanding of the process of rain formation, and the various techniques currently used for measuring various rain parameters that include – amount of rain, rain intensity and drop size distribution. We also focussed on understanding the dynamics of rain which included- maximum size and volume of raindrops, terminal velocity of raindrops, force of a raindrop and the relationship between the rain intensity and drop size distribution. Following this, we looked at understanding the basics of vibration analysis, and how key concepts – frequency model, and modal model can be used for inverse force identification. This concept becomes useful for identifying the impact force of the rain drop. Finally, we looked at the different types of sensor architecture available and the selection parameters for designing a sensor.

In the next chapter we look into the first set of experiments for designing the device which is to characterise the response of the transducer – plate arrangement for force identification using frequency model method.

3 Characterisation of the plate

3.1 Introduction

In the previous chapter, as part of the literature review we looked to describe what rain is, provide a general background to vibration analysis, and sensor design. As mentioned earlier, as part of this research we look to compute drop size distribution and rain intensity by measuring the vibrations caused on a clamped plate using a thin film piezo film. The first set of experiments included, to characterise the response of the transducer – plate arrangement for force identification using frequency model method.

This experiment consists of three main parts – variation of frequency response function based on thickness of the plate, diameter of the plate, and spatially across the surface of the plate. The chapter will discuss the experimental setup, provide details on the calibration of the sensors used as part of the experiment, and provide a background to what is measured and a discussion on the results.

3.2 Experimental setup

As part of the literature review, there were two methods identified for calculation of the excitation forces – modal model and frequency model. Recent improvements in the quality of measurement techniques has enabled the use of the frequency model method. By measuring the contact force from the hammer, and the velocity of the plate to find the mobility of the plate Y.

The selected transducer is a thin film piezo sensor of dimensions $30mm \times 16mm \times 52\mu m$ ($FDT1\text{-}052K$ by measurement specialities). This sensor has a wide frequency range of operation with a low acoustic impedance and high sensitivity making it the ideal choice for measuring transient water drop impacts. The sensor is attached to abs plastic sheets of thickness $2mm$, $3mm$ and $4mm$. The plates will be clamped by two different diameter rings; $5cm$ and $10cm$. The transducer can be attached to the plate using sticky back tape or the use of quick setting adhesive to the centre of the plate as shown in Figure 17. The selected impact points were $0cm$, $0.5cm$, $1cm$, $1.5cm$, $2cm$, $3cm$, and $4cm$ away from the centre for a plate of diameter $10cm$ as shown in Figure 17 and $0cm$, $0.5cm$, $1cm$, and $1.5cm$ away from the centre for a plate of diameter $5cm$.

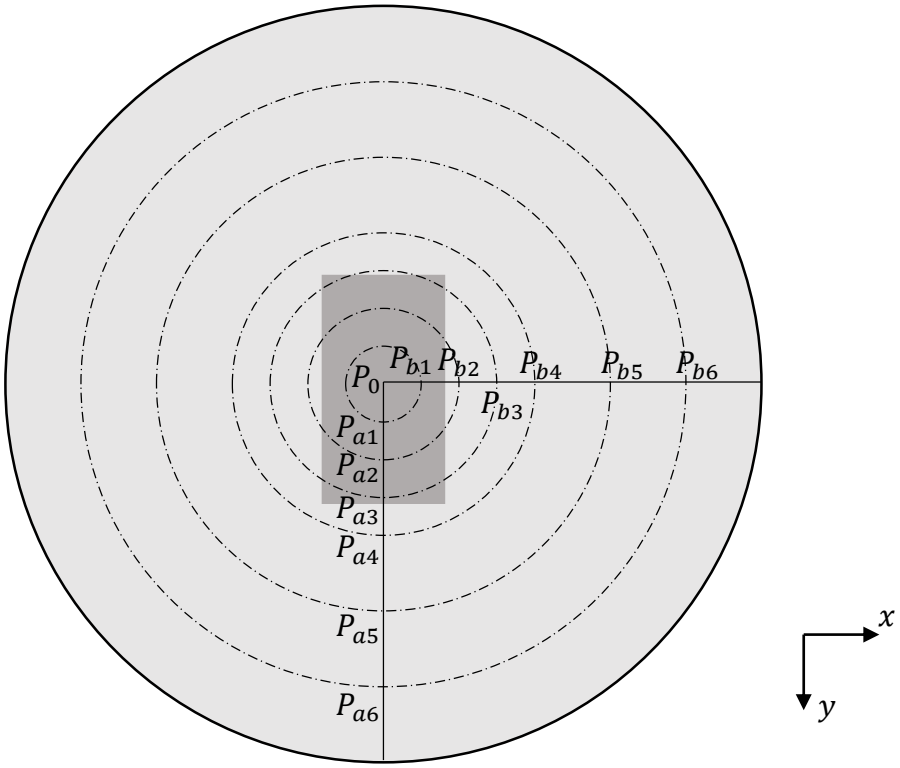

Figure 17: Depiction of the sensor plate arrangement with plate size $100mm$ *with selected points of contact. The transducer is represented by the greyed out area*

The characteristics of the plate (dimensions, elasticity) affects the way the sensor measures the impact forces on the plate. It is for this reason, a built-in force transducer hammer is selected. The output terminals of the transducer and of the hammer with a built-in force transducer connected to a charge co (Bruel & Kjaer, Type 8203, and $2647A$) are connected to a computer through a data acquisition system (Bruel & Kjaer Pulse front-end Type 3560- B- $X07$). The computer controls the pulse front-end, and the data captured is visualised using PULSE LabShop software (by Bruel & Kjaer). A schematic representation of the arrangement is as shown in Figure 18.

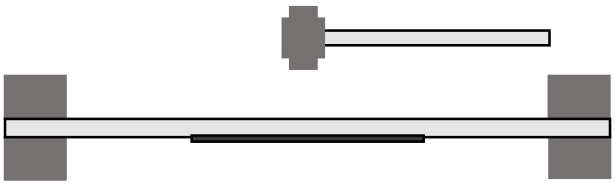

Figure 18: Schematic representation of the experiment to measure the characteristic of the plate

The pulse front-end simultaneously measures and analyses the signals from the two channels. The transducer on the hammer outputs a charge (in coulombs) proportional to its impact force and the connected ICP type charge coupler then converts this charge to a voltage which is measured by the front- end. The force applied by the hammer is therefore given by the sensitivity of the hammer over coupler combination (in $Volts/Newton$) and the output of the transducer on the sensor plate arrangement was simultaneously recorded in $Volts$. The multi-channel analyser was set to acquire $1sec$ of data sampled at $16khz$ and the fast Fourier transform calculations were set for 6400 lines of narrow band frequency. The resolution selected for the measurement, provides for adequate mapping of the amplitude of the input voltage signal from the thin film piezo sensor.

3.3 Calibration

The force transducer Type 8203 (Bruel & Kjaer) is calibrated at $3.35\ pC/N$ and charge is converted to voltage by the ICP coupler and to force by the Pulse labshop software. The selected transducer is thin film piezo sensor manufactured by Measurement Specialities Inc. Like all piezoelectric materials, on application of a mechanical stress on the film it develops an electrical charge proportional to said stress. The low acoustic impedance of the piezo film makes it a better choice as a sensor in comparison to piezo ceramic devices(Sensor, 2008).

The thin film piezo sensor can be operated in either charge mode or voltage mode. The technical manual(Sensor, 2008) for the sensor provides the details of operation of the device. Under conditions approaching short circuit, the sensor is operated in charge mode and the generated charge density is given by

$$D = Q/A = d_{3n}X_n \quad (n = 1,2, or\ 3) \tag{3.1}$$

The mechanical axis (n) of the applied stress (or strain), by convention, is:

$1 =$ length (or stretch) direction, $2 =$ width (or transverse) direction and

$3 =$ thickness direction

where

D = charge density developed

Q = charge developed

A = conductive electrode area

d_{3n} = appropriate piezoelectric coefficient for the axis of applied stress or strain

n = axis of applied stress or strain

X_n = stress applied in the relevant direction

In open circuit mode (voltage mode), the output voltage of the of the sensor is given by

$$V_0 = g_{3n}X_n th \quad (n = 1,2, or\ 3\ as\ above) \tag{3.2}$$

where

$g =$ appropriate piezoelectric coefficient for the axis of applied stress or strain

$X_n =$ applied stress in the relevant direction

$th =$ the film thickness

The piezo coefficient, d_{3n} and g_{3n} are the most widely used. The first subscript refers to the electrical axis and the second subscript refers to the mechanical axis. Their values are given in Table 6.

Symbol	Parameter	Value	Units
d_{31}	Piezo strain constant	23	$(pC/m^2)/(N/m^2)$
d_{33}		-33	
g_{31}	Piezo stress constant	216	$(mV/m)/(N/m^2)$
g_{33}		-330	

Table 6: Properties of piezo film (Sensor, 2008)

On impact of the hammer on the plate, stress is applied on the sensor mostly in the mechanical 1 direction as shown in Figure 19, the charge or voltage is transferred through the thickness of the film as the electrodes are applied to the top and bottom of the film surfaces.

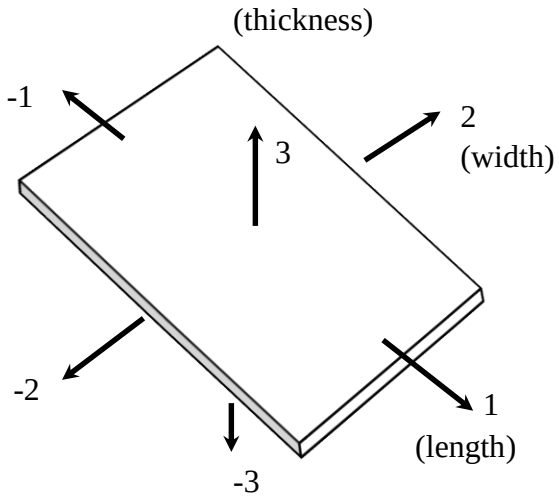

Figure 19: Numerical classification of axes adapted from Sensor (2008)

3.4 Summary of parameters measured

The dual channel analyser (Bruel & Kjaer Pulse front-end Type 3560- B- X07) measures the input from both the channels. For each input, the autospectrum is calculated from the squared averages of the amplitudes of the complex spectrum calculated by forward Fourier transforming the input time function. The dual channel analyser also calculates the cross spectrum and uses this in conjunction with the autospectrum to calculate the frequency response function and the coherence of the signals measured (Randall, 1987). In the following sub-sections we are going to be looking in detail at the cross-spectrum, frequency response functions, and coherence.

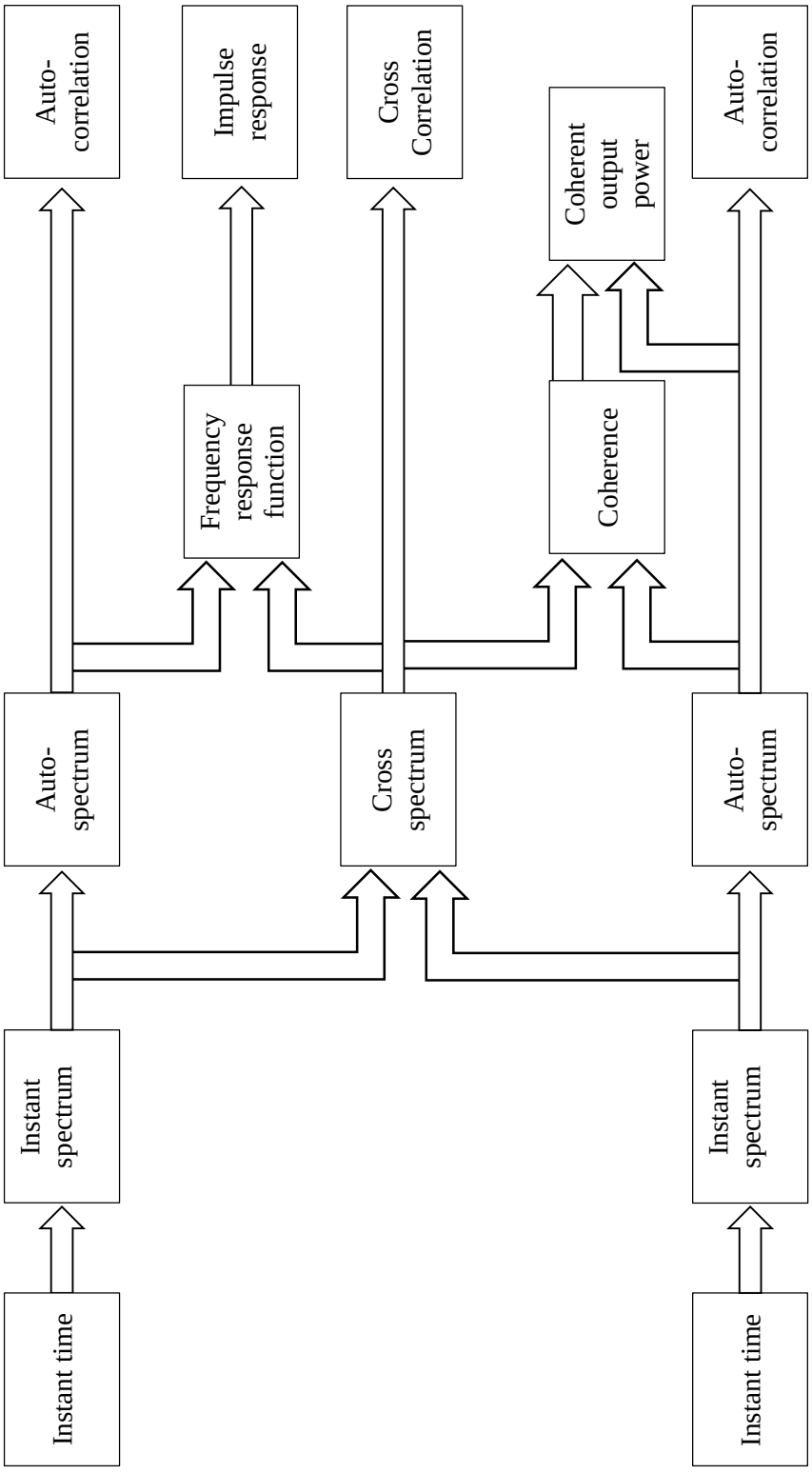

Figure 20: Block diagram for a dual channel FFT analyzer in spectrum averaging mode

3.4.1 Cross-spectrum

The cross-spectrum is a complex function, it is the forward Fourier transform of the cross-correlation function. Consider the instantaneous spectra measured by the dual channel analyser to be $A(f)$ and $B(f)$, the cross spectrum from signal A to signal B is shown in equation below

$$S_{AB}(f) = A^*(f) \cdot B(f)$$

The amplitude of S_{AB} and S_{BA} is the same, however they have opposite phase. The cross-spectrum isn't widely used on its own, but used to calculate other functions (Randall, 1987).

3.4.2 Frequency response

To determine the frequency response function an important use of the dual channel analysis. The frequency response function characterizes a stable, linear time invariant system and is represented by the ratio of the output to the input in the frequency domain. They are also referred to as the "transfer function"(Randall, 1987).

There are three different forms of frequency response functions:

H_1: is the frequency response function calculated as the ratio of the cross-spectrum normalised by the input autospectrum to the input autospectrum.

$$H_1(f) = \frac{G_{AB}(f)}{G_{AA}(f)}$$

H_2: is the frequency response function (FRF) calculated as the ratio of the output autospectrum to the cross-spectrum normalised by the output autospectrum.

$$H_2(f) = \frac{G_{BB}(f)}{G_{BA}(f)}$$

And H_3: is the FRF computed as the average of H_1 and H_2.

Effect of noise on frequency response function

Random noise has an effect on the frequency response function. The propagation of these errors leads to errors in force estimates for inverse force synthesis. To understand the impact of the errors in $H_1$and H_2 calculations and the reason for the selection of H_1 or H_2, we will consider the effect of random noise added at (1) the measured output and (2) the measured input of the system.

Consider an ideal system as shown in Figure 21, here the measured signal $b(t)$ includes the output signal from the system $v(t)$, but also some additive uncorrelated noise $n(t)$. The input autospectrum G_{AB} gives an unbiased estimate of the true cross-spectrum G_{AV} if sufficient averaging is performed. The relation for the output autospectrum for uncorrelated signals is given by the mean squares $G_{BB}(f) = G_{vv}(f) + G_{NN}(f)$

$$H_1(f) = \frac{G_{AB}(f)}{G_{AA}(f)} = \frac{G_{AV}(f)}{G_{AA}(f)} = H(f) \quad 3.3$$

$$H_2(f) = \frac{G_{BB}(f)}{G_{BA}(f)} = \frac{G_{VV}(f)+G_{NN}(f)}{G_{VA}(f)}$$

$$H_2(f) = H(f)\left[1 + \frac{G_{NN}(f)}{G_{VV}(f)}\right] \quad 3.4$$

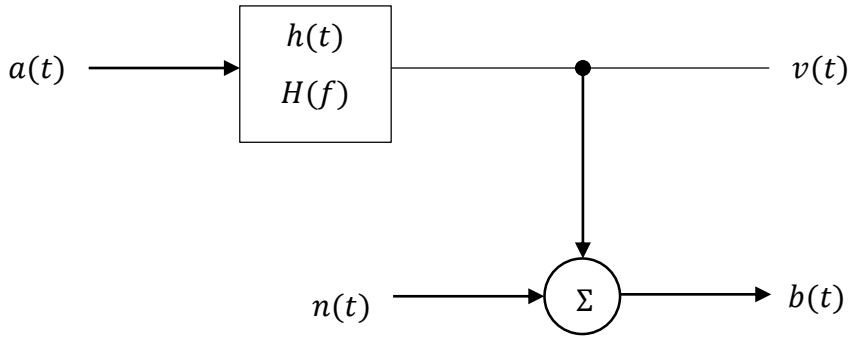

Figure 21: Ideal system with noise added in measured output signal $b(t)$

For the opposite situation, where the random noise $m(t)$ contaminates the measured input signal $a(t)$ is shown in Figure 22. Here, the noise doesn't contribute to the system response $b(t)$.

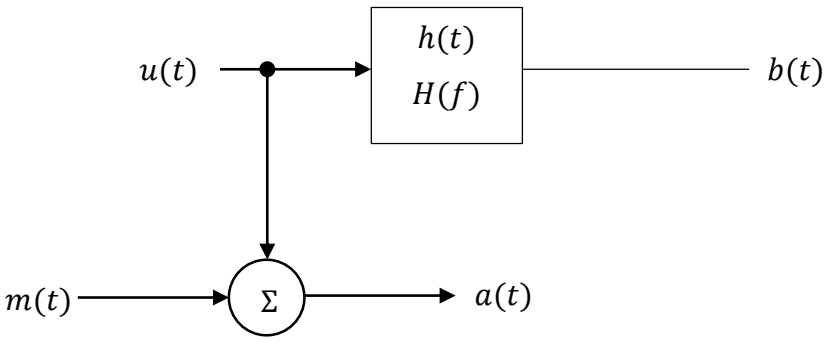

Figure 22: Ideal system with noise added in measured input signal $a(t)$

$$H_1(f) = H(f)\frac{1}{\left[1+\frac{G_{MM}(f)}{G_{UU}(f)}\right]}$$

$$H_2(f) = H(f) \qquad 3.5$$

For a typical situation with noise at both the input and the output, $H_1(f)$ is given by equation 3.7 and $H_2(f)$ is given by equation 3.8. The H_1 technique is best used in situations where noise is present for measuring anti-resonances. Here the signal-to-noise ratio is poor. The H_2 technique is used when noise is present for measuring resonances, the signal-to-noise ratio tends to be the best. And both the methods give the same result when noise is not present in the measurements.

3.4.3 Impulse response

The impulse response of a system is defined as the output of the system when a unit impulse is applied at the input in the time domain. It is calculated by inverse Fourier transforming of the frequency response function. The transform window is selected based on what modes of the frequency response function are required to be fitted. (Randall, 1987).

$$h(t) = \mathcal{F}^{-1}\{H(f)\} \qquad 3.6$$

The selection of window function is critical to the calculation of the impulse response of the system. In this experiment we use a rectangular window function.

3.5 Discussion of results

In this section we will look to discuss the results of the measurements conducted for the different configuration of the sensor plate arrangements and characterise based on the thickness of the plate, size of the clamp ring, and location of impact on the plate.

3.5.1 Variation of sensor- plate arrangement sensitivity – thickness

In this sub section, we are looking to characterise the sensor-plate arrangement based on its thickness. Here we assume that the force acts in the same direction as the positive displacement. The response of the plate is axisymmetric; that is in the plane of the plate, the response depends only on the distance from the drive point.

A detailed derivation of the drive point impedance of an infinite flat plate is enlisted in Junger and Feit (1972)

$$Z_p = \lim_{r \to 0} \frac{F}{-i\omega w(0)} = \frac{4}{\sqrt{3}} \rho_s c_p h^2 \qquad 3.7$$

Where $c_p = [E/\rho_s(1 - v^2)]^{1/2}$

The drive point impedance derived is purely real and frequency independent. Assuming for the same type of material, from this equation we can understand the impedance of the plate is related to the square of the thickness of the plate. The inverse of impedance is mobility, resulting in a thinner plates to be more sensitive to vibration in comparison to thicker plates. The infinite plate theory is introduced here to show there is a relationship between the impedance and the thickness of the plate. The infinite plate theory is inappropriate here is because the first mode of the frequency response measurement occurs at quite a high frequency. The literature review provides us with a transferable understanding. In this particular application of rain sensing and measurement, we look to measure the frequency response function in $Volts/Newtons$ to compare the behaviour the device.

The measured frequency response function (as shown in Figure 24 and Figure 25) demonstrates the change in frequency response for the two different sizes of clamped plate scenario for different thickness of the plates (excitation at the centre of the plate). Figure 24 shows the frequency response function for a plate configuration with clamp setting $50mm$ for different thicknesses and Figure 25 shows the variation of frequency response function for a plate configuration of clamp setting $100mm$. Since the measurements for the different plates were take on different days, the $2mm$ thickness plate has a $20hz$ high pass filter and the $3mm$, $4mm$ thickness plate have a $7hz$ high pass on them. Also, there is a strong $50hz$ component in the measured data. An example of the noise affecting the measurement is shown in Figure 23. In order to mitigate this, the selected frequency range is between $100hz$ to $2000hz$. In this frequency range there is a linear increase in the frequency response function (in $Volts/Newton$) for increasing drop diameter. There are two modal peaks for the 50mm clamp setting and three modal peaks for the 100mm clamp setting. The first modal peak is particularly useful as it behaves as an amplification of the signal measured.

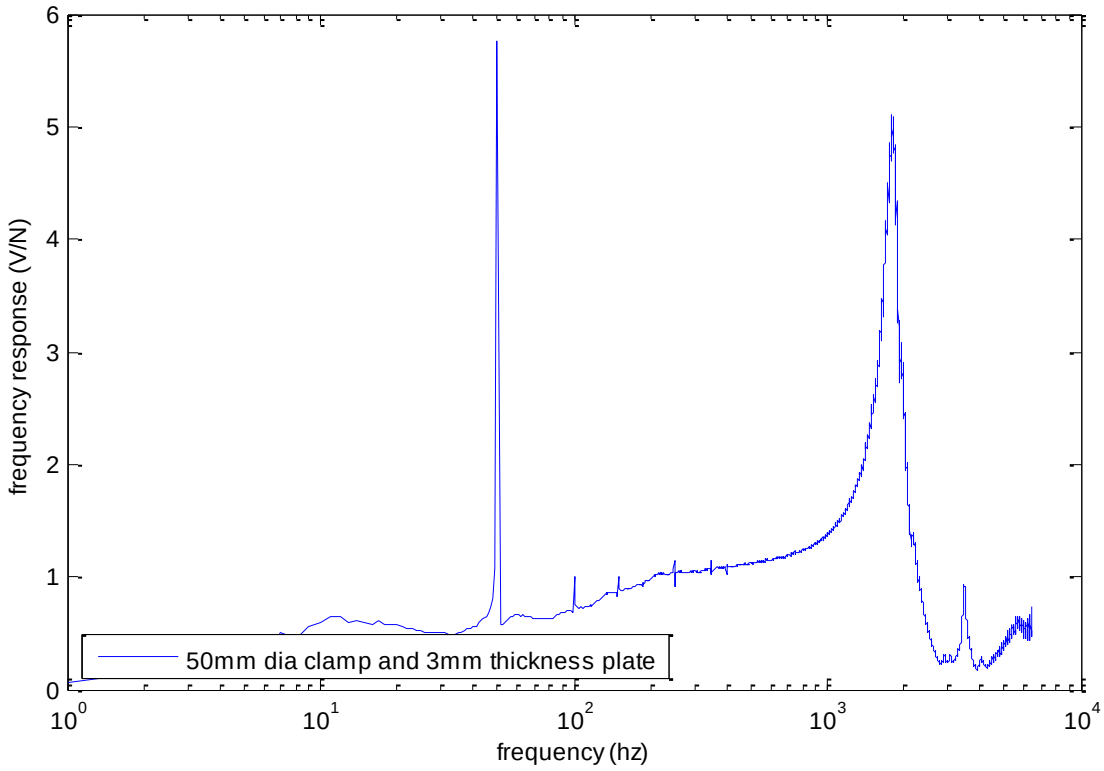

Figure 23: Electrical noise in measurement of frequency response function (in $Volts/Newton$) of transducer- plate arrangement of 50mm diameter clamp and 3mm thickness plate

This is because of the piezo film's capacitive nature that makes it susceptible to electromagnetic interference. The susceptibility to the A.C. mains interference by the film device becomes important, as the measured output signal level is small (Sensor, 2008). By designing appropriate filters (low pass, high pass, or band pass), the electrical noise can be isolated.

As expected, the frequency response function of the thinner plate is higher in comparison to that of the thicker plates. In the case of the device, it must not be too high so that it is susceptible to environmental noise and general building vibrations or too low that a raindrop does not produce a measurable response. The effect of environmental noise will be discussed at a later stage of the thesis.

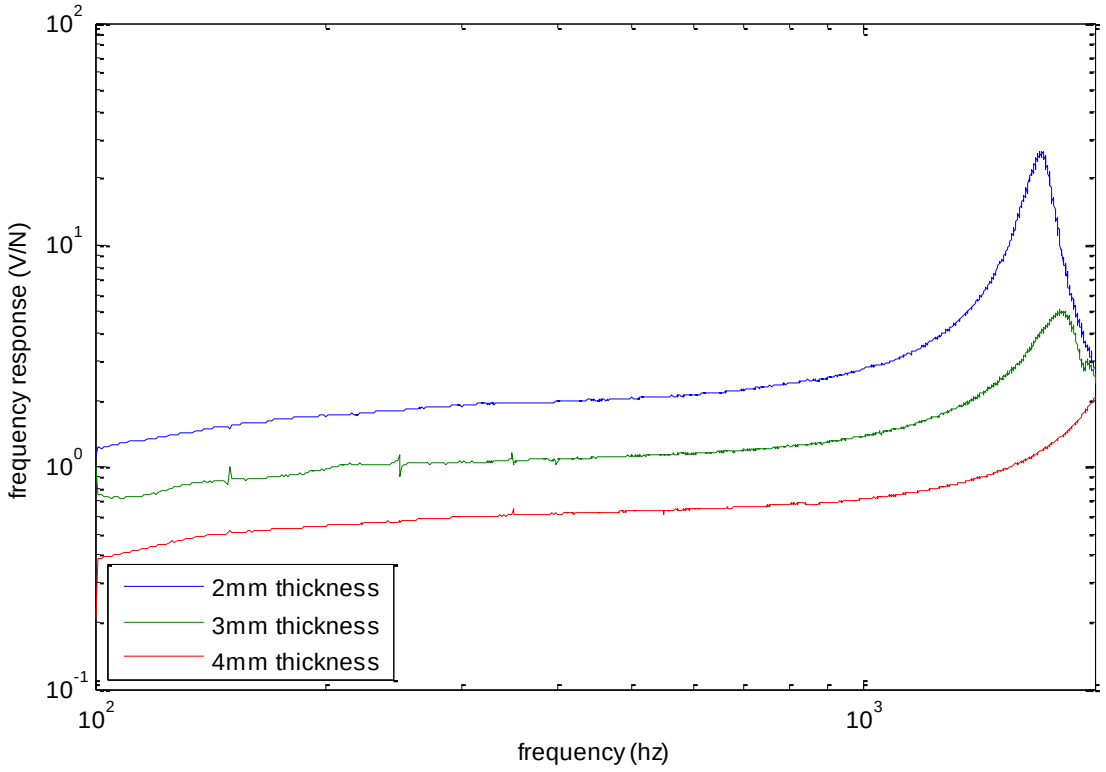

Figure 24: Comparison of frequency response function measured in $Volts/Newton$ for clamped plate of 50mm diameter for different thicknesses at P0

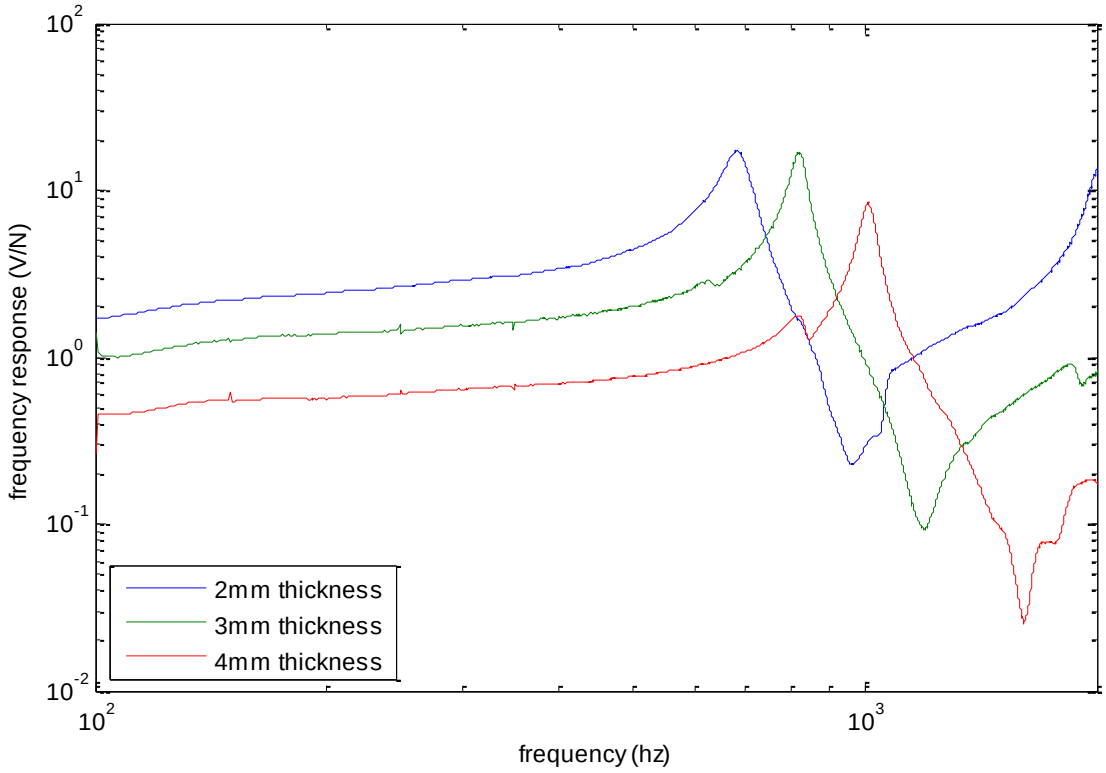

Figure 25: Comparison of frequency response function measured in $Volts/Newton$ for clamped plate of 100mm diameter for different thicknesses at P0

3.5.2 Variation of sensor- plate arrangement sensitivity – diameter

In this sub section, we will look to understand the impact of the size of the clamping arrangement has on the frequency response function of the plate. The clamping arrangement can be of different shapes – rectangular or circular or elliptical or parallelogram plates. The reason for selection of a circular plate as against the other shapes is because of symmetric of the shape, allowing for characterising the plate using lesser number of points. The chosen sizes for comparison was $50mm$ and $100mm$ diameter ring for the different thicknesses ($2mm$, $3mm$ and $4mm$) of plates. In each of the cases, the transducer was attached such that the geometric centre of the transducer is at the geometric centre of the circular plate. The size of the clamp arrangement affects the number of modes. Figure 26, Figure 27 and Figure 28, show the results for the two clamp arrangements for the $2mm$, $3mm$ and $4mm$ thickness plates respectively. The accelerance of the device in V/N is consistently higher in the $100mm$ plate sensor arrangement for the three different thicknesses and has three resonances in comparison to the two for the smaller plate arrangement.

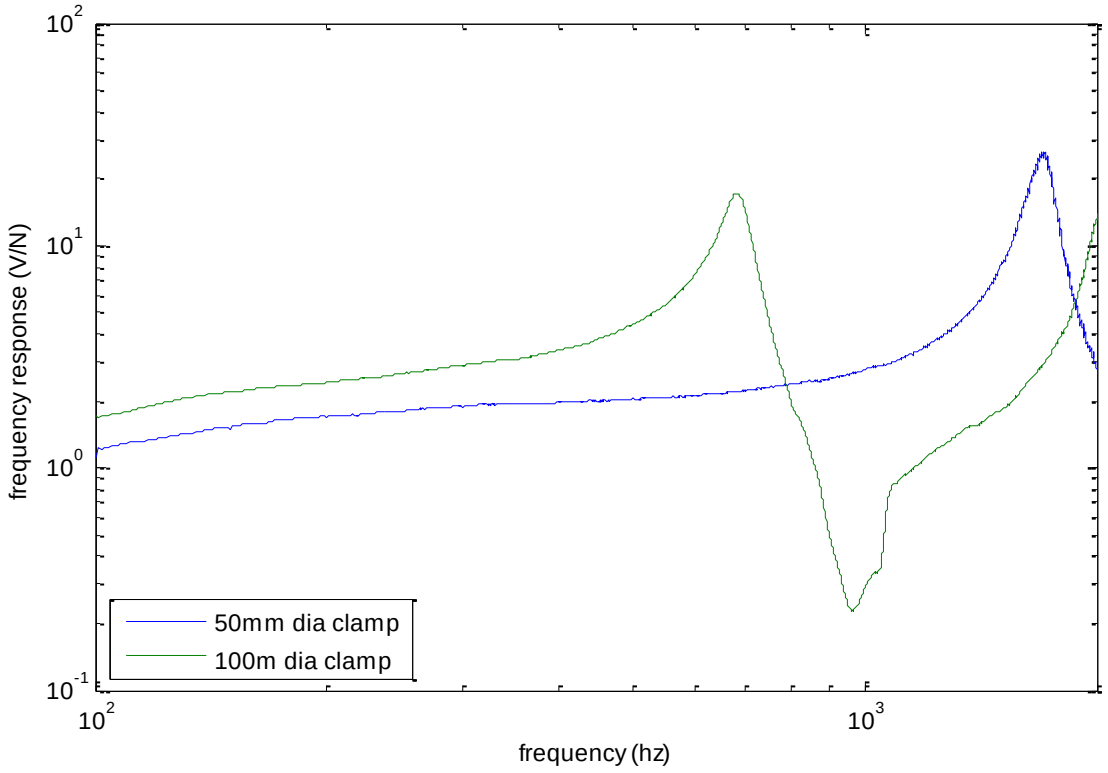

Figure 26: Comparison of the frequency response function measured in $Volts/Newton$ for two clamp arrangements for a plate thickness of $2mm$ at the centre

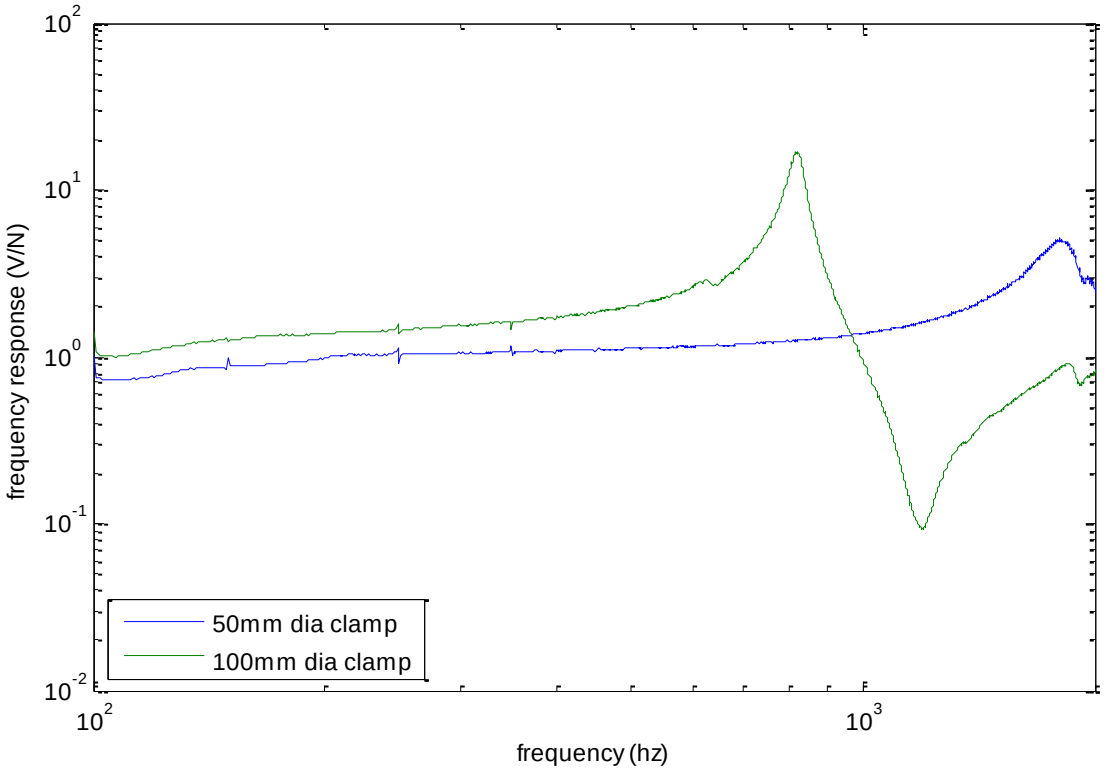

Figure 27: Comparison of the frequency response function measured in $Volts/Newton$ for two clamp arrangements for a plate thickness of 3mm at the centre

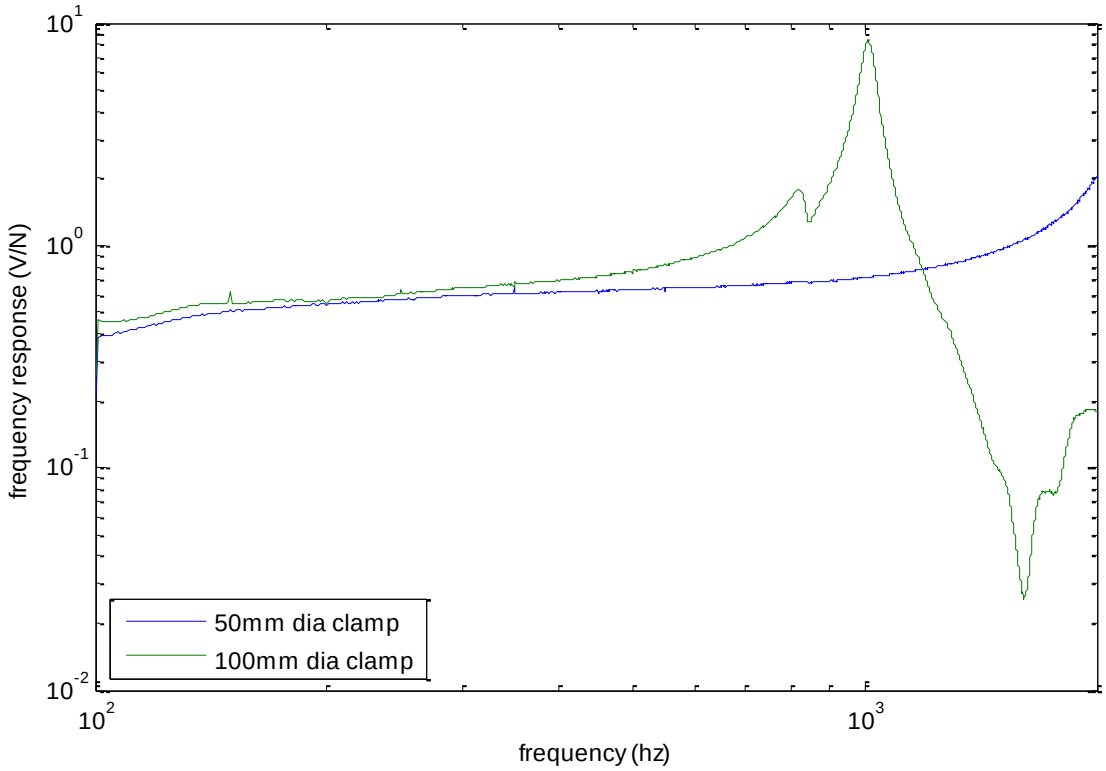

Figure 28: Comparison of the frequency response function measured in $Volts/Newton$ for two clamp arrangements for a plate of thickness 4mm at the centre

3.5.3 Variation of sensor- plate arrangement response – spatial

In this sub section we'll look at the variation of the frequency response function spatially across the surface of the transducer plate arrangement. As shown in equation 3.17, the driving point impedance for an infinite plate of uniform thickness is constant for all frequencies at all x, y coordinate. However with a clamped plate, the response function varies with respect to the position of measurement from the position of the transducer. We would be require to select the number of points required for calibration in order to understand the frequency response behaviour of the clamped plate- sensor arrangement.

In this case, the transducer is attached to the centre of a circular clamped plate arrangement. As shown in Figure 17, due to the construction of the transducer element there are two axes of operation for the sensor plate arrangement. As mentioned earlier, the effective output of the transducer is a resultant of the stress applied by the force across the length and width of the transducer. A summary of the points selected and their respective position from the centre of the circular disc is given in Table 7.

Label	Distance from the center	$\mathbf{5}\boldsymbol{cm}$ clamp	$\mathbf{10}\boldsymbol{cm}$ clamp
$P0$	center	✓	✓
$Pa1, Pb1$	$5mm$	✓	✓
$Pa2, Pb2$	$10mm$	✓	✓
$Pa3, Pb3$	$15mm$	✓	✓
$Pa4, Pb4$	$20mm$		✓
$Pa5, Pb5$	$30mm$		✓
$Pa6, Pa6$	$40mm$		✓

Table 7: Summary of the selected points on the plate- sensor arrangement where a is across the length axis and b is on the width axis

The impact hammer was used to apply a force across the length of the transducer to see the variation of the frequency response function. For the device of $2mm$ thickness plate and $100mm$ clamp plate, the points selected across the length axis are $Pa1$ ($5mm$), $Pa3$ ($15mm$), $Pa4$ ($20mm$) and $Pa6$ ($40mm$). And the points selected across the width axis of the sensor are $Pb1$ ($5mm$), $Pb3$ ($15mm$), $Pb4$ ($20mm$) and $Pb6$ ($40mm$). Figures Figure 29 shows a comparison of the transfer function across and Figure 30 shows a comparison of the transfer function at these points.

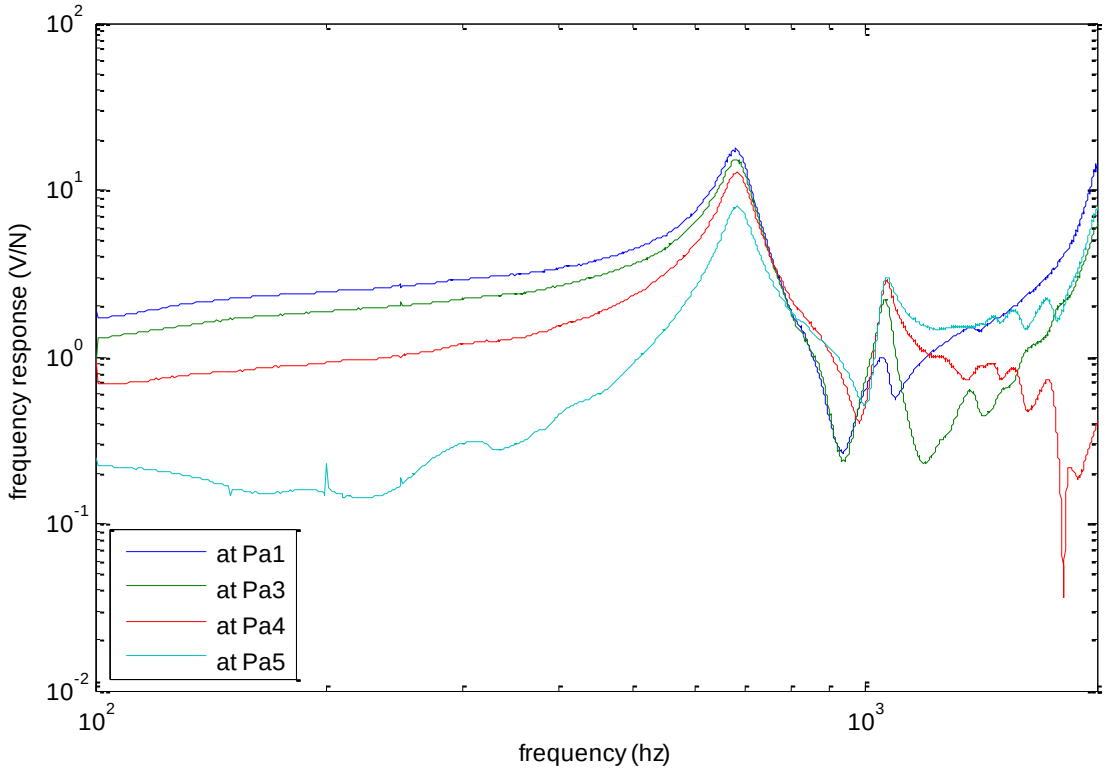

Figure 29: Comparison of the frequency response function measured in $Volts/Newton$ for 100mm clamp and 2mm thickness plate at Pa1, Pa3, Pa4 and Pa5

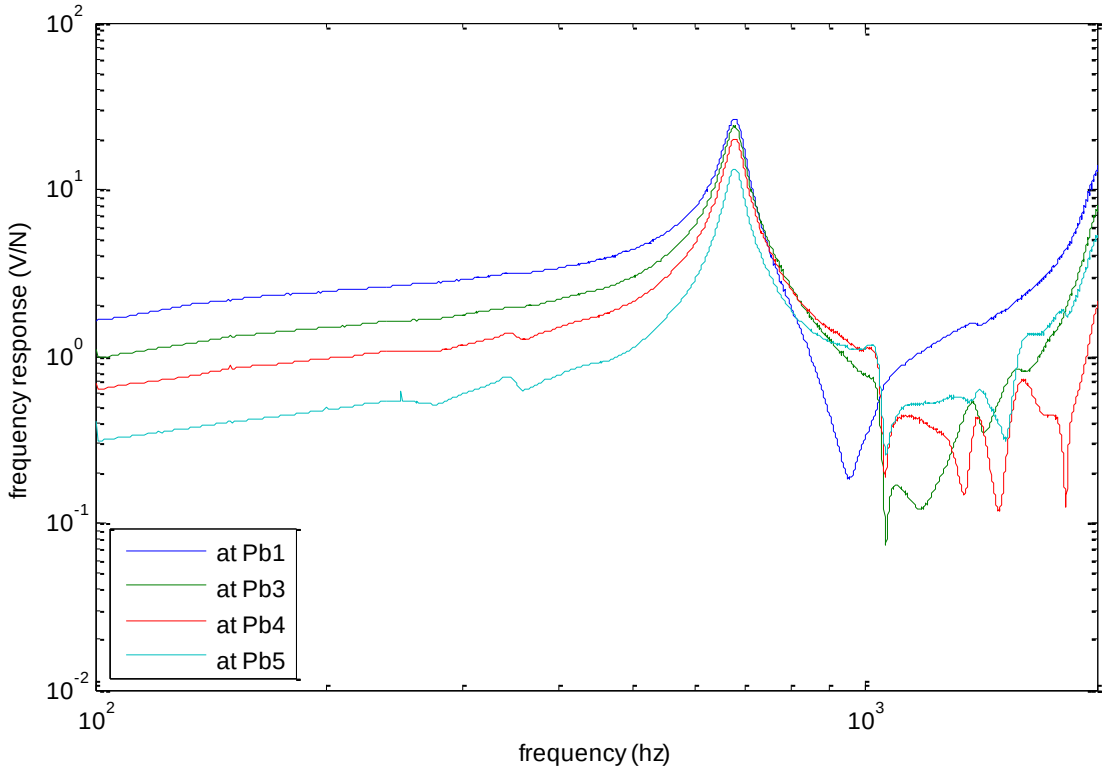

Figure 30: Comparison of the frequency response function measured in $Volts/Newton$ for 100mm clamp and 2mm thickness plate at Pb1, Pb3, Pb4 and Pb5

The frequency response function is expected to reduce in amplitude as we go further away from the transducer located at the centre of the plate. This is because as we go further down the length of the sensor towards the clamped edge, there is a smaller displacement of the plate for the same unit force of excitation and smaller displacement means less strain on the sensor and hence a lower voltage output. This behaviour is also visible across the width axis of the sensor. This may be an issue for potentially underestimating the size of the droplet depending on the location of the impact. This is consistent in both $3mm$ and $4mm$ thickness plates for the similar sized clamp.

In the case of $2mm$ thickness plate and $50mm$ clamp, the points selected across the length axis are $Pa1$ ($5mm$), $Pa2$ ($10mm$) and $Pa3$ ($15mm$). And the points selected across the width axis of the sensor are $Pb1$ ($5mm$), $Pb2$ ($10mm$) and $Pb3$ ($15mm$). It was found that the output of the transducer- plate arrangement was demonstrating the same trend as was seen in the larger clamp arrangement. The amplitude of the response function reduced as we move further away from the centre of the transducer-plate arrangement as is visible in figures Figure 33 and Figure 34. Figure 35 shows the amplitude and the resonance of the frequency response function is the same at a radius of $5mm$ from the centre of the clamp- sensor arrangement. However for the radius of $15mm$ the amplitude of the frequency response function across the width axis is lower than the amplitude of the response function measured across the length axis as shown in Figure 36.

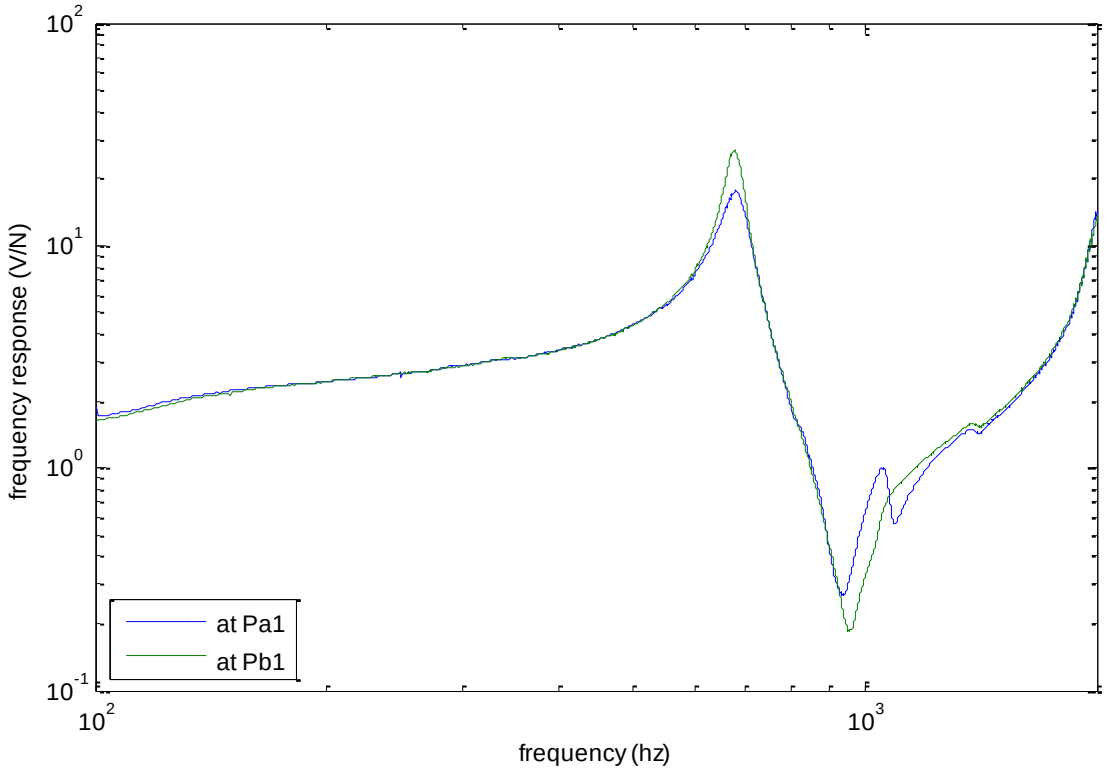

Figure 31: Comparison of the frequency response function measured in $Volts/Newton$ *of the plate of* $2mm$ *thickness and* $100mm$ *diameter clamp at* $5mm$ *from the centre*

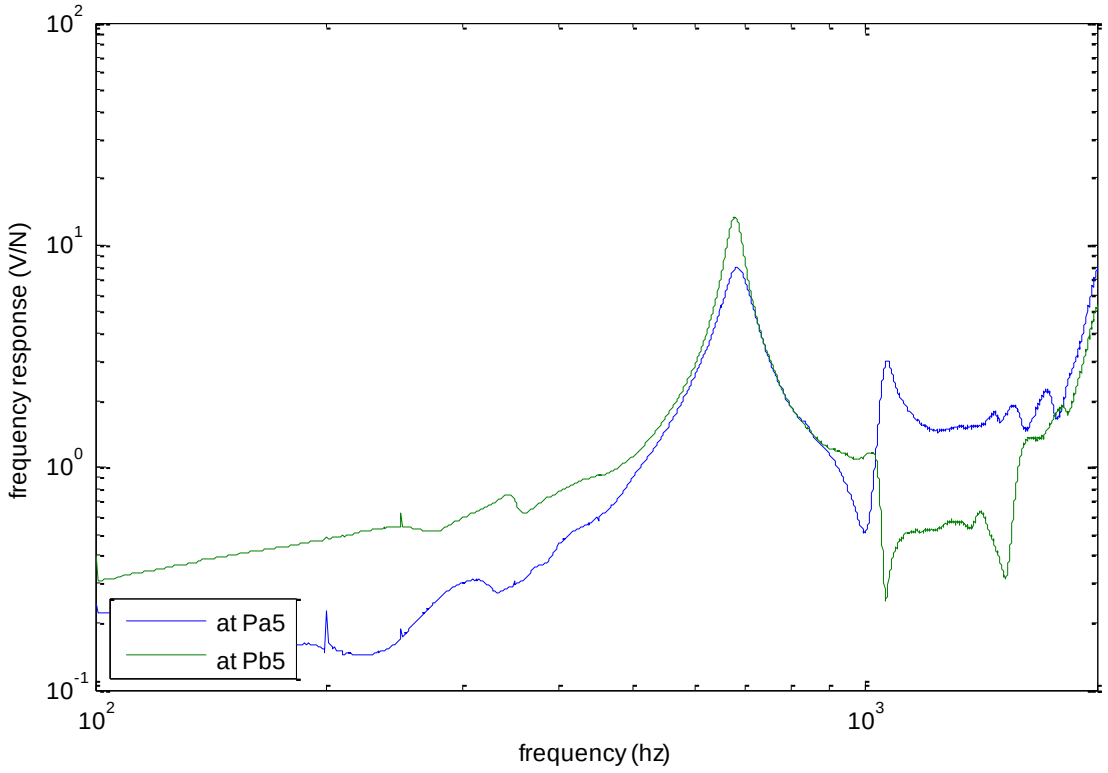

Figure 32: Comparison of the frequency response function measured in $Volts/Newton$ *of the plate of* $2mm$ *thickness and* $100mm$ *diameter clamp at* $30mm$ *from the centre*

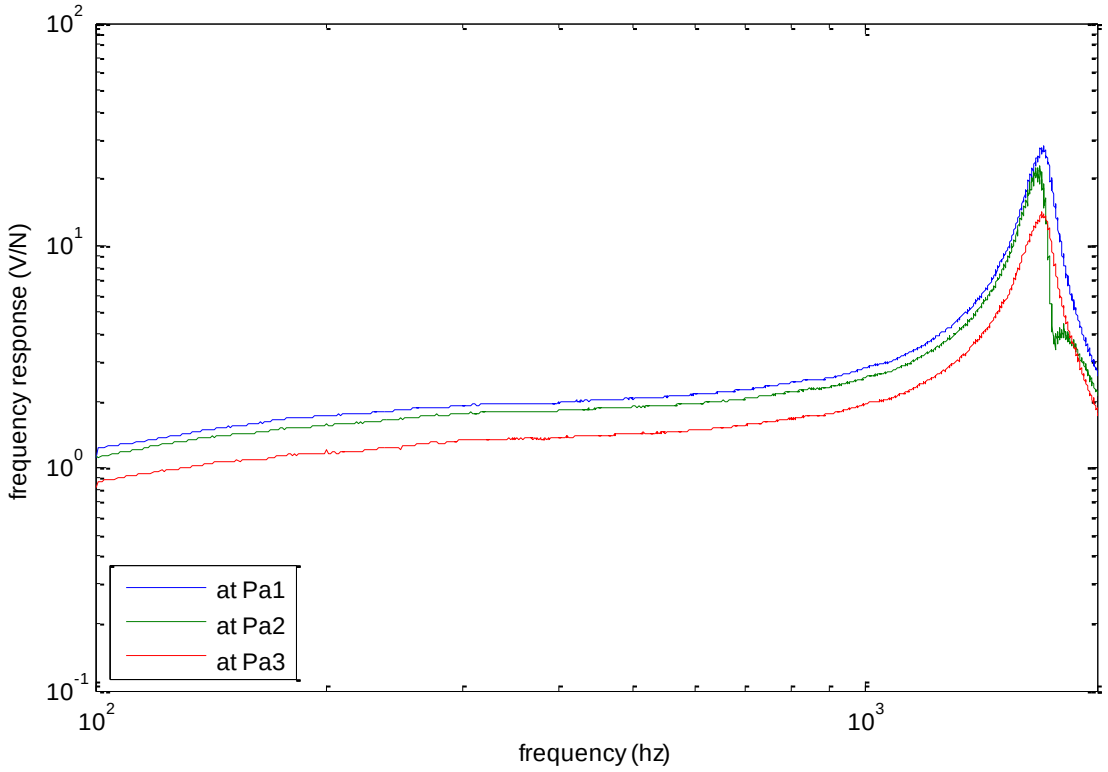

Figure 33: Comparison of the frequency response function measured in $Volts/Newton$ for 50mm clamp and 2mm thickness plate at Pa1, Pa2, and Pa3

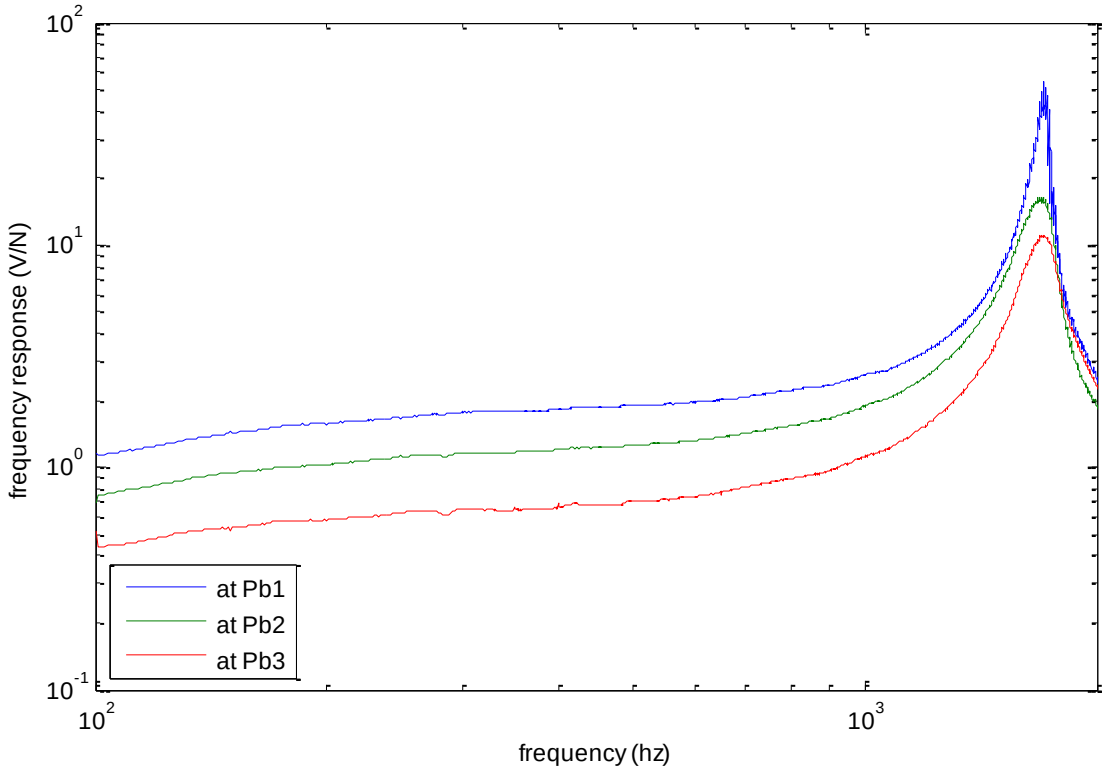

Figure 34: Comparison of the frequency response function measured in $Volts/Newton$ for 50mm clamp and 2mm thickness plate at Pb1, Pb2 and Pb3

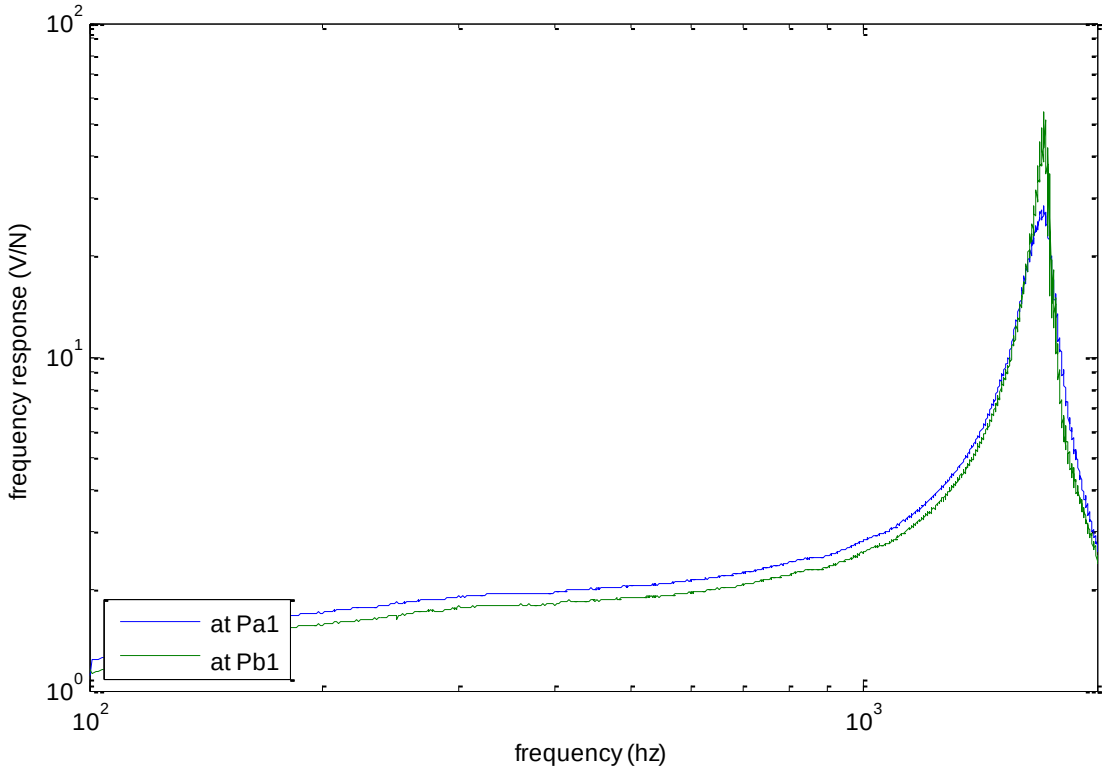

Figure 35: Comparison of the frequency response function measured in $Volts/Newton$ *for* $50mm$ *clamp and* $2mm$ *thickness plate at points Pa1, and Pb1*

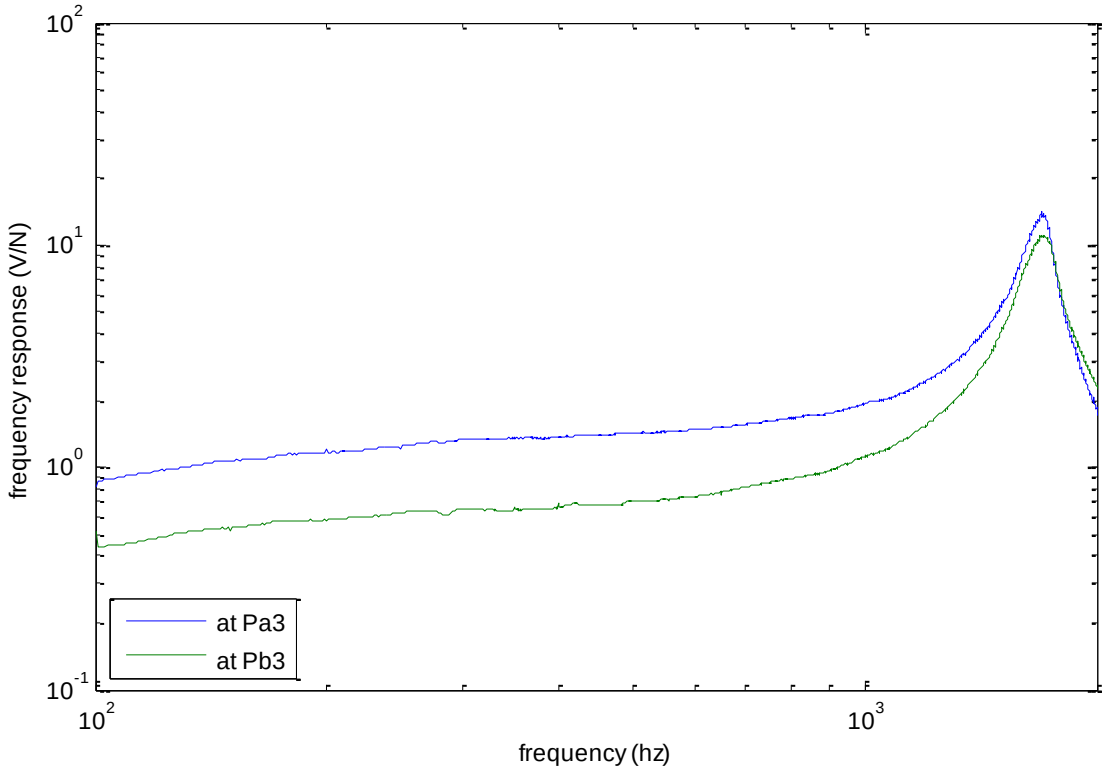

Figure 36: Comparison of the frequency response function measured in $Volts/Newton$ *for* $50mm$ *clamp and* $2mm$ *thickness plate at points Pa3, and Pb3*

3.6 Summary

In this chapter, the frequency response function in $Volts/Newtons$ of the transducer- plate arrangement was measured and we looked to understand how this is affected by - the sensor characteristics, the thickness of the plate, the size of the plate clamp, and across its surface. The magnitude of the frequency response function increases as the thickness of the plate decreases as the thinner plates displace more in comparison to a thicker plate. It was also found the magnitude of the frequency response function reduced as function of distance away from the transducer at the centre of the circular plate.

In applications such as measuring and characterising rain, the device is required to be small in size so as to not be affected by the varying noise levels and to be large enough to for a representative sample of falling raindrops. Another issue of significance is to reduce the probability of more than two droplets hitting the sensing area simultaneously (Jayawardena & Rezaur, 2000). These factors are also significant in selecting the dimensions of the device. It is for this reason the $2mm$ thickness plate, clamped with a $50mm$ ring is selected. The selected frequency range for comparison is between $100hz$ and $2000hz$. In this frequency range h both the low frequency (environmental and electrical) noise and high frequency (effects of road traffic) can be ignored. The first modal peak at $1700hz$ is of particular interest as it amplifies the impact of the drop.

In the next chapter, we'll look at the process for designing a rain generator. The rain generator is designed to consistently dispense water droplets of a set size at set intervals from a predetermined height at a constant drop velocity.

4 Design of rain generator

4.1 Introduction

In the previous chapter, we looked at the first set of experiments for designing the sensor device. This involved understanding the characteristics of the plate and how its physical properties (thickness, diameter) and the location of the impact affects frequency response function of the transducer-plate arrangement.

In this chapter, we will go through the process of designing a rain generator. The identified method of sensing for the device is to correlate the force of impact by the water droplet to its size. It is for this purpose we require the designed rain generator to consistently dispense water droplets at set size at set intervals from a predetermined height. The rain generator will be used later to further validate the force model described by Petersson (1995) discussed as part of the literature review. The methodology for this experiment is based on previous designs to understand the mechanics of soil detachment by raindrop impact (Guigon, Chaillout, Jager, & Despesse, 2008a; Jayawardena & Rezaur, 2000; Salmi et al., 2005). The chapter is broadly divided into three subsections, experimental setup, experimental discussion and summary.

4.2 Experimental setup

This sub section discusses the experimental setup for a rain generator. The experiment is designed to dispense different water drop sizes at a pre-set height and capture the output of the sensor for comparison and analysis. The test rig is made of an aluminium extrusion frame of height $2m$. A schematic representation of the experimental setup is as shown in Figure 37.The selection of the height was to enable the falling droplets to reach their terminal velocity in stagnant air.

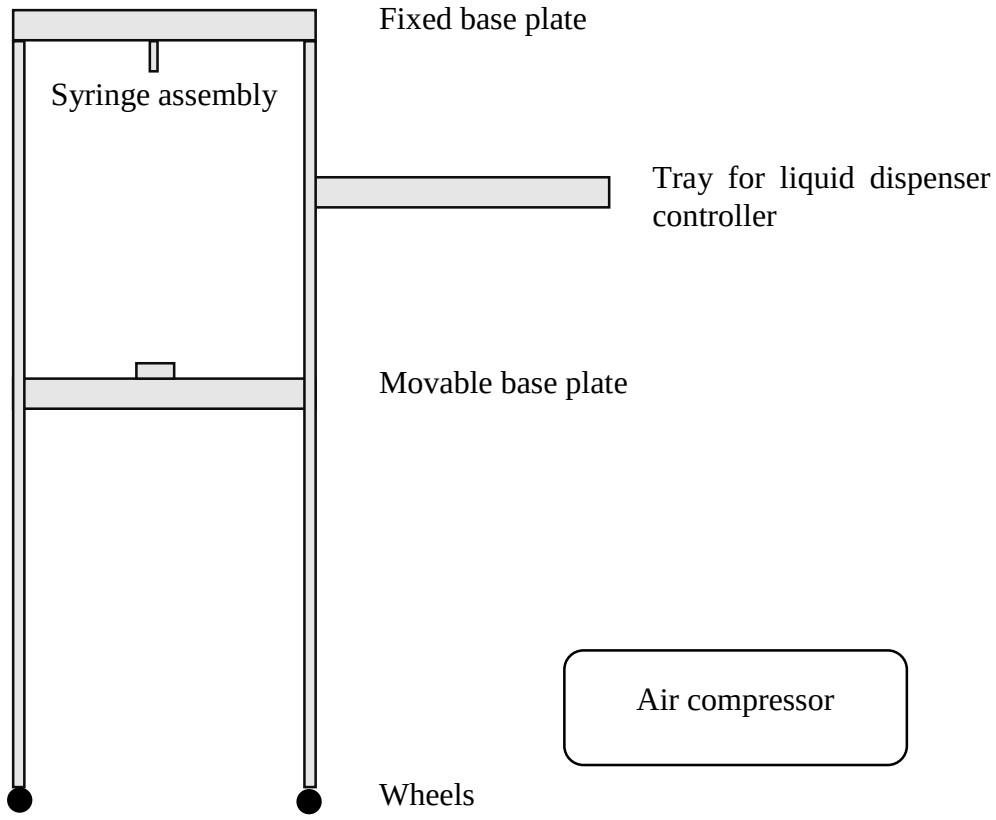

Figure 37: Schematic representation of the drop simulation apparatus

The test rig has two base plates attached, one at the upper and another at the lower end (Figure 38(c). At the top end, it has a syringe securely fastened, storing the water to be dispensed through interchangeable syringe needles at the geometric centre of the plate as shown in Figure 38(a) and at the lower base plate it has space for holding materials or plates as shown in Figure 38(b).

(a)

(b)

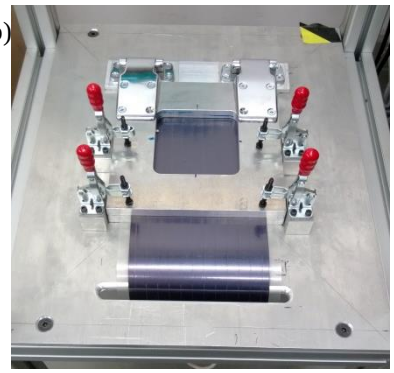

(c)

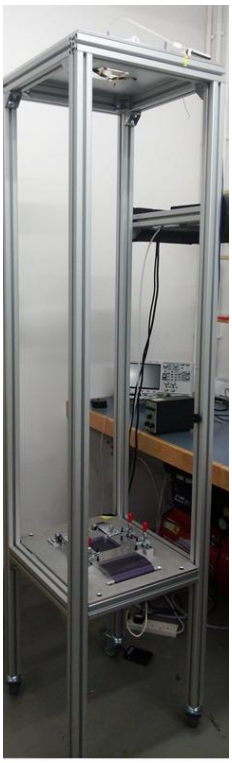

Figure 38: Test bench with (a) showing the syringe securely fastened to the top plate (b) showing the base plate with the test material clamped in the frame and (c) the complete structure of the test bench

The selected syringe needles had inner diameters of $0.15mm$, $0.58mm$ and $1.2mm$. The base plate which houses the sensor can be moved either higher or lower through the length of the extrusion housing to adjust the fall height for the droplet of water. By adjusting the fall height, we can all adjust the impact velocity of the water droplet.

4.3 Experimental discussion

The two main requirements to be met for this experiment is the drop size chosen must be within the expected drop size distribution of natural rainfall, and the drop impact velocity should approximate drops falling at their terminal velocity ensuring the same energy and momentum as that of natural rain.

4.3.1 Drop sizes

The volume of water droplet coming out of the syringe is controlled using an air pressure controlled liquid dispenser that is controlled using LabVIEW. The liquid dispenser used is called FIS $JB1113N$ automatic liquid dispenser. It takes in air input at $70 - 100\,psi$ ($5 - 7bar$) and has controllable air output from $1 - 100psi$ ($0.1 - 7\ bar$). The time for growth of the drop can be selected from 0.005 to $31secs$. For this experiment the output air pressure was set at 10psi with the pulse time set to $0.005secs$. This allows for the dispenser control to grow the water droplet based on the number of the pulses. The dispensing kit comes with a variety of syringe barrels and auxiliary attachments, of which the needle chosen for the experiment has an inner diameter of $0.15mm$. The drop grows along the section $A - A'$ at the end of the needle as shown in the Figure 39. The rupture of the drop is caused as the force exerted by the weight of the water droplet exceeds the adhesive forces due to the surface tension between the water droplet and A-A' causing the water droplet to separate and fall.

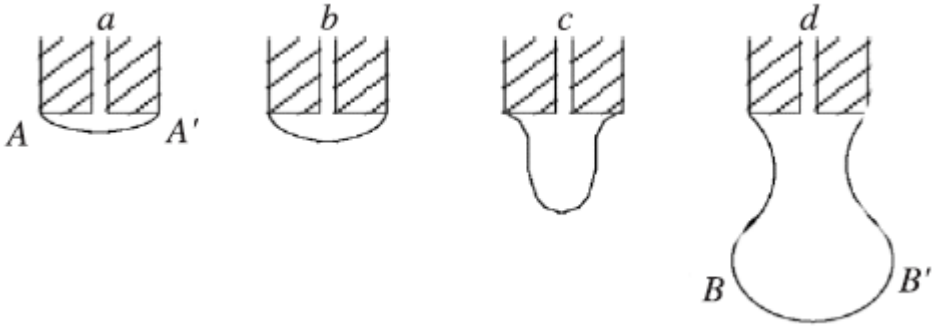

Figure 39: Drop falling from the syringe needle taken from (Guigon et al., 2008a)

The different drops generated from the identified needles require to be calibrated. There are different methods available for calibrating the size of water droplets. One such method is the use of laser optical measurements of the droplet diameters. Alternative methods of

measurement include the flour method (Laws & Parsons, 1943), oil immersion technique (Eigel & Moore, 1983), and stain method (Solomon, Kincaid, & Bezdek, 1985). In the flour method, the water droplets when they fall on a pan containing fresh, bleached wheat flour form little dough balls the size of the impacting droplet.

The identified method for evaluating the size of droplets in this experiment is the different density liquid method. In this method, the water droplets were collected in a deep container filled with oil. The droplets maintain their respective sizes on impact with the oil filled container. Thirty drops were created through the process highlighted earlier for a particular needle with inner diameter as mentioned in Table 8.

The container of oil with the water droplets were then photographed. The image generated was then analysed in Matlab using the image processing toolbox to measure the size of the water droplets. The results of those measurements are highlighted in the table below.

Syringe needle description	Needle inner diameter (in mm)	Mean diameter of drop (in mm)	Range of measurement (in mm)
Lavender	0.15	2.23	$\pm$0.02
Clear	0.20	2.48	$\pm$0.02
Red	0.25	2.65	$\pm$0.02
Orange	0.33	2.86	$\pm$0.02
Purple	0.51	3.06	$\pm$0.02
Pink	0.58	3.29	$\pm$0.02
Black	1.20	3.89	$\pm$0.02

Table 8: Comparison of the diameter of the drops obtained against the inner diameter of the syringe needle used

The images collected are processed and analysed to obtain the sizes of the water droplets. A summary of the steps taken for analysing the image is given in Figure 40. The major steps involve noise reduction, feature extraction, and blob detection. The identification of the drops is affected by the amount of contrast between the foreground (drops) and the background (container with oil). An example image of the drops measured in pixels are shown in Figure 41.

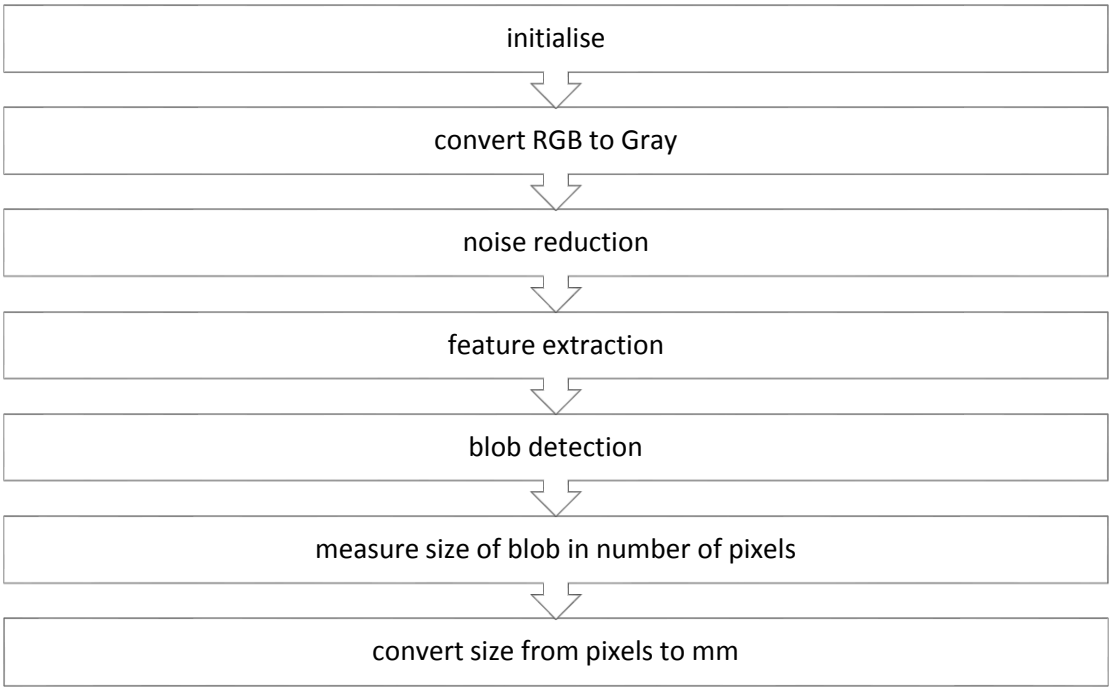

Figure 40: Summary of the steps taken for identifying the drop sizes from the sample images taken

Figure 41: A sample image of the water droplets collected in a tub, identified and measured in number of pixels

4.3.2 Fall velocity of droplets

As mentioned as part of the literature review, the impact velocity of raindrops is assumed to be at their terminal velocity. Several studies have been highlighted in the literature review on the relationship of drop's terminal velocity as a function of its diameter. However, these relations don't hold true during windy conditions as the velocity of the raindrops will be higher with them hitting the surface at an angle.

A more practical approach to check if the water droplet has attained its expected drop velocity would be the use of laser detectors, one at the top end of the source of the drop creation and the other near to the impact point. By measuring the time taken by the water droplet to cross both laser detector, we will be able to measure the velocity of fall for the droplet. However, this experiment is conducted indoors and it is safe to assume the droplets will reach their terminal velocity in stagnant air given enough height of fall.

Due to the limitations of the rain simulator, we will estimate the velocity of the drop using a numerical model proposed by Van Boxel (1998) relating to the distance travelled. There are two principle forces at work on a falling body – force of gravity (F_g) and friction or drag force (F_d). Assuming the mass of the drop m is constant and the initial velocity is $0.0 m/s$. The acceleration of the drop can be calculated from the forces applied to it.

$$\frac{dV}{dt} = \frac{1}{m}\left(F_g - F_d(V)\right) \qquad 4.1$$

The model uses Euler's method to calculate the drop velocity as a function of time and distance travelled with the velocity converging towards terminal velocity(Valette et al., 2012). Figure 42 shows the results of the implementation of the calculation for drop sizes $2.23mm$, $3.29mm$ and $3.89mm$. The chosen height for the falling drops is set to 0.6 metres, and using the methods of calculation the velocity of the drop can be estimated to be $3.2 m/s$.

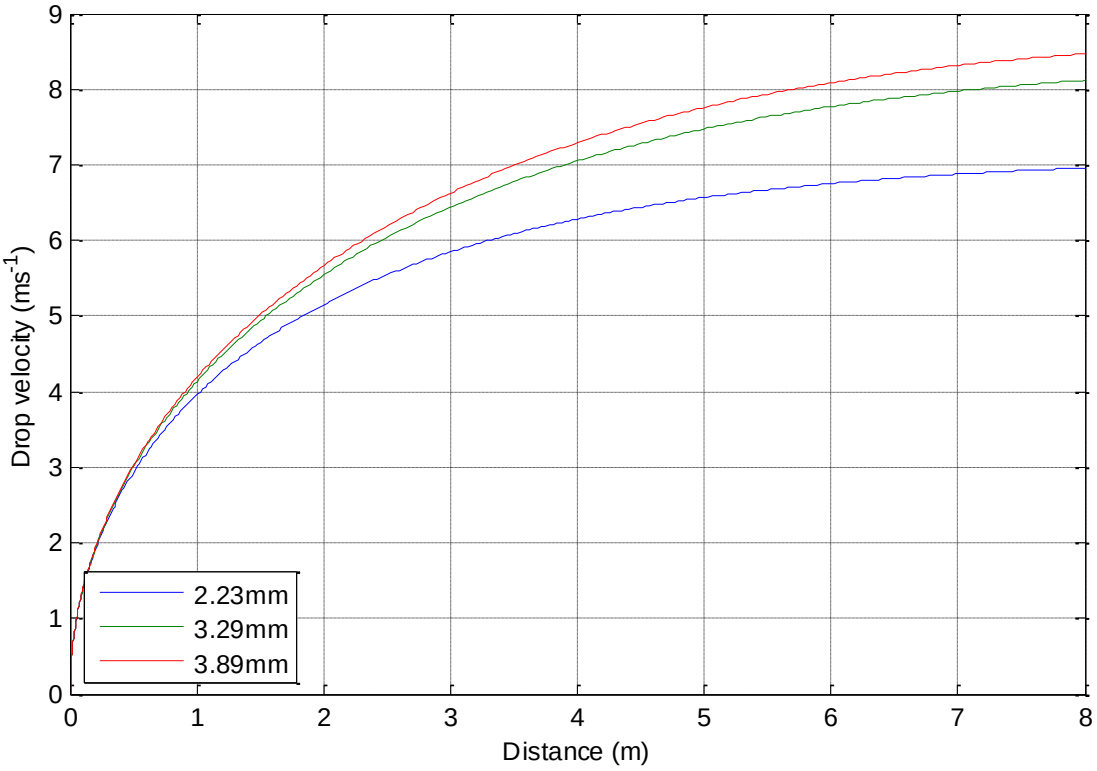

Figure 42: Drop velocity vs distance travelled for a sample of the drop sizes.

4.4 Summary

In this chapter we looked to design and build a rain drop generator. The designed simulator will help further the validation of the force of a water droplet model designed by Petersson, which will be discussed in detail in the following chapters. This experiment is broadly based on previous experiments used to understand the mechanics of soil erosion. There are two main requirements for this experiment - the drops generated by the technique must be of the same size, and must fall at the same velocity. The drop size can be controlled by varying the diameter of the needle (with the rate of growth constant) and the drop velocity is controlled by varying the height of fall for droplet. The fall distance for the drop was limited to $0.6m$ and for that limited the drop velocity to $3.2m/s$ for the three different drop sizes used for the experiment.

In the next chapter, we are going to use the rain drop generator to dispense individual droplets of set diameter, measure their impact force and compare the results of the measurement to Petersson (1995) force model.

5 Force of a drop

5.1 Introduction

In the previous chapter, the design process for building a rain drop generator was discussed. It will generate drops of a particular diameter and a particular fall velocity. This is controlled by varying the size of the inner diameter of the syringe needles or the height of fall of the drop respectively.

In this chapter, we will measure the impact force of the individual droplets generated using the rain generator, and compare this measurement to Petersson (1995) force model. The results of this experiment will help with simulating the response of the transducer- plate arrangement in order to understand its response, and potential problems with the device.

5.2 Experimental setup

The experimental setup for this experiment is essentially a combination of chapter 3, and chapter 4. The process for simulating the drops is discussed as part of chapter 4. The characteristics (drop diameter and fall velocity) of the drops are simulated by the use of interchangeable syringe needles and changing the height of fall for the droplet. The sensor used for measuring the impact force of a drop of water is a force transducer type 8203 by Bruel & Kjaer, it is calibrated at $3.35 pC/N$ and is attached with a $10mm$ diameter and $5mm$ thickness copper disc. The disc is attached to increase measurable, target surface area of the sensor.

Three drop sizes were identified for this experiment- $2.23mm$, $3.29mm$ and $3.89mm$. These drop sizes were simulated using the lavender, pink, and black coloured needles. The inner diameter of the needles were $0.15mm$, $0.58mm$ and $1.20mm$ respectively. For this experiment, the height of fall was set to 0.6 metres. At this height, the calculated velocity for the three chosen drop sizes were constant at $3.2\, m/s$. This velocity is calculated via equation 4.1 using Euler's method to calculate the drop velocity as a function of time and distance. The method was discussed as part of chapter 4. Five trials each of the simulated drops were conducted.

5.3 Force of a drop impacting a rigid system

As part of the literature review in chapter 2, we looked at the details for deriving the force of a single drop impacting a rigid system as suggested by Petersson (1995). Equation 5.1 highlights this relation as a function of time

$$F(t) = -\rho\pi r^2 \begin{cases} -v_0^2, \ t \leq \frac{2r}{3v_0} \\ v_0^2 \left[\frac{5}{9} + \frac{4v_0 t}{3r} - \frac{v_0^2 t^2}{r^2}\right], \ \frac{2r}{3v_0} \leq t \leq \frac{5r}{3v_0} \end{cases} \quad 5.1$$

From the equation, we can see the impact force of the drop is dependent on the spherical equivalent radius of the droplet, and its fall velocity. Using this equation we are able to simulate the transient behaviour of the force of a drop in the time domain. Figure 43 shows a comparison of the frequency domain representation of the simulated force for the three drop sizes identified at their expected fall velocities.

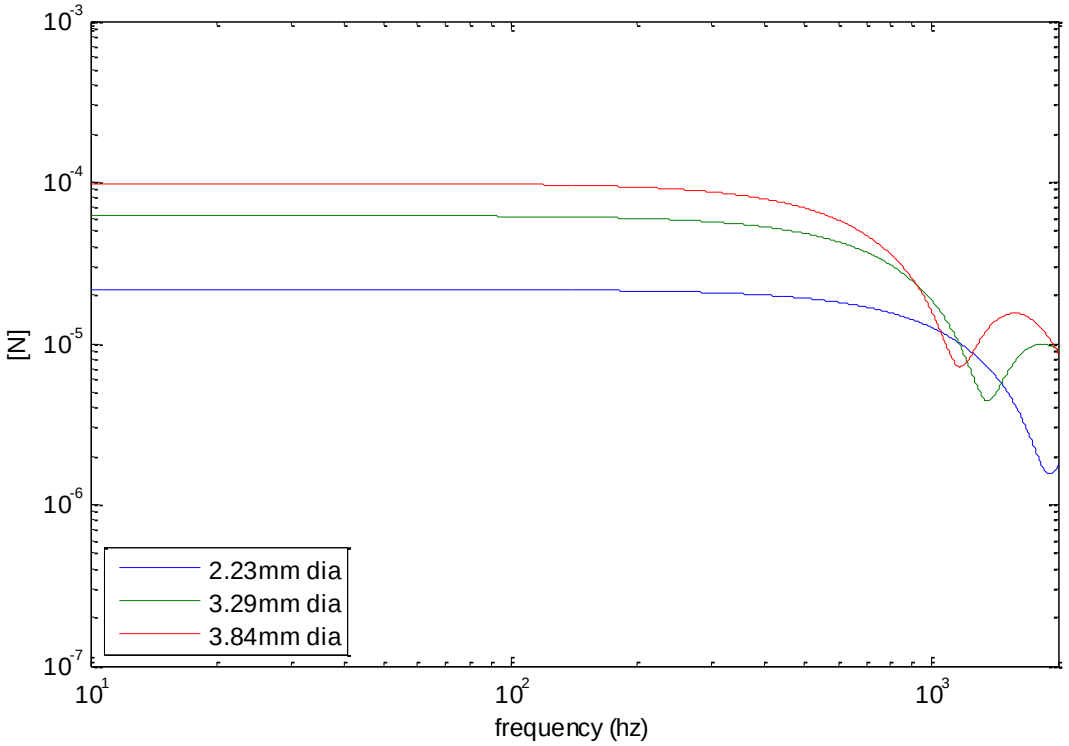

Figure 43: Comparison of the frequency domain representation of simulated force for the drops of diameter 2.23mm, 3.29mm and 3.84mm

5.4 Measured force of a drop impacting a rigid system

The multi- channel analyser was used here in its single channel mode to measure force directly. The analyser had similar settings to the measurements made as part of chapter 3 where it was set to acquire $1sec$ of data sampled at $16khz$. Following the measurements, an average of the trials (measured frequency domain representation) for each drop size was calculated. A five point moving average was applied on the calculated results to find the equivalent force of the drop in the frequency domain. A comparison of the end results is shown in Figure 44.

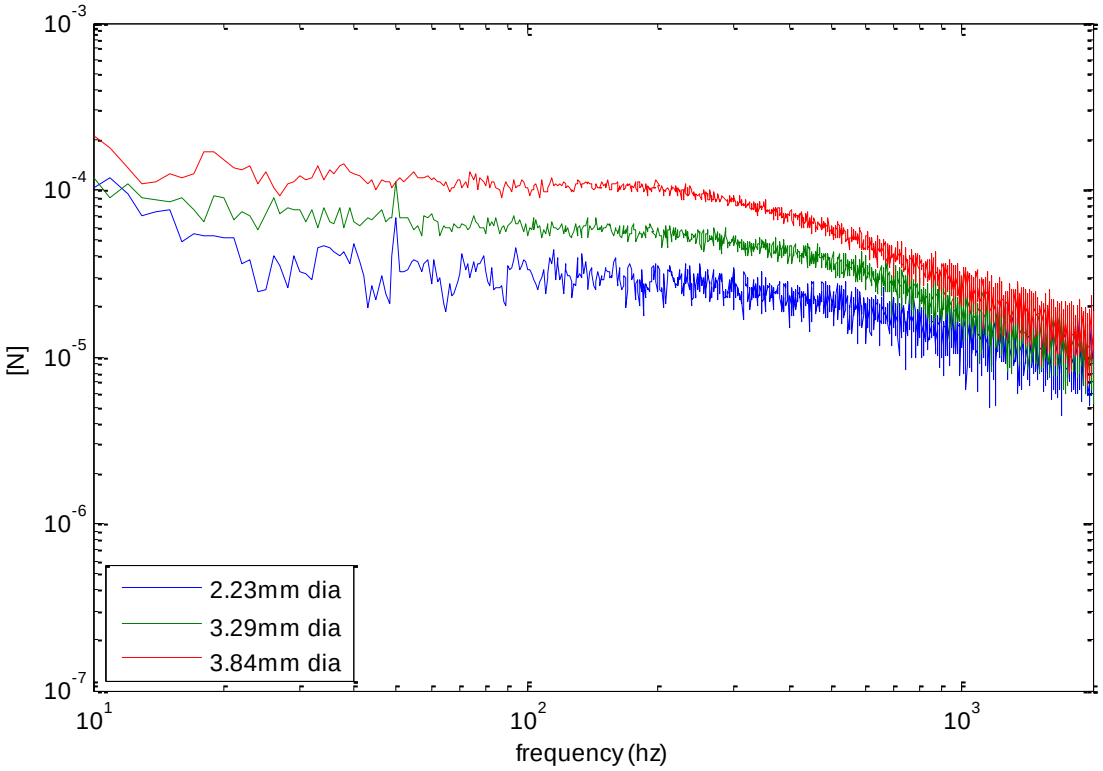

Figure 44: A comparison of the results force measurements made in frequency domain for the three different drops of sizes 2.23mm, 3.29mm, and 3.84mm diamter

The comparison of the results for the measured drop force with the simulated drop force in the frequency domain representation for the three drop sizes are as shown in the figures Figure 45, Figure 46 and Figure 47. The figures show there is a good correlation between the measured forces of the drop and the simulated force for the larger drops as the signal to noise ratio of the measurement is better in the frequency range of $100hz$ and $1000hz$. The high values below 20Hz can be attributed to the noise floor of the force sensor. This particularly works for the device design as the selected frequency range of operation for the 50mm clamp- transducer plate arrangement is between $100hz$ and $2000hz$.

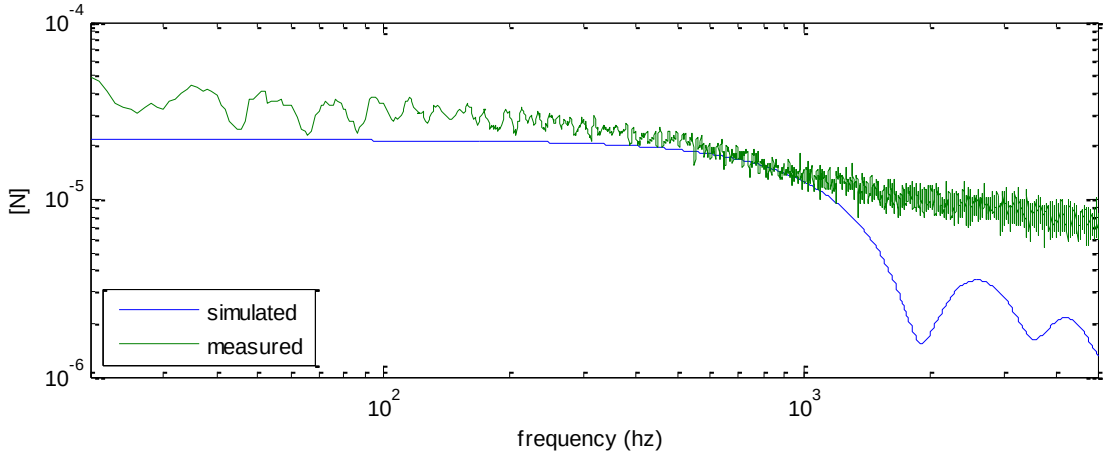

Figure 45: Comparison of the measured force vs simulated force of a drop of diameter $2.23mm$ *and drop velocity* $3.2m/s$

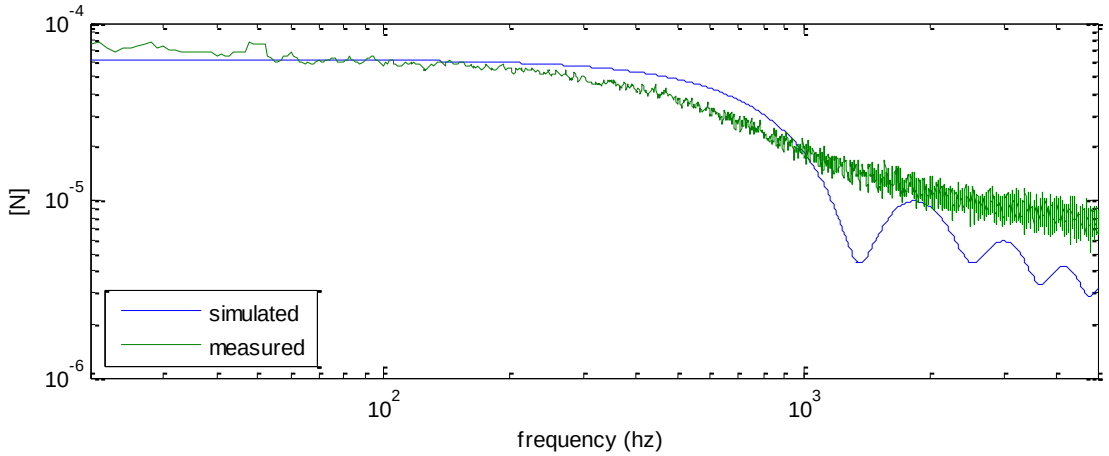

Figure 46: Comparison of the measured force vs simulated force of a drop of diameter $3.29mm$ *and drop velocity* $3.2m/s$

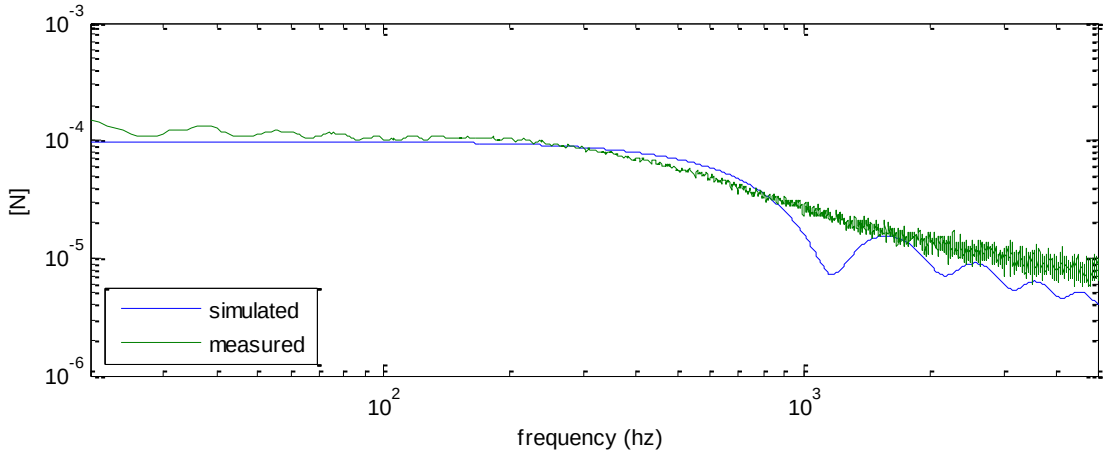

Figure 47: Comparison of the measured force vs simulated force of a drop of diameter $3.84mm$ *and drop velocity* $3.2m/s$

5.5 Force of a drop impacting a non-rigid system

For a non- rigid receiving system, Petersson (1995) by allowing for the motion of the plate and assuming the shape of the drop as a short cylinder, the force of the drop is simplified to

$$F_D \approx \rho S_D v_D^2 \left[1 - \frac{1}{2+\frac{C_R}{\rho S_D v_D}}\right]^2 \qquad 5.2$$

By comparing the flow impedance of the drop $Z_{flow} = \rho S_D v_D$ with the mechanical point impedance for a pure, resistive receiving structure, it is evident the drop appears more rigid for a higher drop velocity. In order to assume the drop force to be an ideal source of constant force, the Z_{flow} (drop impedance) must be much smaller than C_R (mechanical point impedance of the receiving structure) (Petersson, 1995). Figure 48 shows the comparison of the drop impedance for a drop of diameter $0.2998\ mm$, and drop velocity $0.3843\ m/s$ (calculated using terminal velocity equation given by Valette et al. (2012)) and the plate impedance for a 50mm clamp plate arrangement. This shows that the plate impedance is more than that of drop impedance for all frequencies, allowing for us to assume the device designed as a rigid body.

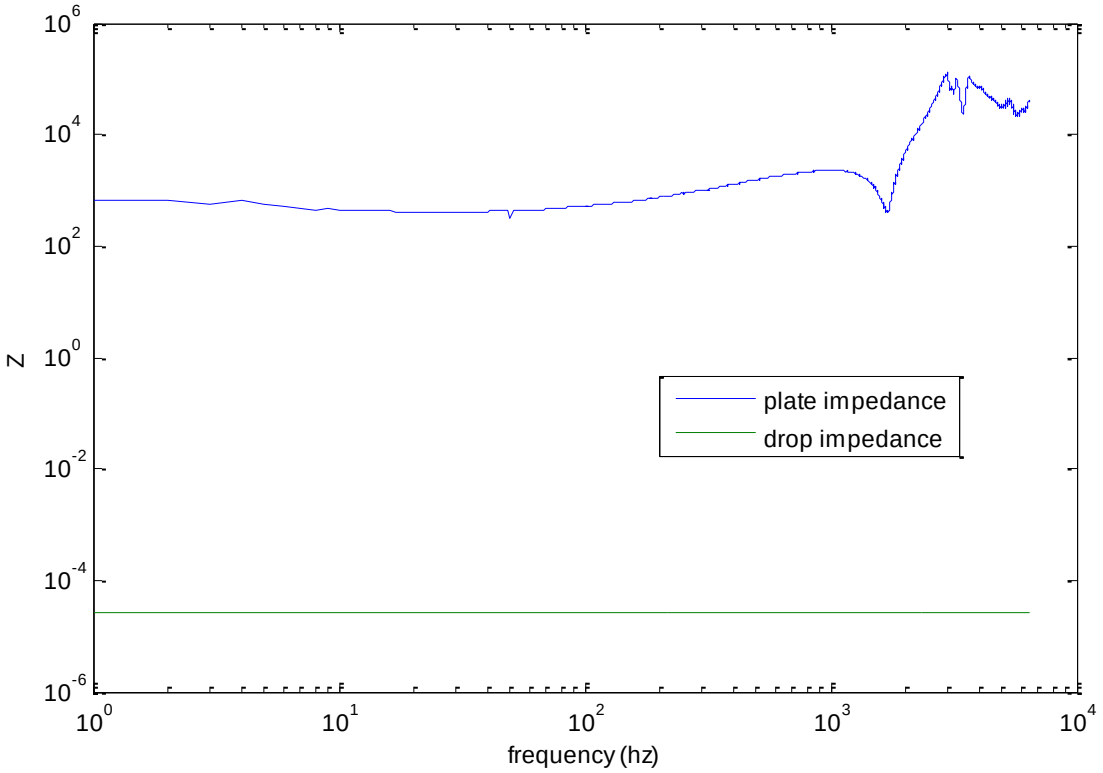

Figure 48: Comparison of the impedance of the transducer plate of $2mm$ *thickness with a* $50mm$ *clamp ring configuration with the drop impedance of drop size* $0.2998mm$ *and drop velocity* $0.3834m/s$

5.6 Summary

In this chapter we looked to measure the force of water droplet and compare it with the simulated force for the same drop size and drop velocity impacting a rigid body. It was found there is a good correlation between the measured force and the simulated force. In the case of a non-rigid receiver system, the system behaves as rigid receiver system, providing the flow impedance of the drop is much smaller than the mechanical point impedance of the receiving structure. This is particularly useful, since the device is a 2mm thick plate and can be characterised as non- rigid. As the impedance of the smallest drop measurable 0.2998mm is a lot smaller than the impedance of the sensing surface allowing for the device to be treated as a rigid system.

6 Response of the plate to background noise

6.1 Introduction

In the previous chapter, we compared the force of a water droplet with the simulated force of the same drop size and drop velocity impacting a rigid body. There was a good correlation between the simulated and the measured force. In this chapter, we look to understand the effects on environmental noise and vibration on the device. This will help with the calibration of the device. The chapter is divided to three main sub-sections- background, experimental setup, experimental discussions, and conclusions.

The background noise and vibration is a concern for the proper functioning of the device because this will affect the lower size of rain droplets the device will be able to measure. Ambient noise is always present. The sources of background noise can be natural (animals, wind) or man-made activities (such as vehicular, factories, aeroplane, construction work) (Becker & Güdesen, 2000). A selection of typical ambient noise condition are represented in Figure 49.

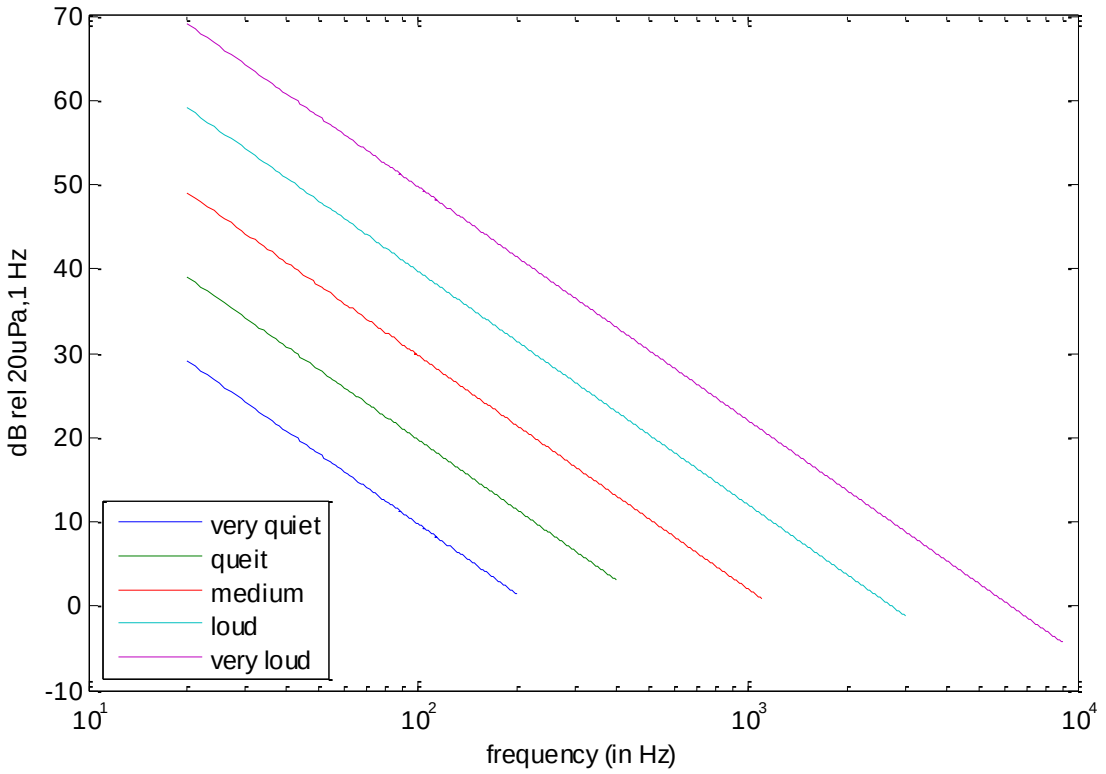

Figure 49: Typical ambient noise conditions adapted from Becker and Güdesen (2000)

6.2 Discussion of experimental results

6.2.1 Setup

An experiment to measure the impact of the sound pressure on the transducer plate arrangement was conducted in the small reverberant room at the University of Salford. The room is designed to be very reverberant. The walls of the room are made of painted dense bricks. The room is made to diffuse sound by the use of reinforced concrete sloping roof and a non- parallel walls. The reinforced concrete floor is built on a Rockwool insulation board to provide vibration isolation.

The selected transducer (thin film piezo sensor) is of the same dimension as of previous experiments ($FDT1\text{-}052K$ by measurement specialities). The multi- channel analyser is used to generate the noise and the frequency response function of the transducer plate arrangement is measured in $Volts/Pascal$. The experiment is repeated for the three plates (thickness $2mm$, $3mm$ and $4mm$) in the two configurations (clamp diameter $5cm$ and $10cm$).

6.2.2 Frequency response function

The frequency response function measured in $Volts/Pascal$ of the transducer-plate arrangement is as shown in Figure 50. However, as can be seen the measurement made the results are quite wavy making it hard to discern and compare between the different plate thicknesses. Following which the response of the plate was measured in $1/3^{rd}$ octave band. Figure 51 shows the results for $100mm$ clamp comparison in $1/3^{rd}$ octave band. The results of the measurement made (Figure 52) for $50mm$ diameter plate size is of more interest this is because as concluded in Chapter 3, the size of the device needs to be large enough to be representative sample of falling raindrops and small enough so that the varying noise levels does not affect the performance of the device.

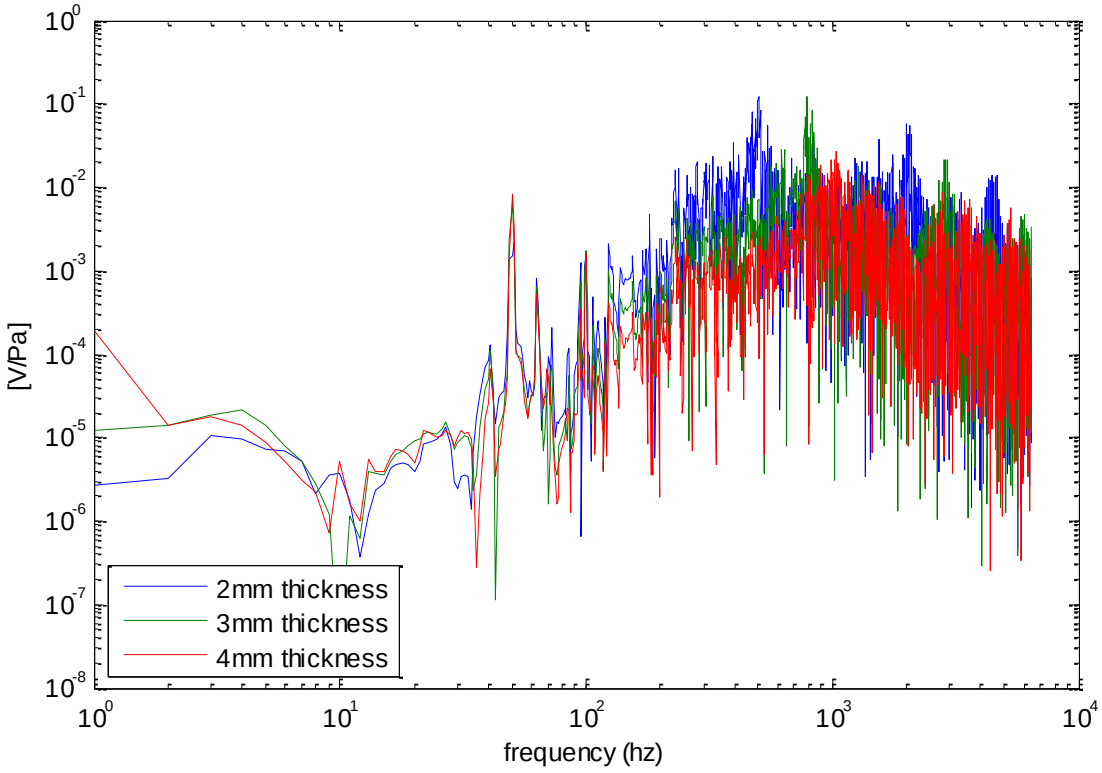

Figure 50: Comparison of the frequency response function of the transducer- plate measurement for 100*mm clamp arrangement in narrow frequency band*

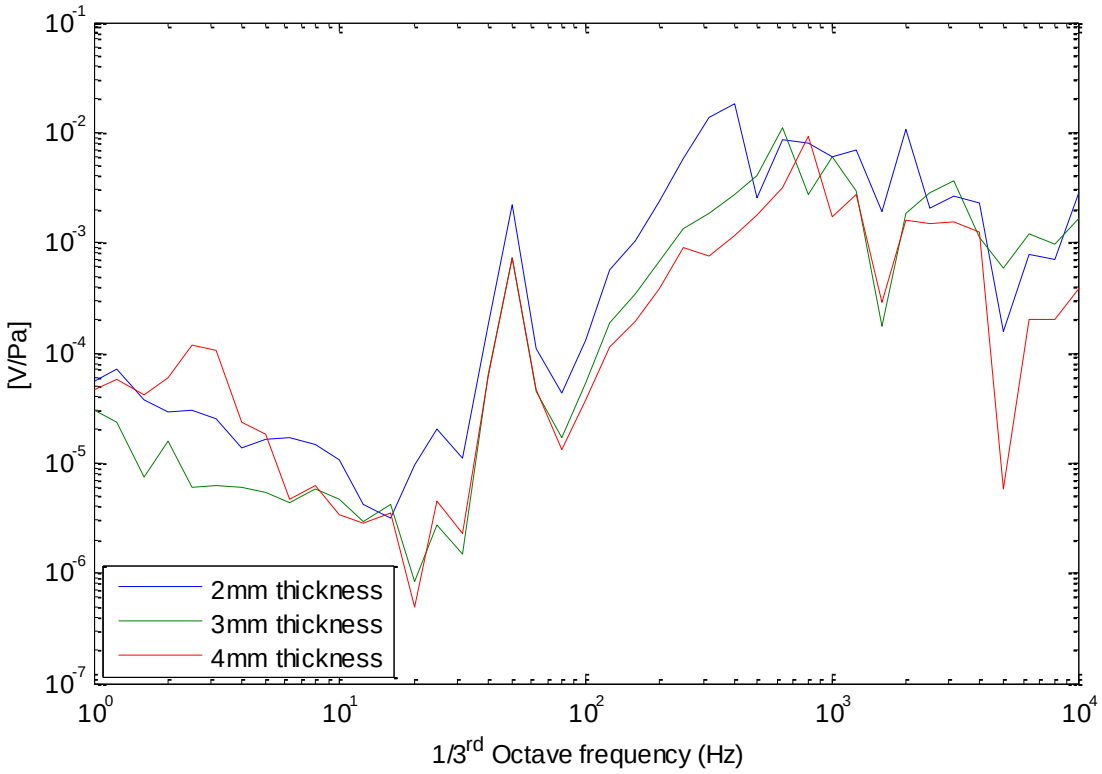

Figure 51: Comparison of the frequency response function for the transducer- plate measurement for 100*mm clamp arrangement in 1/3rd octave frequency band*

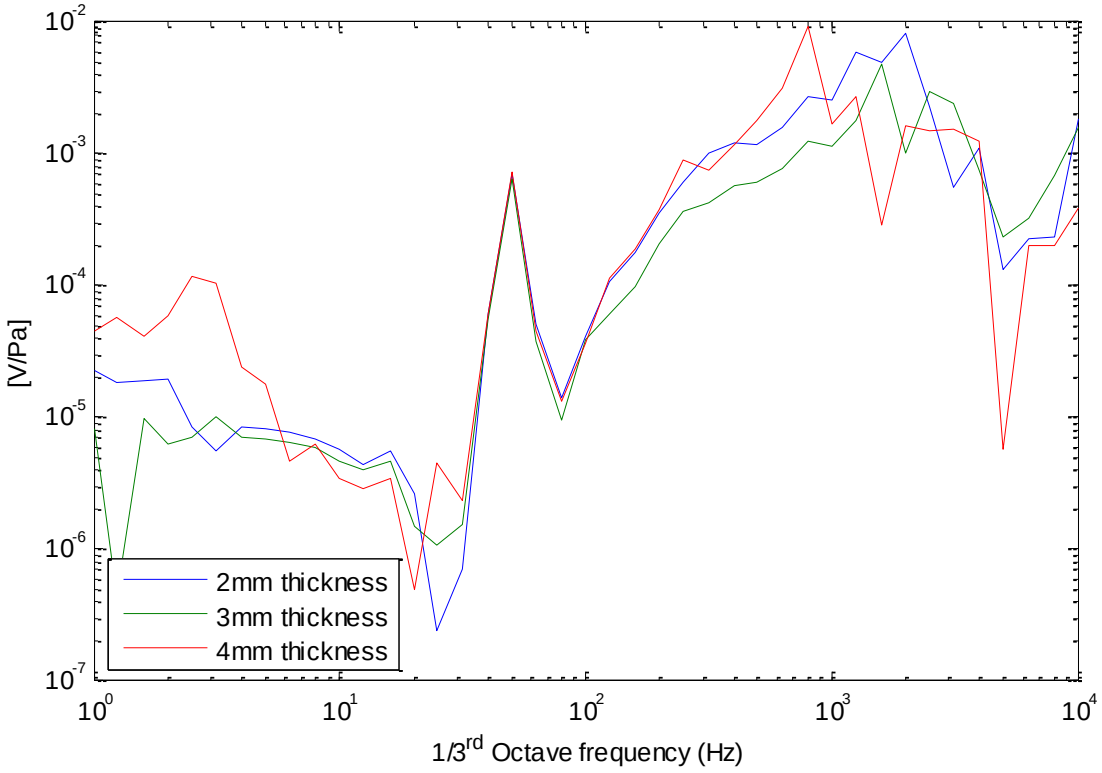

Figure 52: Comparison of the frequency response function for the transducer- plate measurement for $50mm$ *clamp arrangement in 1/3rd octave frequency band*

6.2.3 Comparison with the drop

By comparing the output response of the transducer-plate arrangement due to an impact of a rain droplet striking it to the output response of the plate due to sound pressure acting upon the device, we can calculate the minimum drop size that can be measured by the device. This will help with understanding the limits of the device. The output response due to a raindrop is calculated by multiplying the force function in the frequency domain with the frequency response function of the transducer plate arrangement measured as part of chapter 3. Becker and Güdesen (2000) recommends classifying ambient noise as shown in Figure 49 to very quiet, quiet, medium, loud, and very loud. Noise levels are subjective and perception of this classification differs, as to some the $50dB$ line is quiet scenario in the environment. However, as this is a device used to measure rain it can be classified as loud. The functions from the graph (Figure 49) can be represented in a logarithmic form to as shown in Table 9. Here dB is the sound pressure in decibels and fr is the frequency with linear spacing.

Type	Expression
Very quiet	$dB = -12 * \log(fr) + 65$
Quiet	$dB = -12 * \log(fr) + 75$
Medium	$dB = -12 * \log(fr) + 85$
Loud	$dB = -12 * \log(fr) + 95$
Very Loud	$dB = -12 * \log(fr) + 105$

Table 9: Table showing the relation function for the different classifications of noise.

The dB value is converted to $Pascal$ for the calculation of the response of the plate to the different noises. This pressure for a linear spacing frequency is multiplied to the frequency response function in $Volts/Pascals$ for the selected device dimensions ($50mm$ diameter and $2mm$ thickness). The results represented in $1/3^{rd}$ octave band is as shown in Figure 53. The reason for selection of the $1/3^{rd}$ octave band is to clearly compare the results. The $50Hz$ noise in the output response of the plate will not scale with increasing sound pressure as is seen in the figure. This issue of scaling can be attributed to the error in the measured frequency response function. However, this noise will be filtered as part of the signal processing.

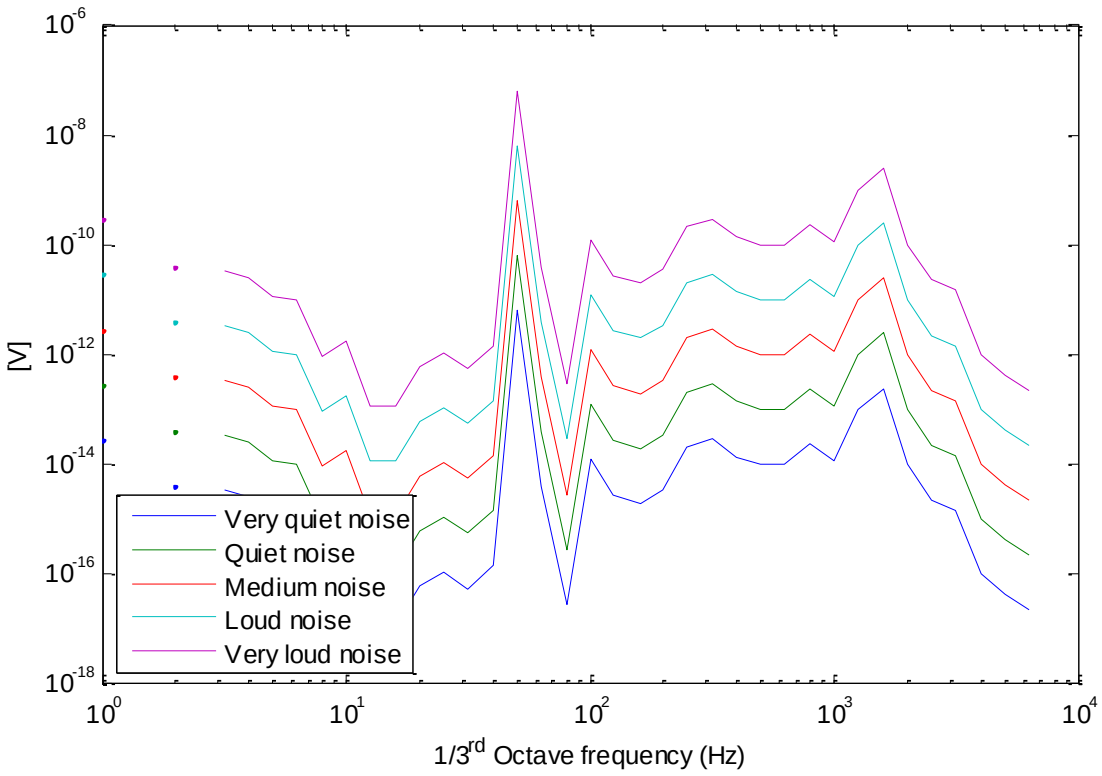

Figure 53: Multiplying the noise function from Becker and Güdesen (2000) with the frequency response function in $Volts/Pascal$ of the $50mm$ diameter clamp with plate of thickness $2mm$

The results of the output of the transducer- plate arrangement due to noise is compared to the resultant output for different sizes of water droplets to identify the lowest drop size measurable by the setup. The selected functions for comparison in the graph includes quiet noise, and loud noise. Figure 54 shows the comparison of the output of the device when a droplet sized $0.4mm$ diameter hits the surface in comparison to the two types of chosen noise profiles, it is the lowest sized drop that can be measured by the device. Figure 55 shows the comparison of the output of the device when a larger drop sized $3.2mm$ diameter hits the surface in comparison to the same chosen noise profiles.

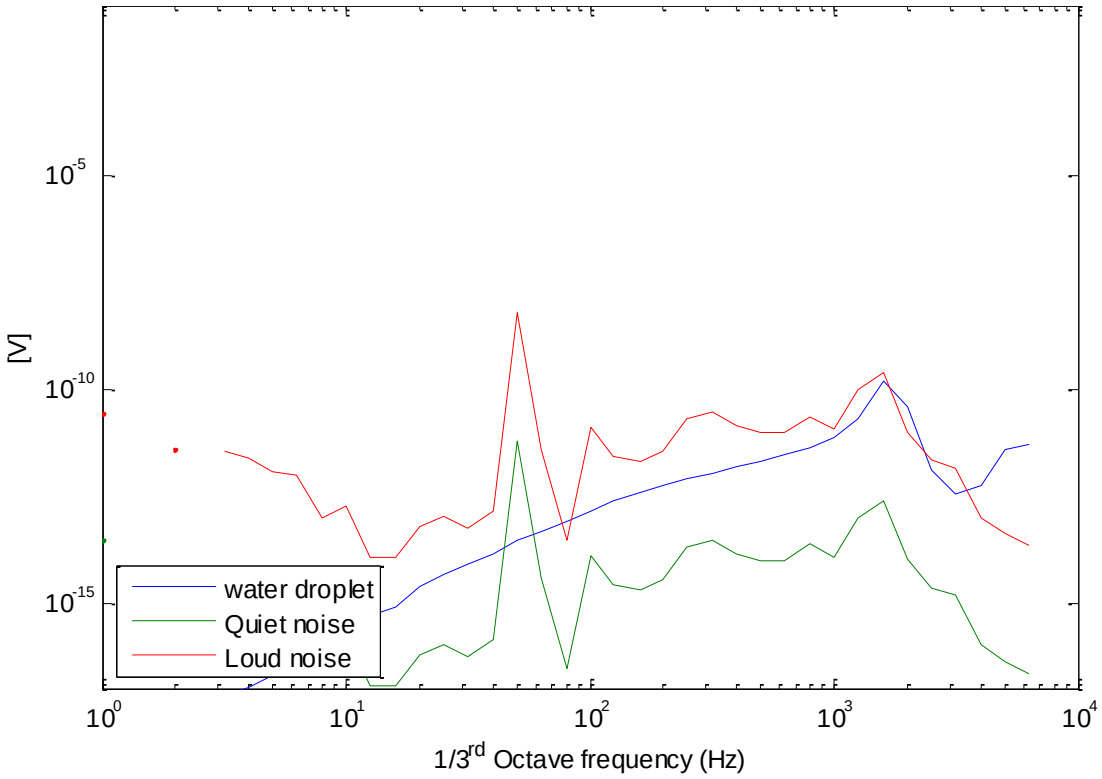

Figure 54: Comparison of the output response between the $0.4mm$ *diameter droplet against quiet noise and loud noise profile for a plate of thickness* $2mm$ *with a clamp of* $50mm$

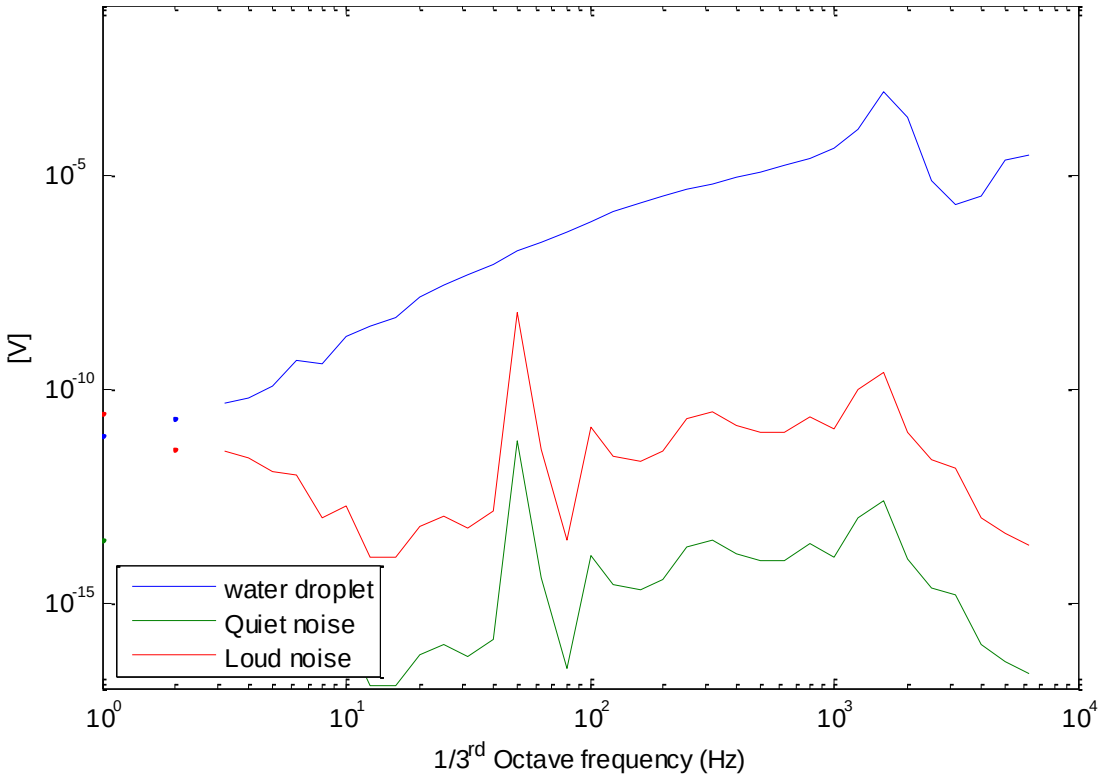

Figure 55: Comparison of the output response between the $3.2mm$ *diameter droplet against quiet noise and loud noise profile for a plate of thickness* $2mm$ *with a clamp of* $50mm$

6.3 Summary

In this chapter, the simulated output response of the transducer- plate arrangement (for the different configurations) for an impacted drop is compared to the simulated output response for different levels of environmental noise and vibrations. This experiment helps with determining the lowest drop size measurable by the device arrangement. The output response of the transducer- plate arrangement is calculated by multiplying the frequency response function of the transducer plate with the simulated noise function for the different levels. This output response of the plate due to sound and vibration is compared to the output response of the plate due to the rain drop. The minimum measurable drop was found to be of equivalent size $0.4mm$ diameter. This drop size is close to the peak of the probability distribution curve for rain drop size and affect the types of rain depending upon the intensity, the device designed will be able to measure. This will be further discussed in the following chapter.

In the following chapter, we will look into the simulation of the device behaviour for simulated rain in order to develop an algorithm for the rain analysis. We will also look at methods for calibrating the transducer- plate arrangement.

7 Device simulation

7.1 Introduction

In the previous chapter, we compared the simulated output response of the transducer- plate arrangement for an impacted drop to the simulated output response for different levels of environmental noise and vibrations. The experiment helped us to determine the lowest measurable size of rain droplets ($0.4mm$ diameter) by the arrangement.

There are different methods for calibrating disdrometers, in this thesis we are looking to utilise a simple calibration techniques wherein single drops of known diameter and drop velocity are dropped on the device from the top of the simulation tower. However, conventional calibration technique is a tedious process, alternative methods involve the use of adaptive signal processing technique. On such technique proposed by Kourtellis, Kasparis, Jones, and Lane (2005) wherein a tipping bucket gauge provides a reference signal for optimising the measurements of a disdrometer. However, in chapter 5, we have a good correlation between the simulated force of a water droplet and the measured force for a water droplet. This allows us to speed up the calibration process of the device.

7.2 Methodology for rain simulation

In this section, we are looking into the methodology for rain simulation. (Valette et al. (2012)) defines rainfall as a finite set of raindrops, characterized by its instant of impact, location, and volume. Natural rain is stochastic by nature, this allows for the number of drops for each size to be different if the duration and intensity is considered to be constant. There are several factors identified that affects the simulation of device response to rain are listed as follows and described in the following subsection:

- The time and space distribution of drops
- The size distribution of the drops
- The fall velocity of the drops

7.2.1 The time and location based distribution of the drops

In this subsection, we look to discuss the location of impact and time instant for the drop impact during a rain episode. Firstly, let's discuss the distribution of the droplets across time. A uniform distribution of the drops in assumed wherein each instant has the same probability assigned to

the drop. Secondly the impact location, here there are two approaches that may be taken. Valette et al. (2012) albeit has discussed the development of a rain simulator over a wide area, the assumptions made can be used for over the device. The paper suggests two methods for simulating the spatial distribution of rain, wherein we assume a uniform distribution or normal distribution with a configurable standard deviation. In this case, the results will correspond to a capillary based drop forming simulator. The second method suggested, is to recreate a realistic rain intensity map by the use of noise algorithm. Perlin's noise function (Perlin, 2002) is often used to synthesise natural textures for clouds, or smoke. The chosen method to mimic the stochastic behaviour of rain is a simplistic method. In this method we pick a random location (position on the plate corresponding to the frequency response function) and a time instant for each individual drop within a considered episode of rain.

In chapter 3, the frequency response function of the transducer plate arrangement was seen to be decreasing in amplitude as the impact point moved further away from the centre of the circular plate as shown in figures 1 & 2. However, for the purposes of this simulation, it is assumed the frequency response of the transducer plate arrangement is the same throughout. This will tie in with the primary method of simulating the rain intensity across a wider area. The impact of the varying frequency response function will be discussed as part of possible errors.

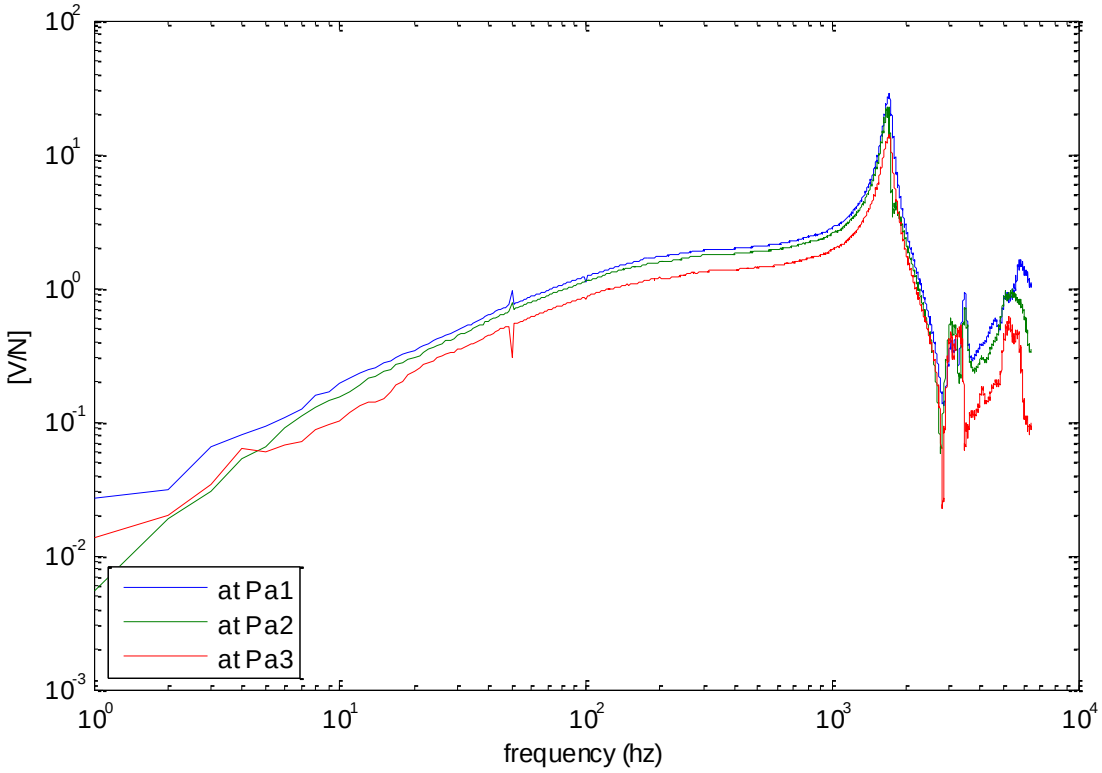

Figure 56: Comparison of the frequency response function measured in Volts/Newton for a plate of 2mm thickness and clamp size 50mm diameter at points Pa1, Pa2, and Pa3

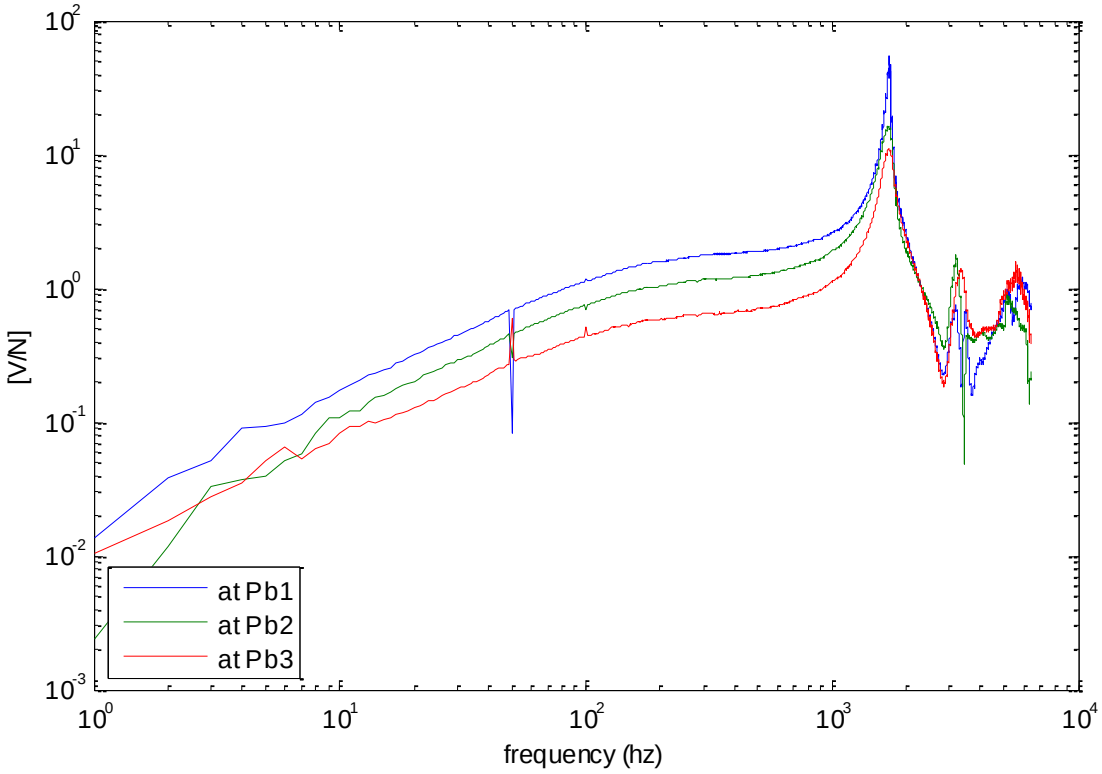

Figure 57: Comparison of the frequency response function measured in Volts/Newton for a plate of 2mm thickness and clamp size 50mm diameter at points Pb1, Pb2, and Pb3

7.2.2 The size distribution of the drops

The drop size distribution has been discussed as part of the literature review. It is defined as the probability distribution of the number of drops per unit size (expressed in diameter of the drop) and per unit volume of space as measured on the surface of earth. There are two methods to obtain the drop size distribution for simulating rain. The first method would be to utilize existing measured DSD data from other disdrometer. The second method is to reproduce the size distribution from a model. One such model is the Uijlenhoet and Stricker (Valette et al., 2012).

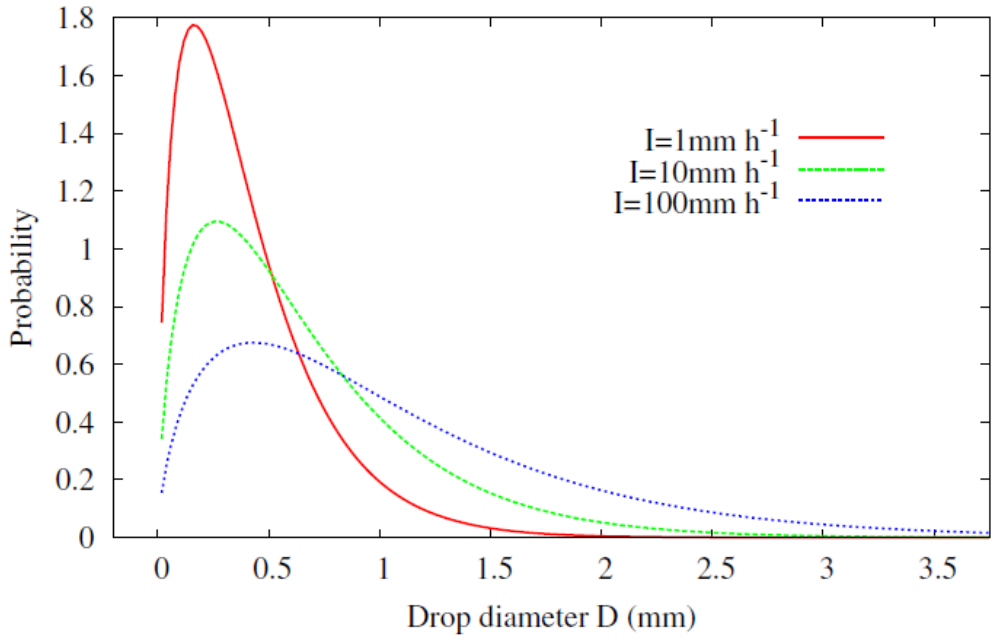

Figure 58: Probability density function of the size of raindrops for different rainfall intensities taken from Valette et al. (2012)

In this simulation we utilize the long term archive of disdrometer dataset collected at Chilbolton, UK by the British Atmospheric Data Centre (BADC) which is one of the centres and facilities in the National Environmental Research council (NERC). An example of the total drops collected for April 2004 is as shown in Figure 59.

In the chapter 6, by simulating the output response of the device for different drop sizes and comparing it with the output response of the device for different noise profiles, we find the lowest measurable drop size is of equivalent diameter of 0.4mm. This limits the ability of the device accurately measure rain of lower intensity, as is visible on Figure 58.

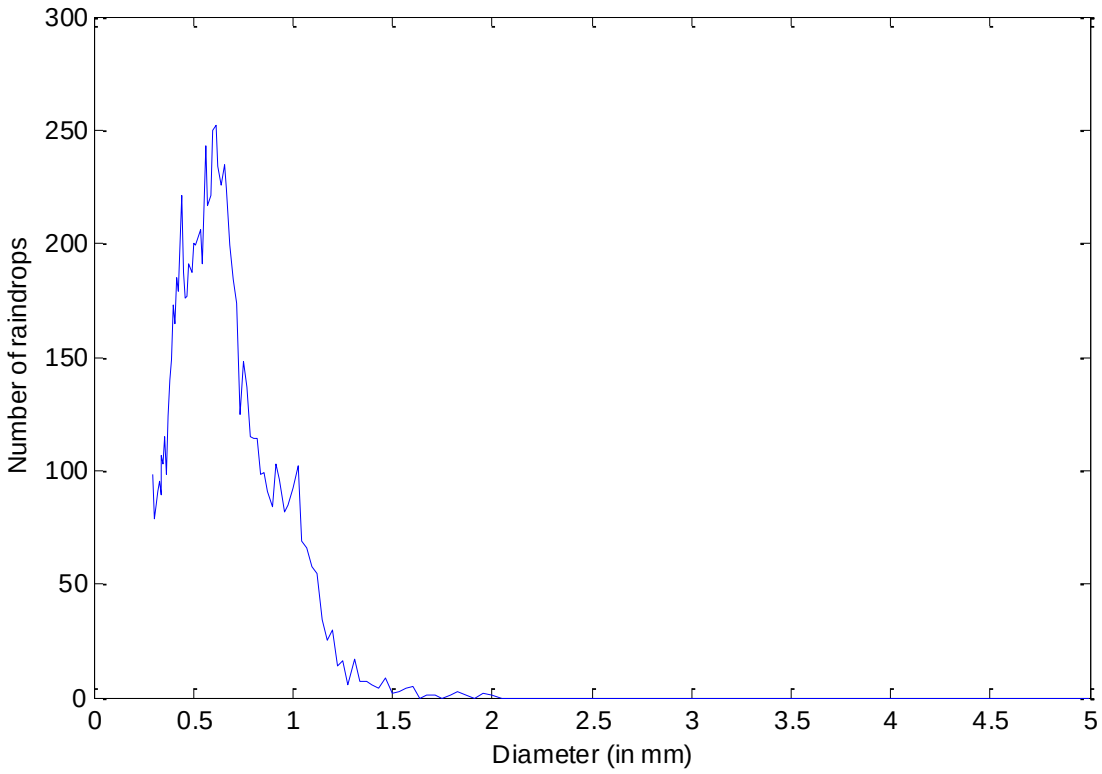

Figure 59: An example of the total number of drops vs the drop diameters measured by the Joss Waldvogel disdrometer at the BADC in Chilbolton, UK

7.2.3 The fall velocity of the drops

Here, we assume the rain droplets fall at their respective terminal velocity. As mentioned as part of the literature review, the relation between the terminal velocity of water droplets and their respective sizes (in drop diameter) has been researched extensively where these models have been discussed. The comparison of the different models are shown Figure 60. Using these models, the velocity can be predicted accurately from raindrop size. The preferred model for this simulation is the relationship is $V_t = \exp(2.397 - 1.006/d)$ provided by Valette et al. (2012).

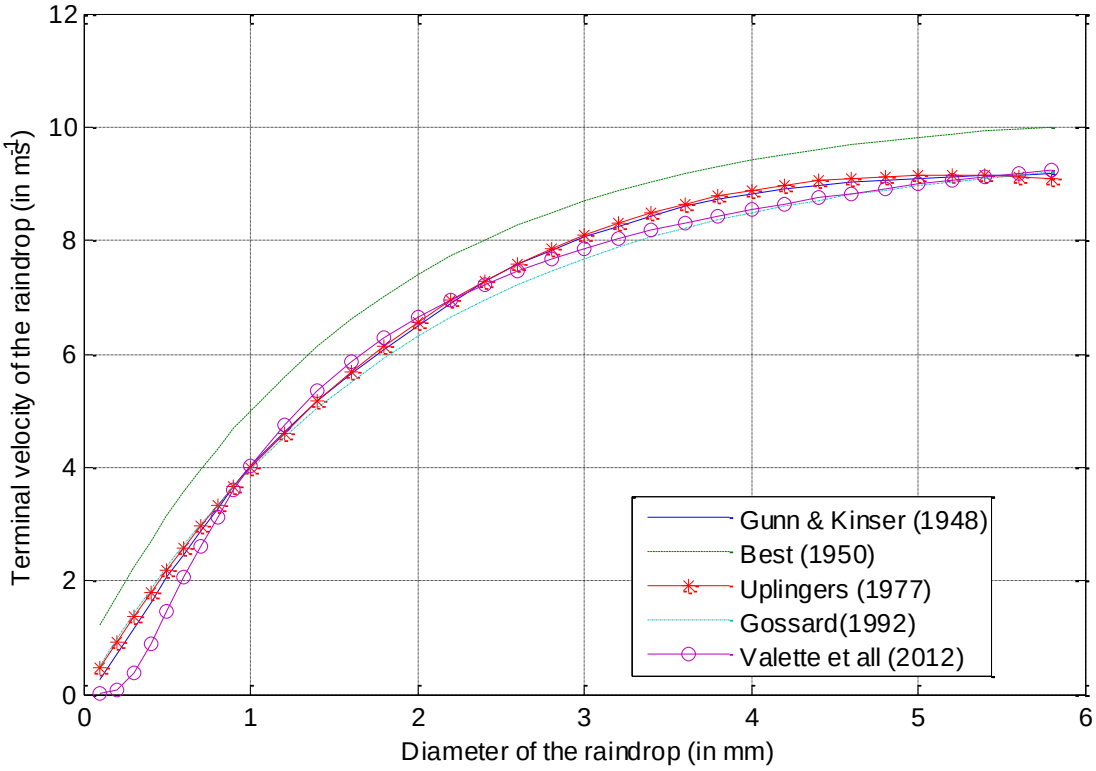

Figure 60: Comparison of the different models for terminal velocity of a raindrop vs equivalent diamter adapted from (Valette et al. (2012))

7.3 Device response for rain simulation

In this sub-section we will look at the program for the simulation for the device response, it consists of two main parts. The first part is the simulation of rain (as discussed earlier) and the second part of the program is the output response of the device arrangement to the simulated rain. The steps involved for this purpose can be summarised as shown in Figure 61. The force time spectrum is calculated using overlap and add method, the results of which is convolved with the impulse response function of the device. An example result of the force- time spectrum for a particular drop size distribution is as shown in the Figure 62. This force- time spectrum calculated by the convolution of the impulse response of the transducer- plate arrangement results in its output response of the respective plate. The number of drops are then calculated by correlating the drop size to the peak impact measured by the transducer. This method is discussed as part of the impact detection and drop size prediction section.

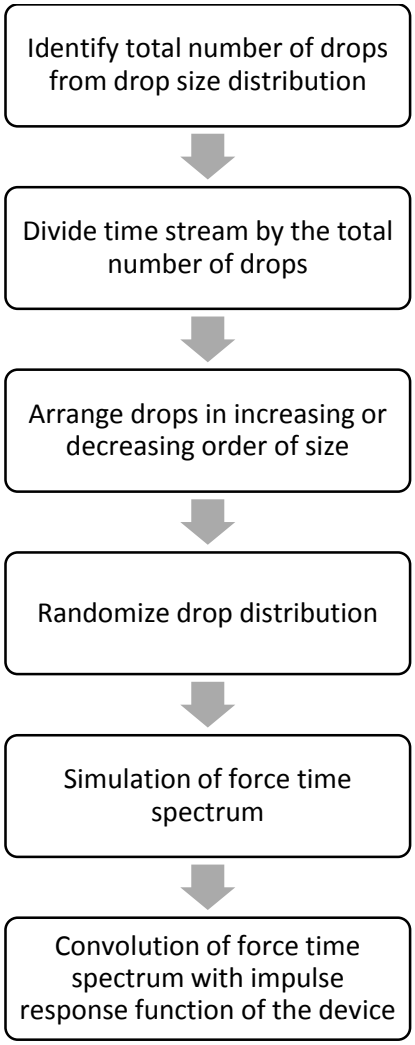

Figure 61: Summary of the steps involved to simulate the output response of the device for a particular drop size distribution

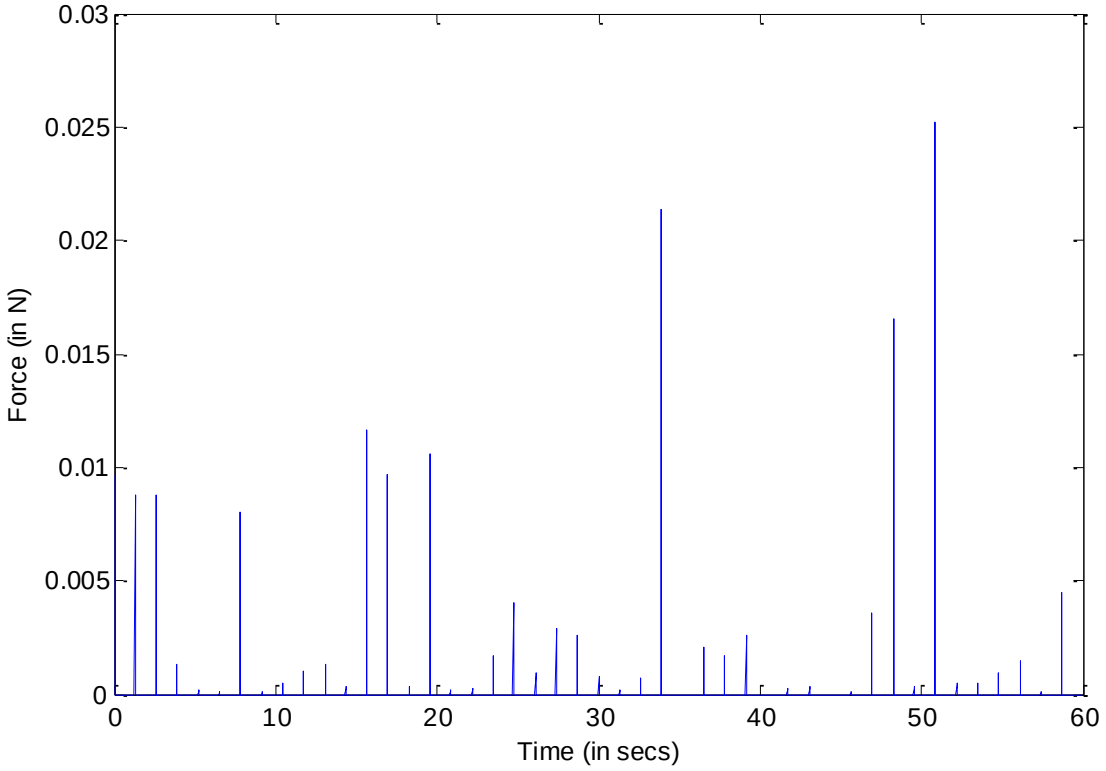

Figure 62: Simulated force time series for raindrop impacts taken from BADC drop size distribution data for $60secs$

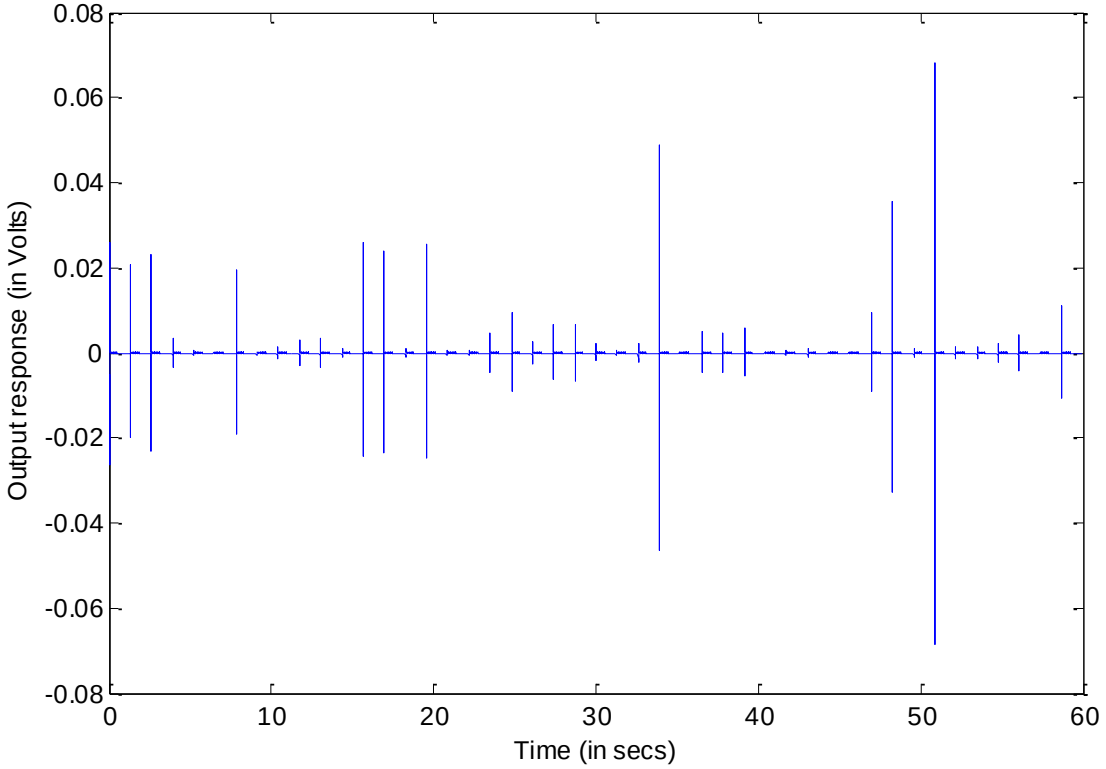

Figure 63: Simulated output response series for raindrop impact taken from BADC drop size distribution data for $60secs$ *as seen by a transducer plate arrangement of* $2mm$ *thickness and* $50mm$ *diameter clamp*

7.4 Single drop calibration

As mentioned as part of the introduction, there are two methods for the calibration of the device. For this thesis, we will look into calibration using a single drop. This is mainly due to the ease of conducting the experiment and the presence of rain simulator designed as part of chapter 4. The rain simulator is used to drop single droplet of a known size on the transducer plate arrangement. However, due to the limited height of the rain simulator, the drops generated may not be able to reach their terminal velocity. We have a formula to estimate the final fall velocity of the drop depending upon the fall height Euler's method, this was discussed as part of chapter 4 (equation 4.1).

The output of the transducer is measured using the Bruel & Kjaer pulse front end connected to a computer. The measured output response is used to identify the droplet size using the assumptions made about drop size, drop velocity, and drop force. As part of this experiment, the drop sizes identified for the calibration of the plate include $2.23mm$, $3.29mm$ and $3.89mm$ diameter. A location is selected on the plate ($P0$ in this case at the centre of the device) and the water droplets are dropped on it. The output response of the plate (time domain and frequency domain) are measured, the process for identifying the drop size from the output response is highlighted in Figure 64 and the result of the comparison for a drop sized $3.89mm$ is shown in Figure 65. As can be seen, there is a good correlation between the measured output response of the plate to the droplet, and the calculated output response (using the frequency response of the plate in Volts/Newton and the simulated force).

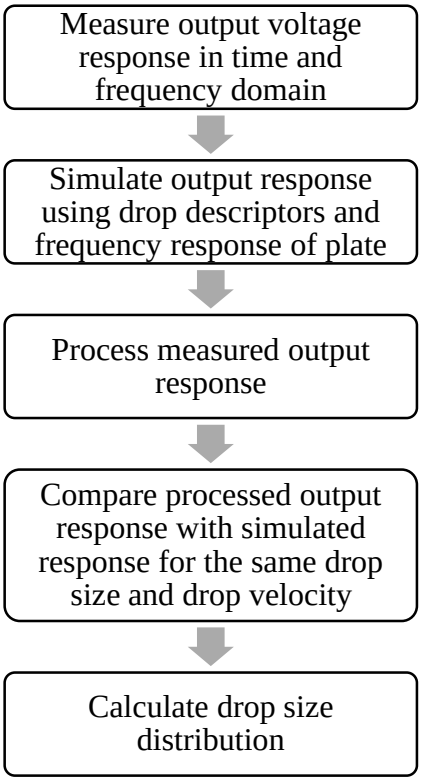

Figure 64: Summary of the steps involved for single drop calibration

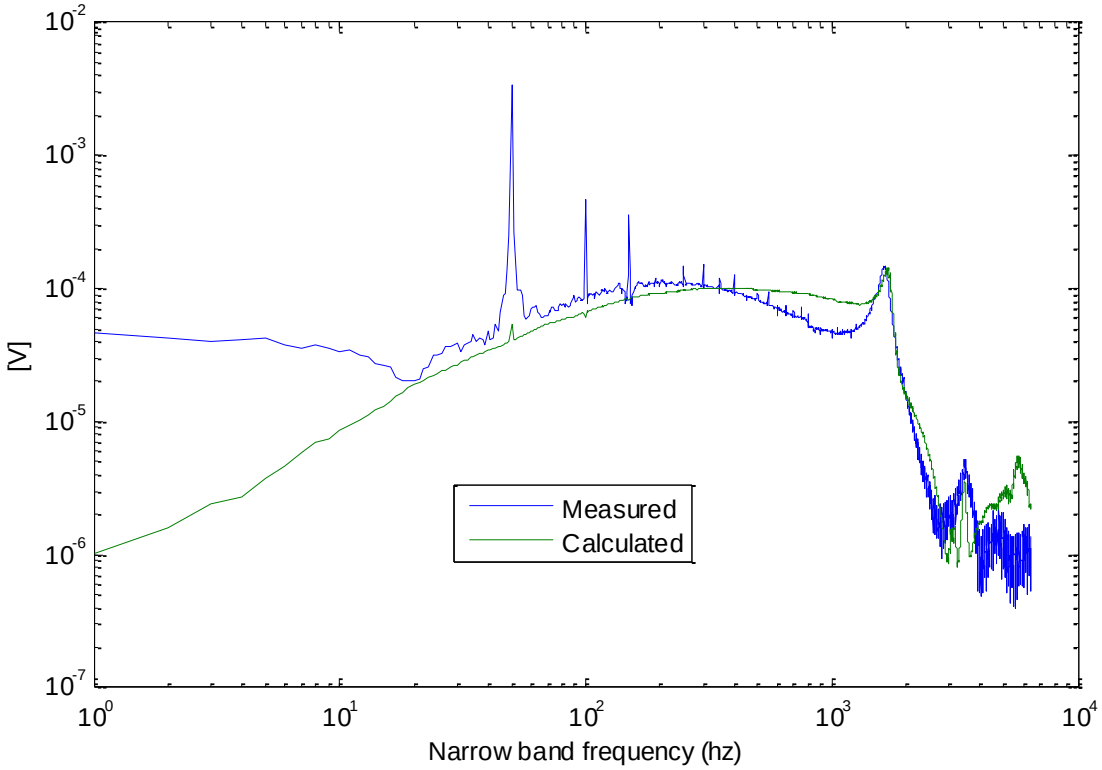

Figure 65: Comparison of the measured output response to calculated output response for a drop of size 3.89*mm diameter on a device configuration of 2mm thickness and 50mm clamp ring*

7.5 Signal processing

In this section we'll look at developing a signal processing algorithm for analysing the measured signals. Signal processing plays a major role in development of electronics, the chosen technique is required to be able remove the impact of environmental noise and vibration, to be able to identify and count the drop from the measured or simulated impacts as part of the process discussed as part of the previous section. The main processes can be summarised to three main tasks – noise reduction, impact detection and drop size prediction, and finally rain intensity prediction.

7.5.1 Noise reduction

In this sub-section, we'll look at how the signal processing can be used for reducing the impact of noise in the measurements. Unfortunately, the measure signals can be affected by various factors during the process of acquisition in sensor devices. The noise affects the analysis of the measurement, making it a no brainer to remove the noise. The main aim of this process is for noise to be removed whilst not distorting the measurement made. The different signal processing techniques that can potentially be used for noise reduction is highlighted as part of the literature review.

As part of the measurements made in chapter 3 and chapter 6, we found the transducer very susceptible to electrical noise and the frequency range of interest for the signal is within $100hz$ – $2000hz$, however rain is a stochastic process and we can approach this for the captured time series of the rain by shortening the window length. Due to the vast amount of data that will be acquired, some of this processing would be unnecessary at times when there is no rain. It is for this reason, the selected method for processing of the data is wavelet transforms. The results of the processing using wavelet transform on a raw signal (Figure 66) is shown in Figure 67.

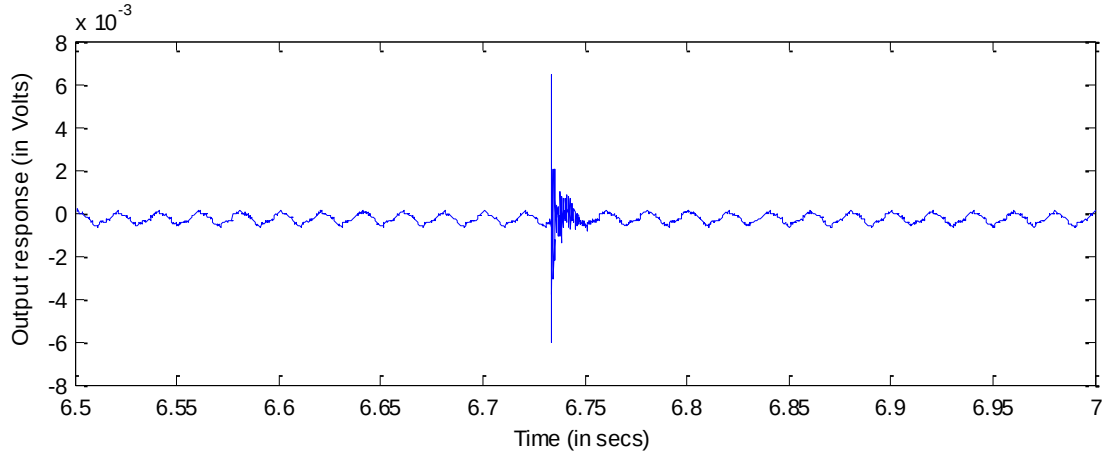

Figure 66: Raw output response measured for a drop of size 3.29mm diameter on a device configuration plate thickness 2mm and 50mm diameter

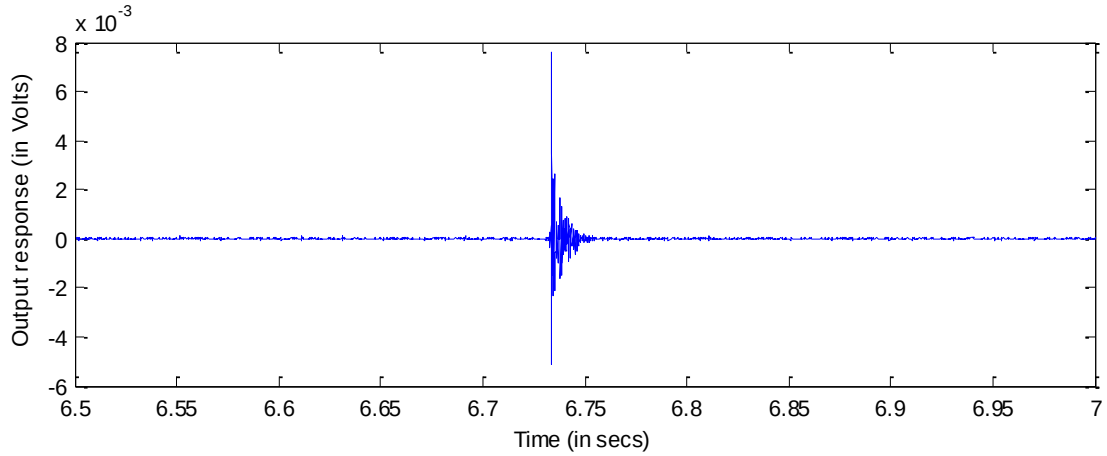

Figure 67: Processed output response of a drop of size 3.29mm diameter using discrete wavelet transform on a device configuration plate thickness 2mm and 50mm diameter

7.5.2 Impact detection and drop size prediction

In this sub-section we'll look at impact detection and drop size prediction. The main purpose of the application is to detect the impact of the drop and predict the size of the drop. Following on from the noise reduction, the processed time series of the measured signal, abrupt changes can be detected by the use of edge detection techniques wherein any abrupt changes in voltage is taken as a drop event. Once the drop event is identified, the drop size is required to be calculated. The drop size can be correlated to the measured peak voltage. It is fairly conclusive that as the size of the drop increases, the impact force of the drop increases, hence increasing the measured peak voltage.

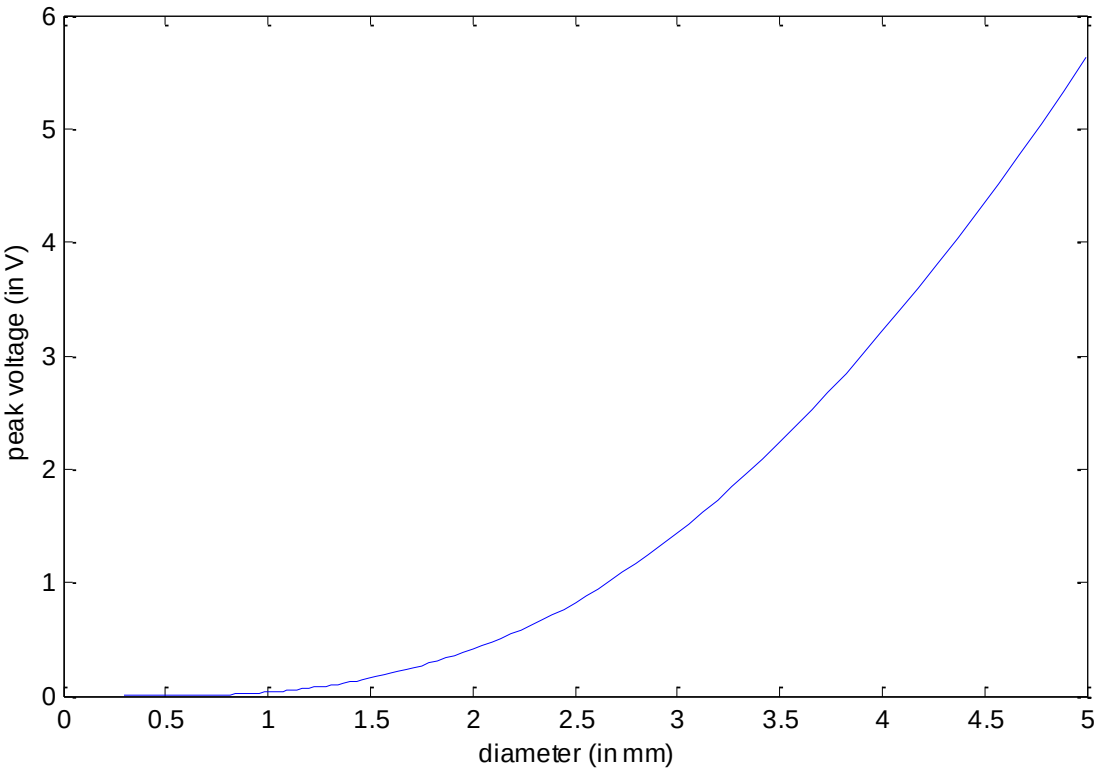

Figure 68: Comparison of the peak voltage calculated for a 2mm thickness with 50mm diameter clamp transducer plate arrangement for each drop sizes against the diameter of the drop

The size of the drops are classified into different bins of different sizes identified by the mean size of the respective bin. Once the size of the drops are identified, they are counted in their respective bins to return the drop size distribution for that particular rain event. However, there is one issue that arises. This is primarily because the frequency response of the plate decreases as a function of distance (away) from the sensor, with the sensor located at the centre of the circular plate. In chapter 3, we identified different location points to measure the frequency

response of the plate in $Volts/Newton$. The different location points for a 2mm thickness plate and a 50mm diameter ring configuration are shown in Figure 69. The variation of the peak voltage measured against the drop sizes across the different points is shown in Figure 70. In order to counter this, the secondary check corroborates the size of the drop by comparing to the pulse width. Alternative methods on countering this issue will be discussed as part of the final conclusion chapter.

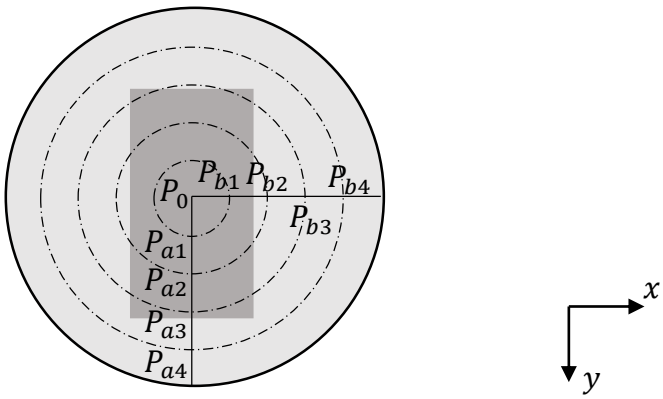

Figure 69: Depiction of the sensor plate arrangement for a plate with a clamp ring size $50mm$ *with selected points of contact. The transducer is represented by the greyed out area*

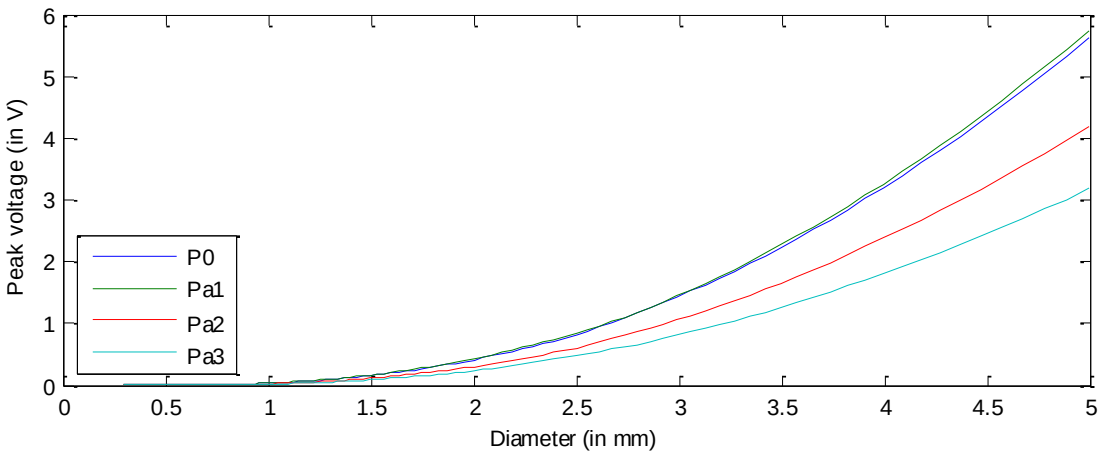

Figure 70: Variation of the peak voltage calculated for a 2mm thickness with 50mm diameter clamp configuration for each drop sizes against the diameter of the drop across the various location on the transducer plate arrangement

7.5.3 Rain rate prediction

The signal processing algorithm is required to be able to remove the impact of environmental noise and vibration and to be able to identify and count the drop from the measured impacts or simulated as part of the process discussed as part of the previous sub section. The method for calculating the rain intensity from the drop size distribution is discussed as part of the literature review. Using this relation, the equation to calculate rain rate is highlighted below.

$$R = \sum_K R_K = \sum_K \frac{\pi}{6} \frac{D_K^3 N_K}{t_{int} A_s} \qquad [mm\ h^{-1}] \tag{7.1}$$

7.6 Summary

In this chapter we looked at utilising simple calibration techniques for the identification of the droplets. In this method the device is calibrated using single drops of known diameter and drop velocity. We also developed a signal processing algorithm that includes noise reduction, impact detection and finally drop size detection. The chosen algorithm can be summarised to four key steps- denoising, impact detection, drop size prediction and finally rain rate prediction. The signal processing algorithm utilises wavelet transforms for denoising. Following which, the impacts of the drops are detected using edge detection and the peak voltage is compared to the drop size look up table where the drops are classified to different bins that returns the drop size distribution. Using the drop size distribution, the rain rate can be calculated from equation 7.1.

In the following chapter, we look to provide a conclusion to the thesis, proposed design for the device, and details on future work.

8 Conclusion

8.1 Summary

The purpose of the thesis is to describe the journey towards investigating the development of the sensor stack to be a part of an integrated sensor approach to device architecture for low cost integrated rain sensing and measuring application. The device architecture consists of three main stacks – energy generation layer, sensing layer, processing layer. The sensing and measuring of rain is done by measuring the vibration caused by rain on the device and correlating this to the volume of the raindrop. There are two main parameters used to describe rain, these are rain rate and raindrop size distribution. Rain rate is defined as the measure of the intensity of rainfall and is expressed in millimetres per hour (in units of speed rather than volume) and it is the most commonly used parameter and drop size distribution is defined as the probability distribution of the number of drops per unit size (expressed in diameter or volume of the drop) per unit volume of space as measured on the surface of the earth. It was found that the size of rain drops vary from minute size up to $6mm$ diameter.

The measurement of the amount of rain and classification of its type helps gain a better understanding of our environment and prepare for disasters such as drought or flooding. However, due to the localized nature and variability of precipitation makes it difficult to understand and model its physical parameters and behaviour. In order to better understand the various hydrological operations (river flow, floods, irrigation planning, modelling of catchment area); a high spatial density is advantageous. This can be enabled by the use of wireless sensor technologies to build an inexpensive sensor network, for this reason the device designed needs to be inexpensive and have a low power consumption. The interconnected devices constantly collect and process a large density of data to help provide an understanding of our physical world by analysing different events/ occurrences. The selected method for measuring rain drop size distribution and rain intensity is to indirectly calculate the impact force of individual droplets by measuring the strain caused on the front facing surface of the device.

As part of the research process, we looked to understand the process of rain formation which helped us understand various issues to developing a physical and dynamic description of rain-size, mass, velocity and force of a drop. Following which, a general background to vibration analysis was studied and how these can be implemented for inverse force synthesis using the frequency model method. Also provided was an overview to designing the sensor device.

The approach taken to evaluate the design of the sensing surface was to characterise different combinations of plate and clamp ring arrangement by measuring and comparing respective frequency response functions. Using this results we were able to simulate the output response and calibrate the selected device configuration for different sizes of water droplets. Also calculated was the output response of the transducer- plate configuration for different levels of noise. The simulation helped us identify the minimum measurable drop size for the configuration of the plate size, and selected sensor

The research helped us to define the design parameters for the sensing layer of the proposed device. The device surface is designed to be small in size so as to not be affected by the varying noise levels and to be large enough to be a representative sample of falling raindrops as mentioned in chapter 3. It is required the impedance of the selected surface is more than that of the lowest drop measurable and also less susceptible to environmental noise. It is for this reason a $2mm$ thickness plate with $50mm$ clamp ring, with the selected transducer a thin film piezo sensor of dimensions $30mm \times 16mm \times 52\mu m$ (attached to the centre of the plate) as the device configuration. The minimum drop size measurable depends on how the device of the above mentioned configuration is affected by environmental noise, this value is $0.4mm$ diameter as mentioned in chapter 6. By applying these minimum design parameters to the sensing surface, the remaining layers of the device can then be selected. As part of the embedded design, the device will consist of primarily three layers – sensing & energy generation layer, electronic layer, and energy storage layer in a stack configuration as shown in Figure 1. By comparing the force of a drop (theoretical vs measured), we find the frequency range of interest is between $100hz$ and $1700hz$. The working frequency range of the device is between $100hz$ and $2000hz$, this includes the first modal peak that acts as an amplification to the drop impact.

However, there are a few issues have been encountered with this approach. Calibration of the device is key as we are measuring the impact force of the rain drops and correlating it to the size of the drop. Primary, Not all rain drops will fall on the device at terminal velocity (the main assumption for calibration of the device), as the fall velocity of the droplet may also be affected by the wind. Secondly, the spatial variation of the of the frequency response function in $Volts/Newton$ in decreasing order from the centre of the plate. This may lead to underestimating the size of the drop based on its position of impact with the device. Heavy rain

may easily mask the impact of small drops and finally, environmental noise can interfere with its operation and affect the design of the device.

As of now, the chosen approach has been validated for a minimum drop size of $2.23mm$. The working of the device for drop sizes less than $2.23mm$ is tested through simulation, however requires further experimentation to validate results (particularly for drops less than $1mm$ diameter). Other solutions to mitigate the issues encountered will be discussed as part of further work.

8.2 Further work

The previous section provides a summary of the work completed as part of the research. In this section we look to enlist areas of further work as a result of this research. Three areas of work has been identified

- Selection of energy generation layer as per proposed design
- To improve the measurement algorithm
- To explore introduction of secondary transducer
- Alternative idea for making force measurement

8.2.1 Selection of energy generation layer

As per the design as shown in Figure 1, the main requirement for the selection of the type of energy generation layer is it should not impede the ability of the device to measure rain. The device could potentially get its energy from the vibrations due to rain. An alternative to this would be to integrate the sensing surface with solar cells.

8.2.2 To improve measurement algorithm

More work is required in this area as existing disdrometers can measure a lower drop size of $0.2998mm$. The current lowest drop size measurable by the device configuration is $0.4mm$. Also desirable is the ability to differentiate between other types of weather conditions such as snow, and hailstorm.

8.2.3 To explore the introduction of the secondary transducer

One of the method identified to mitigate the issue relating to the impact position of the drop is to attach a secondary thin film sensor perpendicular to the existing thin film sensor measuring the deflection of the plate on the perpendicular axis as shown in Figure 71.

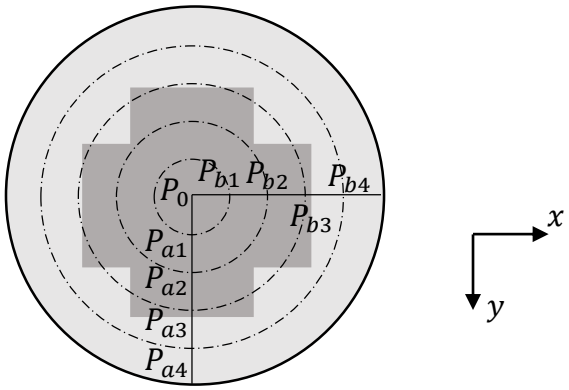

Figure 71: Depiction of the sensor plate arrangement for a plate with a clamp ring size $50mm$ *with secondary thin film sensor attached perpendicular to the axis of the primary sensor. The sensors are represented by the greyed out area*

8.2.4 Multiple force transducer idea

An alternative idea to improve the measurement is the use of a circular array of force transducers. The transducers used will make a direct measurement of the impact forces of the individual droplets and calculate the drop size distribution and rain intensity. A schematic representation of the proposed idea is shown in Figure 72.

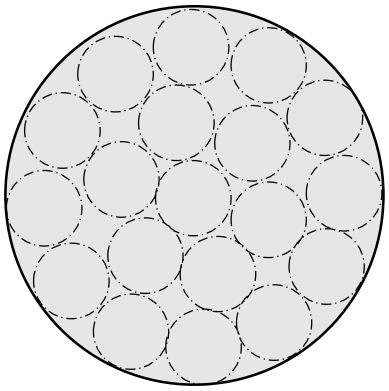

Figure 72: Schematic representation of multiple force transducer

9 References

Amos, J. (2014). Smart umbrellas 'could collect rain data'. *Science.* Retrieved 01/05/2014, 2014, from http://www.bbc.co.uk/news/science-environment-27222282

Anastasi, G., Conti, M., Di Francesco, M., & Passarella, A. (2009). Energy conservation in wireless sensor networks: A survey. *Ad Hoc Networks, 7*(3), 537-568. doi: 10.1016/j.adhoc.2008.06.003

Bagree, R. (2012). *Characterization and Design of a Readout Circuit for a Piezoelectric-based Acoustic Disdrometer*. TU Delft, Delft University of Technology.

Barnaghi, P., Wang, W., Henson, C., & Taylor, K. (2012). Semantics for the Internet of Things. *International Journal on Semantic Web and Information Systems, 8*(1), 1-21. doi: 10.4018/jswis.2012010101

Beard, K. V., Bringi, V., & Thurai, M. (2010). A new understanding of raindrop shape. *Atmospheric Research, 97*(4), 396-415.

Becker, G., & Güdesen, A. (2000). Passive sensing with acoustics on the battlefield. *Applied Acoustics, 59*(2), 149-178. doi: http://dx.doi.org/10.1016/S0003-682X(99)00023-7

Bentley, W. A. (1904). Studies of raindrops and raindrop phenomena. *Monthly Weather Review, 32*(10), 450-456.

Best, A. C. (1950). Empirical formulae for the terminal velocity of water drops falling through the atmosphere. *Quarterly Journal of the Royal Meteorological Society, 76*(329), 302-311.

Blau, M. (1999). Indirect measurement of multiple excitation force spectra by FRF matrix inversion: Influence of errors in statistical estimates of FRFs and response spectra. *Acustica, 85*(4), 464-479.

Boggess, A., & Narcowich, F. J. (2009). *A first course in wavelets with Fourier analysis*: John Wiley & Sons.

Briggs, J. C. (1991). *Force identification using extracted modal parameters, with applications to glide height testing of computer hard disks.* Massachusetts Institute of Technology.

Campos, E. F. (1999). On measurements of drop size distribution. *Top. Meteor. Oceanog, 6*(1), 24-30.

Crossley, J., Kundgol, A., Mellors, N., & Waterworth, S. (2011). VENT CONTROLLING APPARATUS: WO Patent WO/2011/104,290.

Dobson, B., & Rider, E. (1990). A review of the indirect calculation of excitation forces from measured structural response data. *Proceedings of the Institution of Mechanical Engineers, Part C: Journal of Mechanical Engineering Science, 204*(2), 69-75.

Eigel, J., & Moore, I. (1983). A simplified technique for measuring raindrop size and distribution. *Transactions of the ASAE [American Society of Agricultural Engineers]*.

Ergen, B. (2012). Signal and image denoising using wavelet transform. *Advances in Wavelet Theory and Their Applications in Engineering, Physics and Technology*, 495-514.

Ewins, D. J. (1986). *Modal Testing: Theory and Practice*: Letchworth: Research Studies.

Fernandez-Raga, M., Palencia, C., Tomas, C., Calvo, A. I., Castro, A., & Fraile, R. (2011). Rain research with disdrometers: a bibliometric review. *Atmospheric Measurement Techniques Discussions, 4*(5), 6041-6068.

Förster, J., Gust, G., & Stolte, S. (2004). A piezoelectrical rain gauge for application on buoys. *Journal of Atmospheric & Oceanic Technology, 21*(2).

Gardner, J. W., & Udrea, F. (1994). *Microsensors: principles and applications* (Vol. 994): Wiley Chichester.

Gilbert, J. M., & Balouchi, F. (2008). Comparison of energy harvesting systems for wireless sensor networks. *International Journal of Automation and Computing, 5*(4), 334-347. doi: 10.1007/s11633-008-0334-2

Glossary of Statistical terms. (2002, December 20, 2005). from http://stats.oecd.org/glossary/detail.asp?ID=5058

Gossard, E., Strauch, R., Welsh, D., & Matrosov, S. (1992). Cloud layers, particle identification, and rain-rate profiles from ZRVf measurements by clear-air Doppler radars. *Journal of Atmospheric and Oceanic Technology, 9*(2), 108-119.

Guigon, R., Chaillout, J. J., Jager, T., & Despesse, G. (2008a). Harvesting raindrop energy: experimental study. *Smart Materials & Structures, 17*(1), 015039.

Guigon, R., Chaillout, J. J., Jager, T., & Despesse, G. (2008b). Harvesting raindrop energy: theory. *Smart Materials & Structures, 17*(1), 015038.

Gunn, R., & Kinzer, G. D. (1949). The Terminal Velocity of Fall for Water Droplets in Stagnant Air. *Journal of Meteorology, 6*(4), 243-248.

Hanna, E. (1995). How effective are tipping-bucket raingauges? A review. *Weather, 50*(10), 336-342.

He, J., & Fu, Z.-F. (2001). *Modal Analysis*. Oxford: Butterworth-Heinemann.

Höller, C. (2013). *Indirect methods of obtaining activity and mobility of structure-borne sound sources.* University of Liverpool.

Jameson, A., & Kostinski, A. (2001). What is a raindrop size distribution? *Bulletin of the American Meteorological Society, 82*(6), 1169-1177.

Jayawardena, A. W., & Rezaur, R. B. (2000). Measuring drop size distribution and kinetic energy of rainfall using a force transducer. *Hydrological Processes, 14*(1), 37-49. doi: 10.1002/(sici)1099-1085(200001)14:1<37::aid-hyp908>3.0.co;2-m

Jones, D. M. (1959). The shape of raindrops. *Journal of Meteorology, 16*(5), 504-510.

Junger, M. C., & Feit, D. (1972). *Sound, structures, and their interaction* (Vol. 240): MIT press Cambridge, MA.

Kompis, C., & Aliwell, S. (2008). Energy harvesting technologies to enable remote and wireless sensing. *Sensors and Instrumentation-Knowledge Transfer Network*.

Kostinski, A. B., & Shaw, R. A. (2009). Droplet dynamics: Raindrops large and small. *Nature Physics, 5*(9), 624-625.

Kourtellis, A. G., Kasparis, T., Jones, L., & Lane, J. (2005). *Disdrometer calibration using an adaptive signal processing algorithm.* Paper presented at the OCEANS, 2005. Proceedings of MTS/IEEE.

Laws, J. O., & Parsons, D. A. (1943). The relation of raindrop-size to intensity. *Transactions, American Geophysical Union, 24*, 452-460.

Mason, B. (1978). Physics of a Raindrop. *Physics Education, 13*(7), 414-419.

Mathuna, C. O., O'Donnell, T., Martinez-Catala, R. V., Rohan, J., & O'Flynn, B. (2008). Energy scavenging for long-term deployable wireless sensor networks. *Talanta, 75*(3), 613-623. doi: 10.1016/j.talanta.2007.12.021

Mitcheson, P. D., Yeatman, E. M., Rao, G. K., Holmes, A. S., & Green, T. C. (2008). Energy harvesting from human and machine motion for wireless electronic devices. *Proceedings of the Ieee, 96*(9), 1457-1486.

Morris, A. S. (2001). *Measurement and instrumentation principles*: Butterworth-Heinemann.

Perlin, K. (2002). *Improving noise.* Paper presented at the ACM Transactions on Graphics (TOG).

Petersson, B. (1995). The Liquid drop impact as a source of sound and vibration. *Building Acoustics, 2*, 585-624.

Randall, R. B. (1987). *Frequency analysis*: Brül & Kjor.

Ries, J., Seeger, M., Iserloh, T., Wistorf, S., & Fister, W. (2009). Calibration of simulated rainfall characteristics for the study of soil erosion on agricultural land. *Soil and Tillage Research, 106*(1), 109-116.

Salmi, A., Ikonen, J., & Oyj, V. (2005). *Piezoelectric precipitation sensor from Vaisala.* Paper presented at the WMO Technical Conference on Instruments and Methods of Observation (TECO-2005), Bucharest, Romania.

Sensor, M. S. (2008). Technical Manual.

Sheppard, B. E., & Joe, P. I. (1994). Comparison of Raindrop Size Distribution Measurements by a Joss Waldvogel Disdrometer, a PMS 2DG Spectrometer, and a Poss Doppler Radar. *Journal of Atmospheric and Oceanic Technology, 11*(4), 874-887.

Shieh, J., Huber, J., Fleck, N., & Ashby, M. (2001). The selection of sensors. *Progress in materials science, 46*(3), 461-504.

Solomon, K. H., Kincaid, D., & Bezdek, J. (1985). Drop size distributions for irrigation spray nozzles. *Transactions of the ASAE-American Society of Agricultural Engineers (USA)*.

Strangeways, I. (2010). A history of rain gauges. *Weather, 65*(5), 133-138.

Taylor, J. (1997). *Introduction to error analysis, the study of uncertainties in physical measurements* (Vol. 1).

ten Wolde, T., & Gadefelt, G. R. (1987). Development of Standard Measurement Methods for Structure Borne Sound Emission. *Noise control engineering, 28*(1), 5-14.

Tokay, A., Kruger, A., & Krajewski, W. F. (2001). Comparison of drop size distribution measurements by impact and optical disdrometers. *Journal of Applied Meteorology, 40*(11), 2083-2097.

Uplinger, W. (1981). *A new formula for raindrop terminal velocity*. Paper presented at the Conference on Radar Meteorology, 20 th, Boston, MA.

Valette, G., Prévost, S., Léonard, J., & Lucas, L. (2012). A virtual discrete rainfall simulator. *Environmental Modelling & Software, 29*(1), 51-60. doi: 10.1016/j.envsoft.2011.10.003

Van Boxel, J. H. (1998). *Numerical model for the fall speed of rain drops in a rain fall simulator*. Paper presented at the Proceedings of the International Workshop on Technical Aspects and Use of Wind Tunnels for Wind-Erosion Control: Combined Effects of Wind and Water Erosion on Processes, November 17–18 1997, Ghent, Belgium.

Van Dijk, A. I. J. M., Bruijnzeel, L. A., & Rosewell, C. J. (2002). Rainfall intensity-kinetic energy relationships: a critical literature appraisal. *Journal of Hydrology, 261*(1-4), 1-23.

Villermaux, E., & Bossa, B. (2009). Single-drop fragmentation determines size distribution of raindrops. *Nat Phys*, *5*(9), 697-702. doi: http://www.nature.com/nphys/journal/v5/n9/suppinfo/nphys1340_S1.html

Weddell, A. S., Harris, N. R., & White, N. M. (2008). *Alternative energy sources for sensor nodes: rationalized design for long-term deployment.* Paper presented at the Instrumentation and Measurement Technology Conference Proceedings, 2008. IMTC 2008. IEEE.

Wilson, J. W., & Brandes, E. A. (1979). Radar measurement of rainfall-A summary. *Bulletin of the American Meteorological Society*, *60*(9), 1048-1058.

Yu, P., Qinghua, L., & Xiyuan, P. (2010). *The design of low-power wireless sensor node.* Paper presented at the Instrumentation and Measurement Technology Conference (I2MTC), 2010 IEEE.